CONTROLS ON METHANE EXPULSION DURING MELTING OF NATURAL GAS HYDRATE SYSTEMS: TOPIC AREA 2

PHASE 1 REPORT

MARCH 31, 2014

CONTENTS

SUMMARY OF RESEARCH

TASK 1: PROJECT MANAGEMENT AND PLANNING

Projected Finish: 9/30/15
Actual Finish: In process

1) An initial web-based kick off meeting was held on 11/07/2012.
2) Twice-monthly telephone conferences with all of our participants have been organized and held.
3) We recruited one post-doctoral scientist for the project (Dr. Kehua You) who arrived from Texas A&M on June 15, 2013.
4) We recruited 4 graduate students for the project.
5) Dylan Meyer (geoscience, started F 2012), Kris Darnell (geoscience, Fall 2012), Jason Sanford (geoscience, Spring 2014), Imran Khan (petroleum engineering, Spring 2014).
6) We organized travel and supported experiment at LBNL
    a. Peter Polito, LBNL visit, Jan 2 – 4, 2013
    b. Peter Polito, LBNL visit, July 7 - 12, 2013
    c. Kehua You, LBNL visit, Sept 22 – 27, 2013
    d. Steve Bryant, 2013 NCGC Symposium, Oct 29 – 30, 2013
    e. Peter Polito & Dylan Meyer, LBNL visit, Dec 16 – 20, 2013
7) Completed Reports (as of the end of budget period one):
    a. 5 Quarterly Research Performance Progress Reports
    b. 17 Cost Accrual Reports
    c. 5 SF-425 Federal Financial Reports
8) We purchased equipment for construction of a thermistor string. The thermistor string consists of ten 10 kΩ resistors epoxied ten centimeters apart inside a 0.25” OD stainless steel tube. External circuitry converts the temperature-controlled resistance drop in each loop to a DC voltage, which is recorded and converted to temperature by a LabVIEW program.

TASK 2: CONCEPTUAL AND NUMERICAL MODEL DEVELOPMENT -1D

Projected Finish: 3/31/14
Actual Finish: 3/31/14

SUMMARY:

Task 2 is on schedule for completion on 3/31/14. Significant accomplishments include that we completed development of two models: 1) An analytical ‘box’ model to describe hydrate formation in a specific volume; and 2) a one dimensional, fully coupled, transient numerical transport model that describes hydrate formation and multi –phase (gas and water) flow. The ‘box’ model is used to design our experimental approach and to then understand the experimental results. The numerical model is used to simulate hydrate formation and dissociation both at the experimental and geological scales. A major computing challenge that was overcome was to stabilize and make more efficient the numerical model that we completed. We applied the 'numerical' and 'box' model to simulate the behavior we pursued in our laboratory experiments. The match between theory and observation was remarkable. We applied the coupled model to predict the effect of seafloor warming on marine hydrate deposits (2.3.2). A significant finding was that given a sufficient initial hydrate deposit, the methane that was disassociated would self-propagate through the hydrate stability zone and vent to the ocean. The remaining subtask (2.3.1) that will be completed before 3/31/14 is to simulate the effect of warming on a deposit in a sub permafrost deposit.

Analytical 'box' model

Here we derive an analytical solution to calculate the maximum hydrate saturation and methane gas consumption during hydrate formation in sediments partially saturated with water and flooded with methane gas. We present examples where the pore fluid is assumed to both saline and fresh. This model is based on thermodynamic equilibrium among liquid phase, vapor phase and hydrate phase. Three components, water, salt and methane, are considered in the model. The calculations are based on mass conservations of water, salt and methane in the 'box'.

Case 1: Saline solution

Figure 1 shows the schematic diagram for this model. Initially, the sediment is filled with $S_{g,i}$ methane gas (dimensionless, gas saturation) and $S_{w,i}$ water (dimensionless, water saturation) with a salinity of $X^{s}_{w,i}$ (wt.%). The initial pressure and temperature in the system is P_i (Pa) and T_i (^{o}C), respectively. Methane hydrate starts to form when the system pressure and temperature decrease to the hydrate stable zone P_f (Pa) and T_f (^{o}C), respectively. During hydrate formation, methane gas is allowed to freely flow into the sediment while no water reservoir is connected to the sediment.

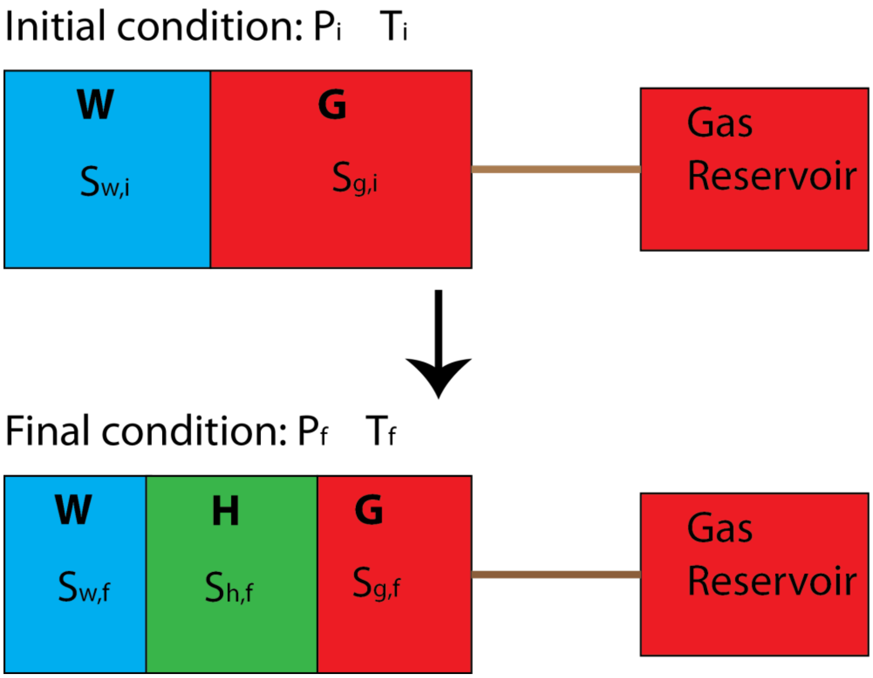

Figure 1: Schematic diagram of the 'box' model. G is gas or vapor phase. W is water or liquid phase. H is hydrate phase. P_i and T_i are the initial pressure and temperature, respectively. P_f and T_f are the final equilibrium pressure and temperature, respectively. $S_{g,i}$ and $S_{w,i}$ are the initial gas and water saturations, respectively. $S_{g,f}$, $S_{w,f}$ and $S_{h,f}$ are the final equilibrium gas, water and hydrate saturations, respectively.

Since salt is transported by water flow and there is no water flow that enters or leaves the system during the experiment, the total amount of salt initially in the sediment should equal that after hydrate formation. Therefore, one has

$$V_{tot}\phi S_{w,i}\rho_{w,i}X^{s}_{w,i} = V_{tot}\phi S_{w,f}\rho_{w,f}X^{s}_{w,e}\,, \qquad \text{Eq. 1}$$

where V_{tot} is the total volume of the sediment (m^3); ϕ is porosity (dimensionless); $X^{s}_{w,e}$ is the mass fraction of salt in brine at three phase equilibrium condition (wt.%) , which can be calculated from the phase boundary curves of brine, gas and methane hydrate using P_f and T_f (Liu and Flemings, 2007); $\rho_{w,i}$ and $\rho_{w,f}$ are the initial and final brine density in the sediment, which can be calculated using the initial and final pressure, temperature and salinity values, respectively (Liu and Flemings, 2007). We reorganize Eq. (1) and obtain the final water saturation as

$$S_{w,f} = \frac{S_{w,i}\rho_{w,i}X^{s}_{w,i}}{\rho_{w,f}X^{s}_{w,e}}\,. \qquad \text{Eq. 2}$$

The maximum hydrate saturation is calculated from the mass conservation of fresh water in the sample. The initial mass of the fresh water in the brine should equal the final mass of the fresh water in the brine plus that in the hydrate, therefore, one has

$$V_{\text{tot}}\phi S_{w,i}\rho_{w,i}\left(1-X^{s}_{w,i}\right)\left(1-X^{m}_{w,i}\right)=V_{\text{tot}}\phi S_{w,f}\rho_{w,f}\left(1-X^{s}_{w,f}\right)\left(1-X^{m}_{w,e}\right)+\frac{V_{tot}\phi S_{h,f}}{M_{h}/\rho_{h}}NM_{w}\,, \qquad \text{Eq. 3}$$

where $X^{m}_{w,i}$ and $X^{m}_{w,f}$ are the initial and final solubility of methane in the water (wt.%) As in Liu and Flemings (2007), the solubility of methane in water in presence of hydrate is calculated using the model of *Henry et al.* (1999) , while the solubility of methane in water in absence of hydrate is calculated using the model of *Duan et al.* (1992). M_w and M_h are the molar weight of water (kg mol^{-1}) and methane hydrate (kg mol^{-1}), respectively; ρ_h is the methane hydrate density, and we used the value of 912 kg m^{-3} in this study; N is the stoichiometric hydration number, which is assumed to be constant and equal to 5.75 in this study. We restate Eq. (3) and obtain the maximum hydrate saturation of

$$S_{h,f}=\frac{\left[S_{w,i}\rho_{w,i}\left(1-X^{s}_{w,i}\right)\left(1-X^{m}_{w,i}\right)-S_{w,f}\rho_{w,f}\left(1-X^{s}_{w,f}\right)\left(1-X^{m}_{w,e}\right)\right]M_{h}}{NM_{w}\rho_{h}}\,. \qquad \text{Eq. 4}$$

The final gas saturation can be written as

$$S_{g,f}=1-S_{w,f}-S_{h,f}\,. \qquad \text{Eq. 5}$$

Mass conservation of methane is used to calculate the methane gas consumption in the sample. Initially, the methane is distributed in water and gas phase. At three phase equilibrium condition, the methane is distributed in water, gas and hydrate phases, therefore, one has

$$\Delta m=m^{m}_{w,f}+m^{m}_{g,f}+m^{m}_{h,f}-m^{m}_{w,i}-m^{m}_{g,i}\,, \qquad \text{Eq. 6}$$

where Δm is the mass of methane gas consumed during hydrate formation (kg); $m^{m}_{w,f}$, $m^{m}_{g,f}$, $m^{m}_{h,f}$ are the mass of methane (kg) in the final water, gas and hydrate phases, respectively; $m^{m}_{w,i}$ and $m^{m}_{g,i}$ are the mass of methane (kg) in the initial water and gas phases, respectively. They are calculated as

$$m_{w,f}^{m} = V_{tot}\phi S_{w,f}\rho_{w,f}X_{w,f}^{m}, \qquad \text{Eq. 7}$$

$$m_{g,f}^{m} = V_{tot}\phi S_{g,f}\rho_{g,f}, \qquad \text{Eq. 8}$$

$$m_{h,f}^{m} = \frac{V_{tot}\phi S_{h,f}\rho_{h}}{M_{h}}M_{m}, \qquad \text{Eq. 9}$$

$$m_{w,i}^{m} = V_{tot}\phi S_{w,i}\rho_{w,i}X_{w,i}^{m}, \qquad \text{Eq. 10}$$

$$m_{g,i}^{m} = V_{tot}\phi S_{g,i}\rho_{g,i}, \qquad \text{Eq. 11}$$

where M_m is the molar weight of methane (kg mol^{-1}); $\rho_{g,i}$ and $\rho_{g,f}$ are the initial and final gas density (kg m^{-3}), respectively, which can be calculated from the initial and final temperature and pressure, respectively (Liu and Flemings, 2007). Substitute Eqs. (7)-(11) into Eq. (6), one can obtain the methane gas consumption during methane hydrate formation at the final pressure and temperature of P_f and T_f, respectively.

Case 2: Fresh water

In this case, methane hydrate is formed in a sediment column initially partially saturated with fresh water and flooded with the methane gas. Under the same three phase equilibrium pressure and temperature condition for saline water P_f and T_f as discussed above, the fresh water system reaches liquid and hydrate stable zone. However, since the sediment is connected with a methane gas reservoir, and water is limited, theoretically all the water initially in the sediment should be converted to hydrate. Therefore, one has

$$S_{w,f} = 0. \qquad \text{Eq. 12}$$

By conservation of water mass, we find

$$V_{tot}\phi S_{w,i}\rho_{w,i}\left(1 - X_{w,i}^{m}\right) = \frac{V_{tot}\phi S_{h,f}}{M_{h}/\rho_{h}}NM_{w}. \qquad \text{Eq. 13}$$

We reorganize Eq. (13) and obtain the maximum hydrate saturation for the case of fresh water

$$S_{h,f} = \frac{S_{w,i}\rho_{w,i}\left(1 - X_{w,i}^{m}\right)M_{h}}{NM_{w}\rho_{h}}. \qquad \text{Eq. 14}$$

The final gas saturation is calculated by Eq. (5). According to the mass conservation of methane, one can calculate the methane gas consumption for the fresh water case as follows

$$\Delta m = m_{g,f}^{m} + m_{h,f}^{m} - m_{w,i}^{m} - m_{g,i}^{m}. \qquad \text{Eq. 15}$$

$m_{g,f}^{m}$, $m_{h,f}^{m}$, $m_{w,i}^{m}$ and $m_{g,i}^{m}$ can be calculated by Eqs. (8)-(11), respectively.

Matlab programs SH_BRINE and SH_FRESH have been developed to assist the above calculations for the saline water and fresh water cases, respectively.

Numerical model

This numerical model considers the fully coupled multiphase, multicomponent fluid flow, solute transport and heat flow. It was originally developed by *Liu* (2006) and has been described in *Liu and Flemings* (2007) . The downward direction is set as positive direction. This model is based on local thermodynamic equilibrium among the liquid, vapor, and hydrate phases. Three components, water, salt and methane, are considered in the model. Fluid flow in the system includes viscous flow (pressure driven), capillary flow (saturation-gradient driven) and gravity flow (buoyancy driven). Heat is transported by conduction and advection.

The following assumptions are used in the model: (1) Darcy's law describes multiphase fluid flow in the uniform porous media. (2) There is no sedimentation and erosion. (3) There is no in situ biogenic methane. (4) Methane is the only hydrate-forming gas. (5) Salt is confined to the liquid phase. (6) Methane is assumed to be the only component in the gas phase. (7) Hydrate is a solid phase and only two-phase (vapor+liquid) capillary pressure is considered. (8) The temperature among each phase is locally in equilibrium.

Appling mass conservation to each component, one can get the mass balance equation for methane as

$$\phi \frac{\partial \left(\sum_{\beta=l,v,h} \rho_\beta S_\beta X_\beta^m \right)}{\partial t} - \sum_{\beta=l,v} \nabla \left\{ \frac{k k_{r\beta}}{\mu_\beta} \left(\nabla P_\beta - \rho_\beta g \right) \rho_\beta X_\beta^m \right\} - \nabla \left\{ \phi^2 D_{l0}^m \rho_l \nabla X_l^m \right\} - q^m = 0. \qquad \text{Eq. 16}$$

The mass balance equation for water is

$$\phi \frac{\partial \left(\sum_{\beta=l,h} \rho_\beta S_\beta X_\beta^w \right)}{\partial t} - \sum_{\beta=l} \nabla \left\{ \frac{k k_{r\beta}}{\mu_\beta} \left(\nabla P_\beta - \rho_\beta g \right) \rho_\beta X_\beta^w \right\} - \nabla \left\{ \phi^2 D_{l0}^w \rho_l \nabla X_l^w \right\} - q^w = 0. \qquad \text{Eq. 17}$$

The mass balance equation for salt is

$$\phi \frac{\partial\left(\sum_{\beta=l}\rho_\beta S_\beta X_\beta^{s}\right)}{\partial t} - \sum_{\beta=l}\nabla\left\{\frac{kk_{r\beta}}{\mu_\beta}\left(\nabla P_\beta - \rho_\beta g\right)\rho_\beta X_\beta^{s}\right\} - \nabla\left\{\phi^2 D_{l0}^{s}\rho_l \nabla X_l^{s}\right\} - q^{s} = 0. \qquad \text{Eq. 18}$$

In the above three equations, the superscripts m, w and s denote methane, water and salt, respectively. The subscripts *l*, *v* and *h* denote liquid, vapor and hydrate phases, respectively.

ϕ is porosity (dimensionless). *t* is time (sec). *k* is sediment permeability (m^2). ρ_β, S_β, μ_β, P_β and $k_{r\beta}$ are the density (kg m^{-3}), saturation (dimensionless), dynamic viscosity (Pa sec), pressure (Pa) and relative permeability of β phase, respectively. X_β^{m}, X_β^{w} and X_β^{s} are the mass fractions of methane, water and salt in β phase, respectively. *g* is acceleration due to gravity (m s^{-2}). D_{l0}^{m}, D_{l0}^{w} and D_{l0}^{s} are the molecular diffusion coefficient (m^2 s^{-1}) of methane, water and salt, respectively. q^m, q^w and q^s are the sources or sinks of methane, water and salt, respectively.

The energy balance equation (superscript *e*) is

$$\frac{\partial\left((1-\phi)\rho_R C_R T + \sum_{\beta=l,v,h}\phi\rho_\beta S_\beta u_\beta\right)}{\partial t} - \sum_{\beta=l,v}\nabla\left\{\frac{kk_{r\beta}}{\mu_\beta}\left(\nabla P_\beta - \rho_\beta g\right)\rho_\beta h_\beta\right\} - \nabla\{\lambda\nabla T\} - q^{e} = 0, \qquad \text{Eq. 19}$$

where the subscript *R* denotes the solid grain. *T* is temperature (^{o}C). λ is the bulk thermal conductivity of the porous media (W m^{-1} ^{o}C^{-1}), and $\lambda = (1-\phi)\lambda_R + \phi \sum_{\beta=l,v,h} S_\beta \lambda_\beta$. λ_β, u_β and h_β are the thermal conductivity (W m^{-1} ^{o}C^{-1}), specific internal energy (J kg^{-1}) and specific enthalpy (J kg^{-1}) of phase β, respectively.

Duan et al.'s (1992) model is used to calculate the methane solubility in water in absence of methane hydrate. Henry et al.'s (1999) model is used to calculate the methane solubility is water in presence of methane hydrate. The Leverett J-function is used to describe the relationship between capillary pressure and pore fluid saturation (Bear, 1972). Corey's model is used to calculate the relative water and gas permeability (Bear, 1972).

Porosity is defined as the pore volume fraction filled with fluid phases (liquid and vapor). As hydrate forms, porosity is reduced as $\phi = \phi_0(1 - S_h)$, where ϕ_0 is the porosity (dimensionless) in absence of hydrate. The decrease of porosity leads to the decrease of intrinsic permeability, which is described by the model of *Kleinberg et al.* (2003), where hydrate is assumed to form in the center of the pores. The decrease in porosity and permeability can change the capillary pressure, which is calculated as $P_c = \sqrt{{k_0\phi}/{\phi_0 k}}\,P_{c0}$, where k_0 and P_{c0} are the intrinsic permeability (m^2) and capillary pressure (Pa) in absence of hydrate, respectively.

The numerical model is solved by fully implicit block-centered finite-difference method. Upstream weighting is used to calculate the phase mobility, and harmonic weighting is used to calculate the intrinsic permeability. Newton_Raphson method is used to iteratively solve the nonlinear equations. Primary variables switching method is used in case of the appearance or disappearance of phases.

The Matlab program originally developed by *Liu* (2006) for this numerical model can only simulate the case when the sediment is initially 100% saturated with water. We modified the input files and the files calculating the Jacobian and residual matrixes for solving the nonlinear equations to extend the program to more general cases of any arbitrary initial water, gas or hydrate saturations. Besides, we added a dynamic time-step choice to improve the numerical stability. With the dynamic time-step choice, the simulation starts with a big time-step value. This value will be cut down to a smaller one whenever the calculation cannot be converged or when it is converged to unreasonable situations, for example, when the saturations are less than zero or greater than 100%. At the new time, the time-step will get back to the original big value to guarantee the efficiency of the simulation. We also added the choice of manually controlling the sediment temperature and fixed gas pressure boundary condition to simulate the laboratory experiment.

SUBTASK 2.1 - DISSOCIATION OF 1D VERTICAL HYDRATE ACCUMULATION

Milestone 1.A 1-D simulation of gas hydrate dissociation in natural systems.

SUBTASK 2.2 - APPLY 1D MODEL TO LABORATORY EXPERIMENT

Milestone 1.B 1-D Simulation of gas hydrate dissociation in laboratory controlled conditions.

This section is to simulate the laboratory experiment described in section 4.1 using the analytical 'box' model and the fully coupled numerical model described above. Initially, the 12.7 cm long F110 sand sample is saturated with 49 vol.% methane gas and 51 vol.% brine having a salinity of 3.5 wt.%. The F110 sand sample has a porosity of 35%, an intrinsic permeability of 8.3×10^{-13} m^2 and capillary entry pressure of about 0.02 MPa. The initial temperature for the sample is 17 $^{\circ}$C, and the initial gas pressure is 6.94 MPa. We fix the gas pressure at the upstream end of the sample to be 6.94 MPa by connecting it to a constant pressure pump, which allows methane gas to freely enter or leave the sample upon the pressure change in the sample. We set a closed boundary at the downstream end of the sample. For the convenience of space discretization in the numerical model, we set the sample length to be 12 cm. But the displayed results here have been corrected by this volume change from the real sample (12.7 cm in length).

Figure 2 shows the accumulated methane gas consumption during the hydrate formation and dissociation predicted by the analytical (blue line) and numerical models (yellow line). The numerically predicted gas consumption is slightly less than the analytically predicted value (yellow line is slightly below blue line). This is because the analytical model neglects the capillary pressure and treats the water pressure as equaling the gas pressure. The predicted Gas consumptions increase from nearly zero to greater than 1 g when temperature is decreased to 8 ^{o}C. Methane hydrate is predicted to form when the temperature is decreased to 8.4 ^{o}C at the pressure of 6.94 MPa and salinity of 3.5 wt.%. After that the predicted gas consumptions increase stepwise as temperature is decreased for hydrate formation, and then decrease stepwise as temperature is increased for hydrate dissociation. The black line with rectangle markers is the laboratory measured methane gas consumption, which will be discussed in detail in Task 4.

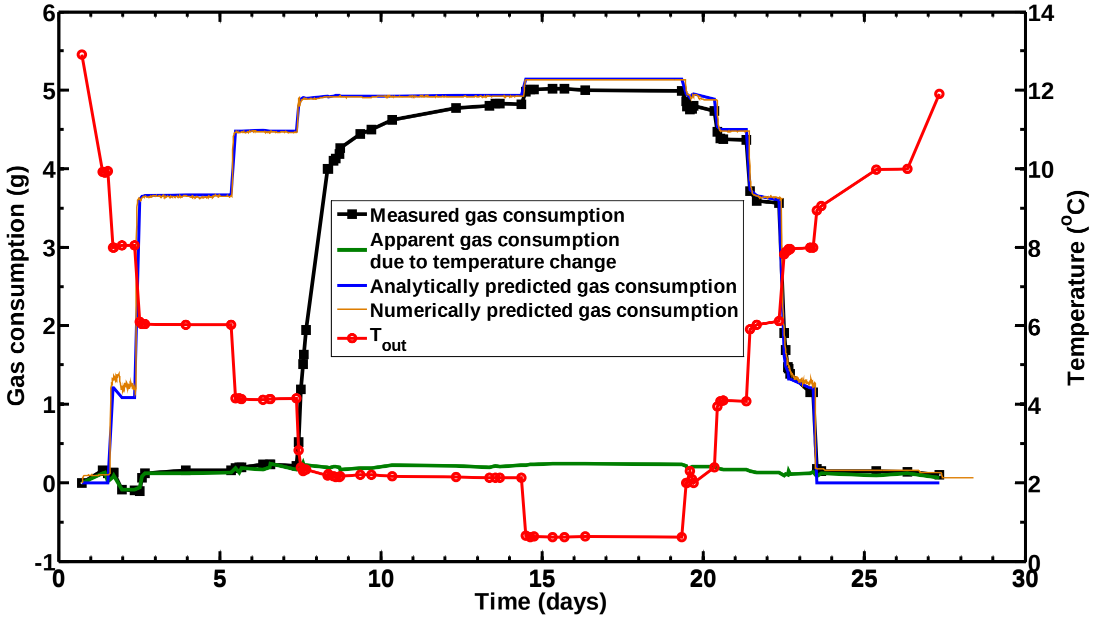

Figure 2: Comparison of measured and predicted methane gas consumption during hydrate formation and dissociation. T2 is the temperature measured on the out radius of the sample. The sample is initially filled with sediment of porosity 35%, and water saturation of 51%. Gas is allowed to flow into or out of the sample. Pressure is held constant by connecting the upstream end of the sample to a constant pressure pump.

Figure 3 shows the distribution of the water, gas and hydrate saturation in the sample calculated by the numerical model at Day 1, 11, 17, 22 and 23 when the sample temperature is 17 (room temperature), 2.2 and 0.6 ^{o}C during hydrate formation, and 4.1 and 6 ^{o}C during hydrate dissociation, respectively. The sample is initially homogeneously saturated with 49 vol.% methane gas and 51 vol.% water. Therefore, the simulated saturations are quite homogeneous across the sample. Hydrate saturation increases as temperature decreases.

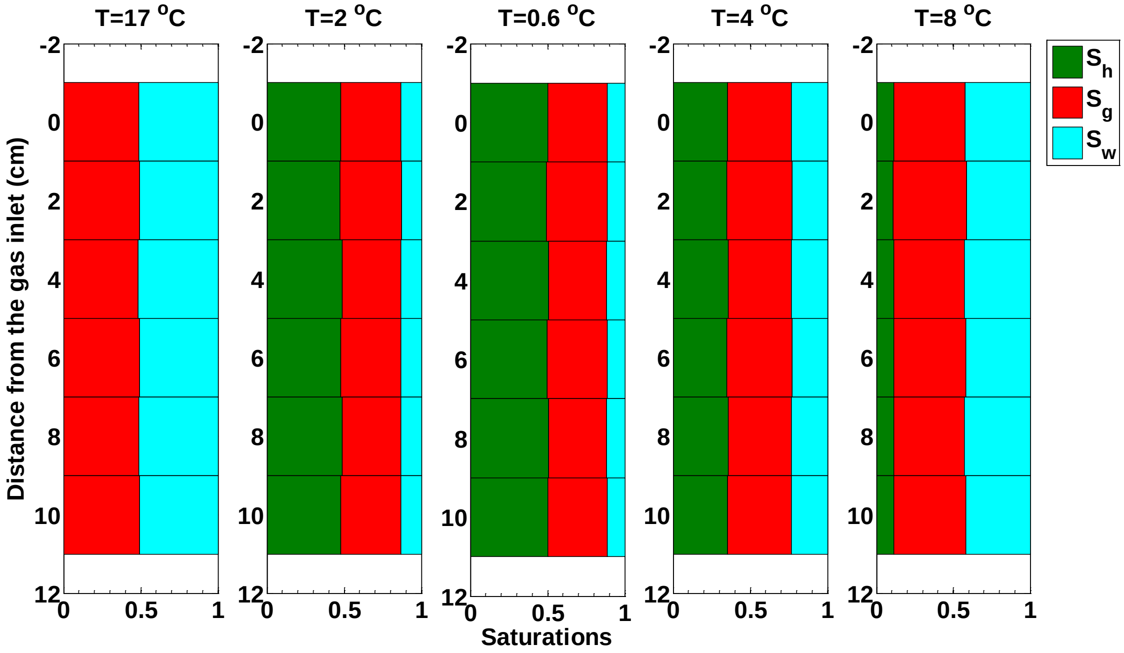

Figure 3: Distribution of saturations at Day 1, 11, 17, 22 and 23 when the sample temperature is 17 (room temperature), 2, 0.6, 4 and 8 °C, respectively.

Figure 4 shows the predicted water, gas and hydrate saturations and salinity using the analytical (lines) model. The predicted results by the numerical model are not shown here because they are undistinguishable from the predicted results by the numerical model. As temperature is decreased to below 8.4 °C, hydrate saturation increases while water and gas saturation decreases stepwise as temperature is decreased for hydrate formation. At the same time, salinity increases and stabilizes to a fixed value at each temperature. As temperature is increased from Day 19 for hydrate melting, hydrate saturation decreases while water and gas saturation increases stepwise. Salinity decreases stepwise as hydrate dissociates. Each point on the curves is three-phase equilibrium when hydrate saturation is greater than zero.

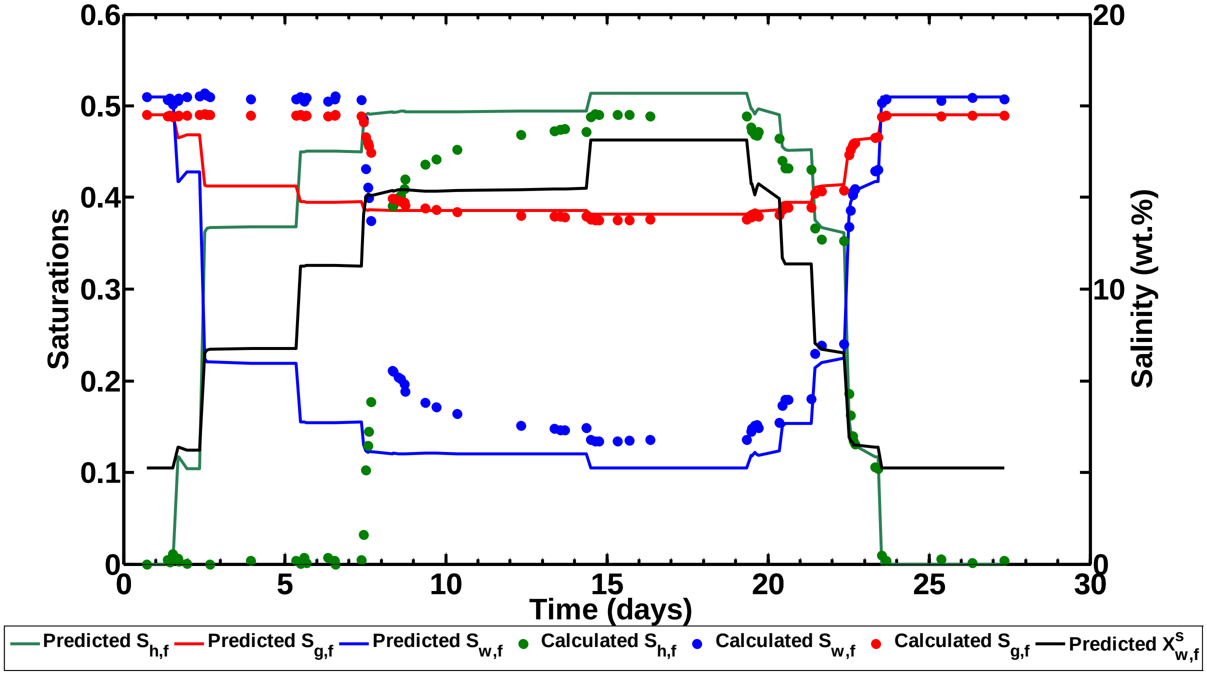

Figure 4: Comparison between the calculated water (blue), gas (red) and hydrate bulk saturations (green) using the measured methane gas consumption (dots) and the predicted saturations using the analytical solutions (lines).

SUBTASK 2.3 - 1D MODELS OF NATURAL EXAMPLES

Subtask 2.3.1 Hydrate accumulations below permafrost

Subtask 2.3.2 - 1D model application to deposits near up-dip limit of stability zone on continental margins

Milestone 1.C Model-based determination of conditions required for gas not to reach seafloor/atmosphere from dissociating hydrate accumulation.

2.3.2.1 Introduction

We use the dynamic, multiphase flow model of (Liu and Flemings, 2007) to investigate the sensitivity of natural hydrate systems to warming perturbations. Our simulations aim to test the hypothesis that hydrate systems close to three-phase equilibrium1) are most sensitive to warming, 2) are the sources of high methane release, and 3) may exhibit transient behaviors as the warming signal propagates into the sediment column. We test these hypotheses by considering one specific case study modeled after (Reagan and Moridis, 2008), who in their 'Case III' simulate a cold, shallow hydrate deposit typical of the arctic continental shelf. We model a one-dimensional, vertical geometry that initially only contains seawater and hydrate, and captures, both, the regional hydrate stability zone (RHSZ) and the sediment below the RHSZ. We force the system with small, instantaneous temperature perturbations (+ 0.22C) and analyze the evolution over long time scales (~10kyr).

Using this general framework, we show that hydrate is melted at the base of the RHSZ (BRHSZ) and that the dissociated gas migrates upward creating its own three-phase equilibrium pathway. The upward migrating gas reforms hydrate once it enters into the new hydrate stability zone. However, the gas can self-propagate through the overlying hydrate stability zone and breach the seafloor if the initial hydrate saturation is sufficiently large for a given level of warming.

The generic result from the hydrate dissociation simulation is as follows. Warming at the seafloor diffusively propagates downward eventually elevating the temperature at the hydrate deposit to the local stability temperature. This causes dissociation at the base of the deposit. The temperature throughout the deposit remains fixed at the stability temperature during dissociation, but adjusts according to dissociation-induced changes in pressure and salinity at depth. Once enough hydrate dissociates, the gas buildup can freely flow upward and a zone with gas and hydrate exists. This vertical gas transport and basal hydrate dissociation continues until the gas reaches the new location for the BRHSZ. At the new BRHSZ, the gas re-solidifies as hydrate raising the temperature of the surrounding deposit through the release of latent heat. This latent heat release warms the overlying sediment above the stability temperature and raises the salinity during hydrate formation-driven salt expulsion. This allows concurrent hydrate formation and vertical gas flow. In this way, the free gas propagates upward in three-phase equilibrium despite being in the RHSZ. This self-propagation moves all the way to the seafloor. Eventually, hydrate formation shuts down due to methane depletion at the seafloor, and this shutdown propagates downward. The final deposit is shifted upward according to the new P-T conditions and contains less methane than the initial deposit due to venting at the seafloor.

These simulation results contrast previous work, which has suggested that free gas does not migrate through the hydrate stability zone, but instead migrates laterally along the dissociating BRHSZ. The transient venting events described above are a new phenomenon that has not previously been discussed or analyzed within models. The remainder of this section will address the conditions under which this behavior is applicable and the implications for natural systems worldwide.

2.3.2.2 Model Setup

We simulate a deposit below the seafloor with an overlying water column of 320 m, a seafloor temperature of 0.4 C, and a geothermal gradient of 0.03 C / m. Our simulation domain contains a grid above the seafloor where sh=0 and the pressure is hydrostatically fixed. This is an open boundary in which we monitor outward fluxes of gas and water. The bottom boundary is at 120 mbsf. We initiate the model with a hydrate deposit 60 m in depth with the top of the deposit at 40 m below the seafloor. The BRHSZ is 100 mbsf before the temperature perturbation. The deposit has a hydrate saturation of 10% by volume. We assess the implications that the new behavior has on natural systems, with special attention to the inherent dependence on hydrate saturation.

At time = 0 years, we introduce a warming at the seafloor that is instantaneous and held fixed throughout time. We analyze two cases, where Case 1 has a 0.1 C perturbation, and Case 2 has a 0.22 C perturbation. All else remains constant between the two cases. Furthermore, neither of these temperature perturbations is sufficient to eliminate the RHSZ. The expectation is that all gas remains within the system and should eventually all be contained in hydrate, albeit with a BRHSZ that has shoaled substantially.

In Case 1, we expect the BRHSZ to shoal 20 m. And in Case 2, we expect the BRHSZ shoal of 35 m.. Finally, in Case 3 the HSZ is completely eliminated with all available methane vented into the ocean. These three cases demonstrate different behaviors and illuminate a new scenario for venting.

2.3.2.3 Simulation Results

Case 1:

In Case 1, the hydrate at the base melts once the temperature perturbation has reached the BRHSZ. The bottom-most layer entirely dissociates, then the gas moves freely upward and reforms hydrate directly above, at the depth of the new RHSZ. During the dissociation of the hydrate, the warming signal ceases its propagation and the temperature at the dissociation depth is held fixed at the three-phase equilibrium temperature. The hydrate formation increases the salinity due to the expulsion of salt in the hydrate structure. However, these effects are insufficient to alter the state of the system further. Instead, all of the methane that is mobile is converted to hydrate at its lowest possible depth. Once all of the mobile methane is re-converted to hydrate, the salt diffuses away from the source of the formation and the heat slowly diffuses away as well. The final hydrate deposit sits at the expected location and total methane losses are minimal and restricted to pressure induced water flux into the ocean within the dissolved phase.

Case 2:

In Case 2, the hydrate at the base also melts once the temperature perturbation has propagated through the deposit. However, the upward migrating gas does not immediately reform hydrate. Instead, the overlying hydrate also undergoes dissociation and the free gas creates a pressure buildup. The pressure buildup forces gas migration. The gas at the new RHSZ does begin to reform some hydrate, but this additional heat and salinity is too much forcing for the overlying hydrate. These combined effects create a high salinity, high temperature pathway that 'burns' through the overly hydrate. Thus, a free gas pathway exists with venting into the ocean. This persists until the gas column loses its buoyancy driven mobility. Then, the top-most gas reforms hydrate capping additional free gas flow. The formation signal then propagates downward, depleting all of the available, mobile methane within the RHSZ. At the end of the simulation, there is a hydrate deposit situated where one would it expect it to be based on a static, thermodynamic analysis. However, the dynamic adjustment drives ~25% of the original methane quantity (by volume) into the ocean. We show results below for Case 2.

Case 3:

In Case 3, the system behaves very similarly to Case 2 until hydrate begins dissociating. Once dissociation begins, the entire deposit quickly undergoes dissociation with upward gas propagation. A vent develops within 1 kyr. Eventually all methane is vented into the ocean at a rate much greater than that observed in Case 2.

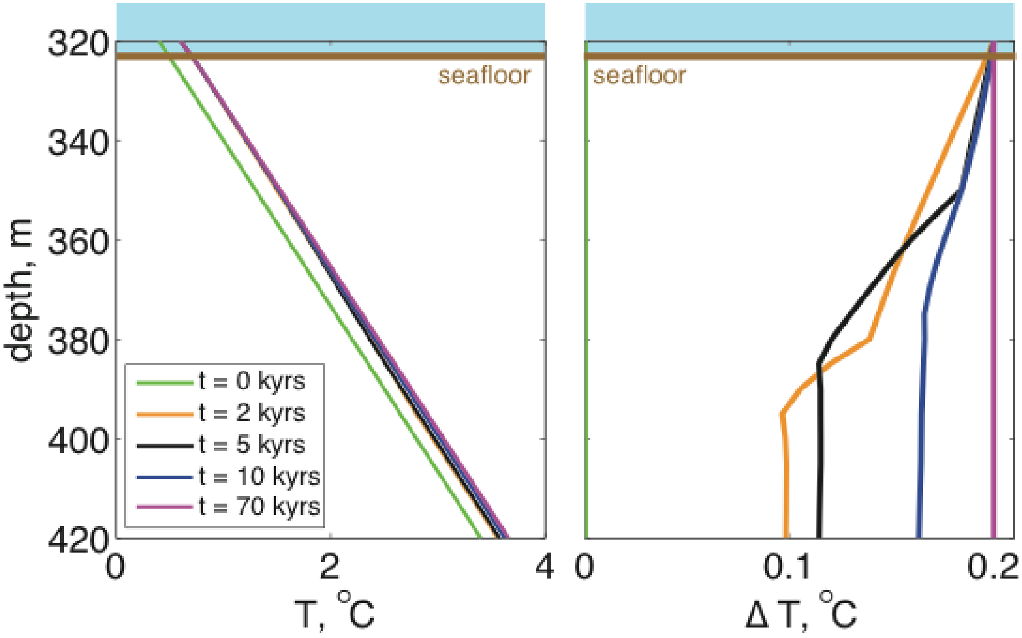

Figure 5: (Left) The temperature evolution from Case 2. The initial temperature profile does not include the temperature perturbation. This is applied directly after and held constant. (Right) The temperature difference from the initial.

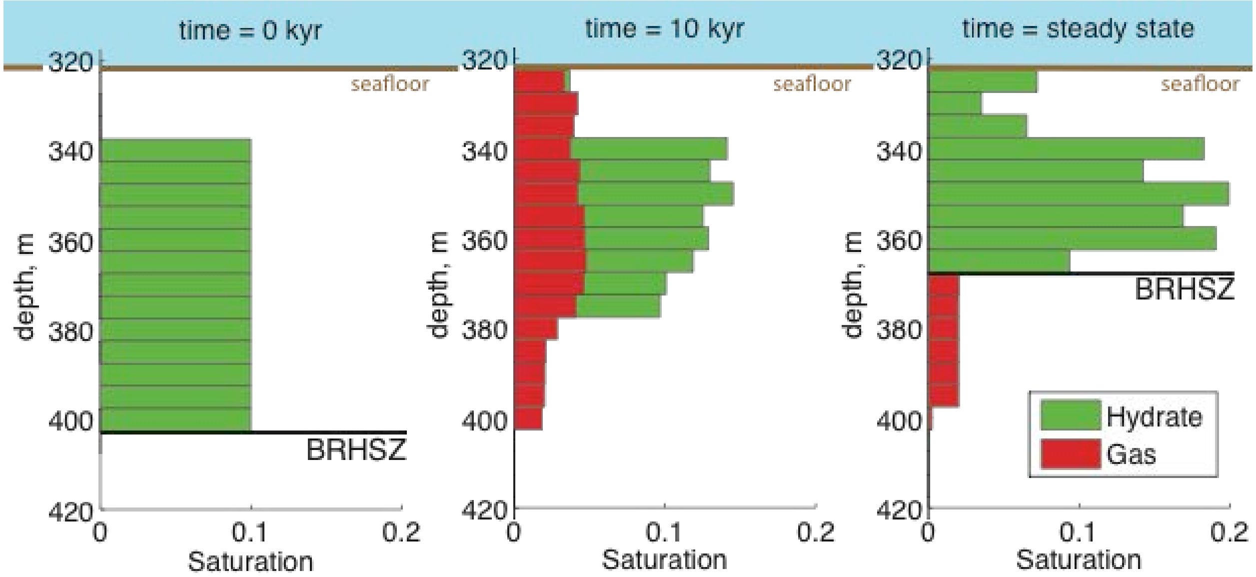

Figure 6: Saturation evolution from Case 2. The time progression goes from left to right. Green represents hydrate and red represents gas. The base of the regional hydrate stability zone is indicated with a horizontal line.

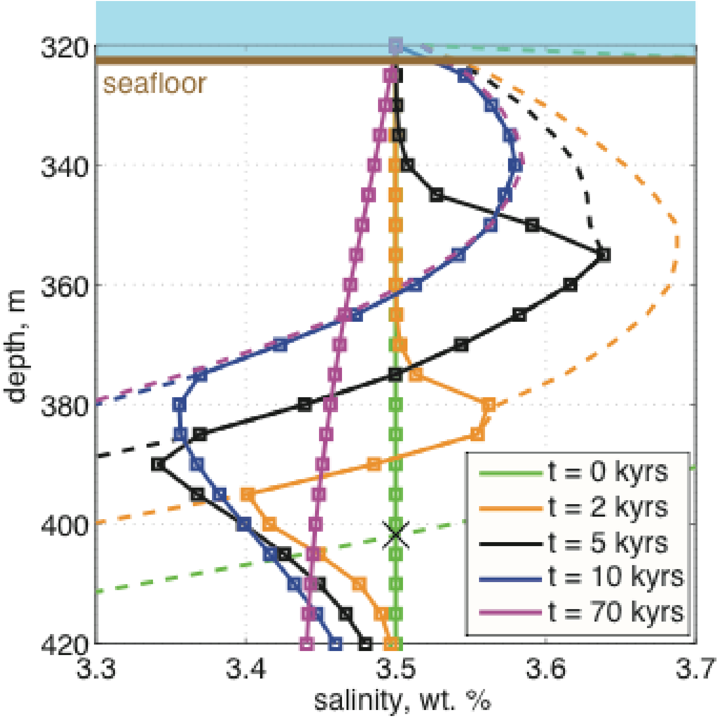

Figure 7: The salinity evolution in Case 2. The salinity at the time slice is plotted as a line with squares. The salinity required to achieve three-phase equilibrium is plotted as a dashed line. There is a source of fresh water where dissociation occurs, and there is a source of salt where secondary hydrate formation occurs.

Salinity effects:

The general hydrate deposit evolution can be seen in Figure 7, which shows the salinity profiles at the same time slices as before. During dissociation, the salinity decreases due to the release of fresh water. During formation, the salinity increases from the expulsion of salt in the hydrate structure. These salinity changes are largely responsible for the unique venting behavior shown in Case 2. The hydrate stability temperature is a function of pressure and salinity, with lower salinity raising the stability temperature and with higher salinity lowering the stability temperature. In this way, the hydrate formation is a self-limiting process. With continued hydrate production, the pore-water will eventually become too saline and free gas will be stable in the presence of hydrate.

Venting:

We also show graphically how the gas venting varies over time in Figure 8. For Case 1, no venting occurs, whatsoever. However, as previously discussed, there is a transient pulse of gas that vents into the ocean in Case 2. This venting behavior is characterized by a sharp increase to a peak value followed by slightly less sharp decrease. This a pulse that dissipates and is not sustained throughout time. This behavior occurs over a ~5 kyr period. In Case 3, the venting occurs much sooner and at a much larger rate.

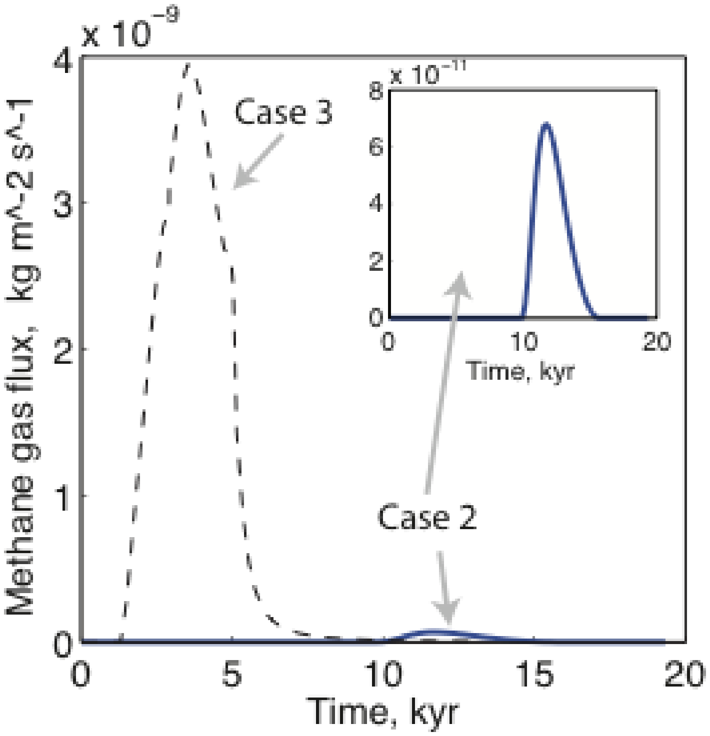

Figure 8: Gas flux venting into the ocean at the seafloor as a function of time. No gas flux for Case 2. There is a transient pulse of gas flux for Case 2 lasts ~5 kyr. In Case 3, all of the methane is vented.

2.3.2.4 Implications and Extensions

The simulation results presented show that for a given hydrate deposit there are methane losses into the ocean that are driven by the consequences of the phase changes. The volume expansion during hydrate dissociation drives gas flow upward, while the heat release and salinity increase during hydrate formation drives anomalous hydrate dissociation within the RHSZ.

We have extended the results from Case 2 to a generic environment. Our analysis shows that the behavior in Case 2 is a consequence of the changes in volume that occur during the re-organization of the system. We have shown that salinity increase that occurs during the secondary hydrate formation is the control on the three-phase behavior. Thus, we can simply calculate the changes in the hydrate stability zone from a given warming, and assess the hydrate re-organization. The threshold for transient venting as we have shown happens when the amount of dissociated hydrate exceeds the amount of hydrate required to elevate the salinity in the shortened hydrate stability zone to the three-phase equilibrium. This basic analysis demonstrates that the transient venting is a potential mechanism for venting across a wide range of water depths and temperature changes.

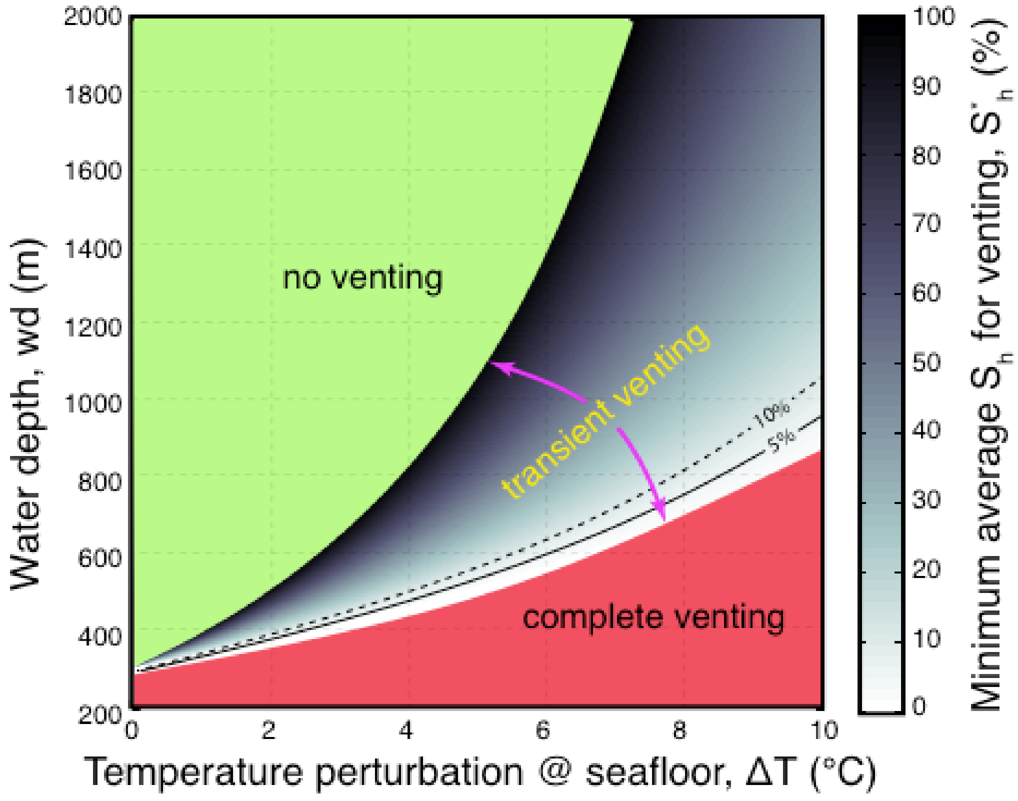

Figure 9: Gas venting potential under a given temperature increase (from assumed 0 C) and at a given water depth. The gradient shows the minimum hydrate saturation within the dissociated zone necessary to produce transient venting.

TASK 3: CATEGORIZE STABILITY OF KNOWN HYDRATE RESERVOIRS

Projected Finish: 9/30/13

Actual Finish: 9/30/13

MILESTONE 1.D DETERMINATION OF WHAT HYDRATE RESERVOIRS ARE AT THREE-PHASE EQUILIBRIUM.

SUMMARY

We constrained the in situ temperature, pressure, and salinity at 4 locations: 1) ODP Site 1249A (offshore Oregon), 2) IODP Site U1328A (offshore Vancouver), 3) NGHP Site 01-10A (Krishna-Godavari Basin, off the eastern coast of India), and 4) at Mallik Site 5L-38 (Mackenzie River Delta in the Northwestern Territories, Canada). ODP Site 1249A and NGHP Site 01-10A have elevated in situ salinities near or at the three-phase boundary for a large portion of the GHSZ, indicating that portions of these systems are at three-phase equilibrium. Mallik has locally elevated salinities documenting three-phase equilibrium within the GHSZ. IODP Site U1328A has elevated salinities, but only for a small portion of the GHSZ and it does not appear that any portion of the sediment within the GHSZ is at three-phase equilibrium. A significant discovery is that we have shown that there are examples both on land and in the ocean basin where there is evidence within the gas hydrate stability zone (GHSZ) that the system is at three phase stability: salinity is elevated enough that gas, water, and hydrate can be present.

3.1 INTRODUCTION

Gas hydrate is a chemical compound consisting of a gas trapped within the crystalline lattice of ice. Hydrate is stable at high pressures and low temperatures and salinities (Figure 10) and can contain various types of low molecular weight gases, though in natural systems it is primarily occupied by methane (Kvenvolden, 1988). Hydrate systems have been identified in submarine sediments along continental margins around the world, primarily through the presence of a bottom-simulating reflector (BSR), but also in recovered cores (Kvenvolden, 1993; Shipley et al., 1979). The combined volume of methane gas stored globally in these hydrate systems is estimated to range from 1 to 5 $\times 10^{15}$ m^3, at standard temperature and pressure (Milkov, 2004).

Along with the potential economic importance of a methane reservoir this size, the possible release of the methane from these systems due to climate change (Dickens, 2003; Wright et al., 2005) has both environmental and geohazard implications. The release of large amounts of methane, a potent greenhouse gas, into the ocean could cause a significant rise in atmospheric concentrations, exacerbating the effects of global warming (Archer et al., 2004; Dickens, 2003; Kvenvolden, 1988). Also, the introduction of large amounts of free gas into submarine sediments could significantly destabilize continental slopes and could cause an increased frequency and severity of tsunamogenic submarine landslides (Kayen and Lee, 1991; Mienert et al., 2005; Nixon and Grozic, 2007; Paull et al., 1996).

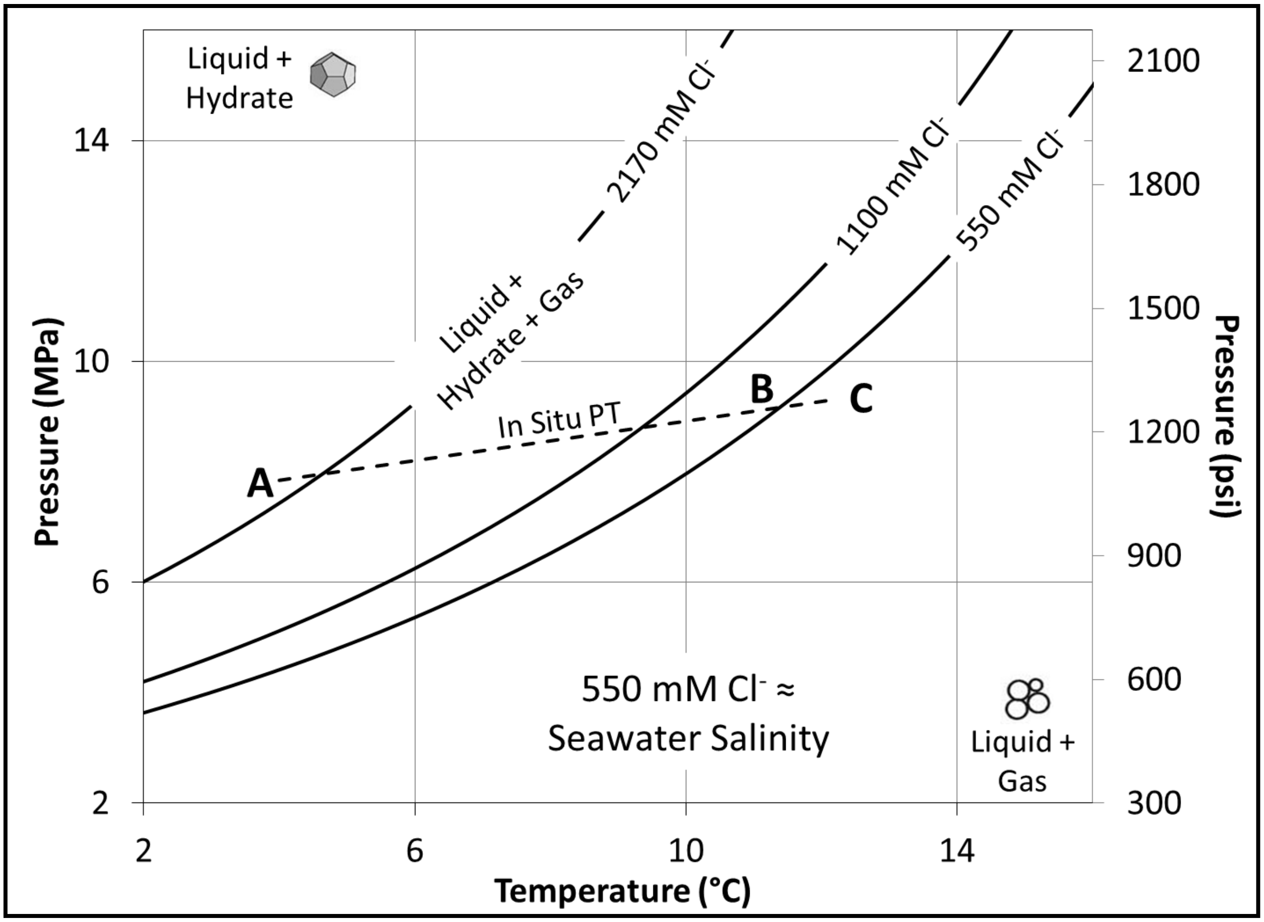

Figure 10: Phase diagram for Structure I methane hydrate. Plots pressure-temperature (PT) conditions required for three-phase equilibrium at various pore-water salinities. Dashed line is an example PT profile where depth increases from A to C and B marks the phase transition boundary as seawater salinity. As salinity increases, the three-phase equilibrium conditions change to high pressures and lower temperatures, moving up the in-situ PT profile.

Commonly, the in-situ conditions of the gas hydrate stability zone (GHSZ) are described by assuming constant geothermal and hydrostatic gradients and pore-water salinity within the system (Figure 11a, b, and c). The intersection between the in-situ salinity and the thermodynamically-defined three-phase salinity marks the depth to the base of the GHSZ. As a result, the traditional concept of submarine gas hydrate systems consists of a three-layer model (Figure 11d). The top layer extends from the seafloor to the base of the GHSZ where hydrate and water (L + H) are stable. The bottom layer consists of all the sediment below the GHSZ where free gas and water (L + G) are stable. The middle layer defines the three-phase boundary where hydrate, free gas, and water (L + G + H) are all stable. This boundary is commonly identified by the BSR (Schmuck and Paull, 1993).

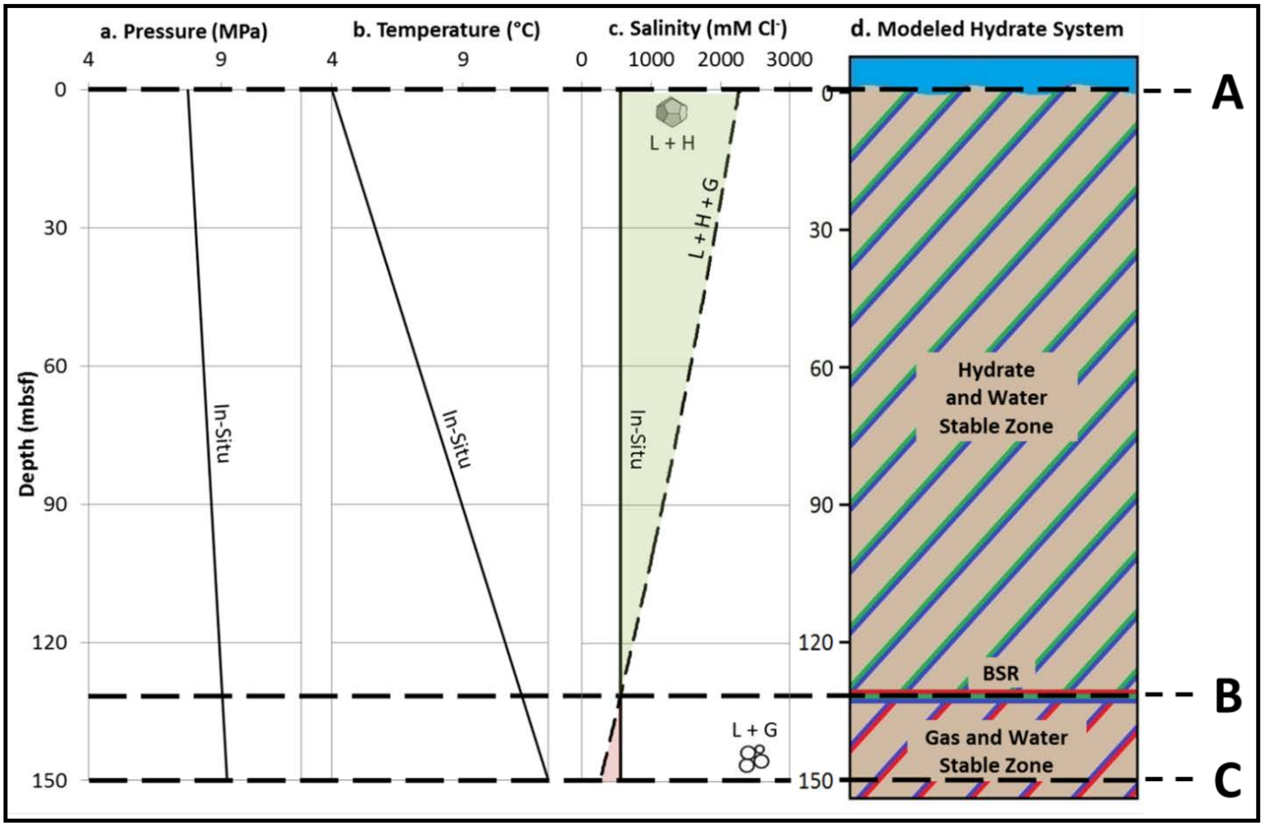

Figure 11: Traditional model of a submarine hydrate system. Solid lines mark the assumed in-situ conditions. Dashed line marks the salinity required for three-phase equilibrium. Intercept between these lines indicates the depth to the base of the GHSZ, marked by the BSR. Depths marked A, B, and C refer to the in-situ PT profile in Figure 1. a) In-situ pore pressure is determined by assuming a constant hydrostatic pressure gradient and no overpressure development. b) In-situ temperature is determined by assuming a constant geothermal gradient, controlled by the conduction of heat from below where heat flow and the thermal conductivity of the sediment are constant. c) In-situ salinity of the pore-water is assumed to be constant and equal to seawater salinity. d) Modeled structure of a hydrate system with these assumed conditions. Two 2-phase regions separated by a three-phase boundary.

The occurrence of seafloor gas vents at many sites (Haeckel et al., 2004; Heeschen et al., 2003; Torres et al., 2011; Trehu et al., 2004) requires the presence of gas within the GHSZ and indicates that the thermodynamic conditions may vary from the classic model described above. These observations have led researchers to further explore the in-situ conditions of these systems. Haeckel, et al. (2004) identified the presence of anomalously high salinities from cores taken at Hydrate Ridge, offshore Oregon, despite hydrate dissociation and subsequent “freshening” of the pore-waters (Lu et al., 2005; Wright et al., 2005). Milkov, et al. (2004) degassed a pressure core from 14 meters below the seafloor (mbsf) at this site and determined that the in-situ salinity at that depth was approximately 1630 mM Cl^- (~3 times greater than seawater). Torres, et al. (2011) discussed six sites in the Krishna-Godivari Basin, Ulleung Basin, and offshore Vancouver Island, similar to Hydrate Ridge, that also recorded elevated core-derived salinities. These studies suggest that assuming a constant, sea water salinity with depth may not accurately represent the in-situ salinity. Elevated salinities within the GHSZ can cause the three-phase equilibrium boundary to migrate toward higher pressures and lower temperatures (Figure 10), altering the thermodynamic state of the system.

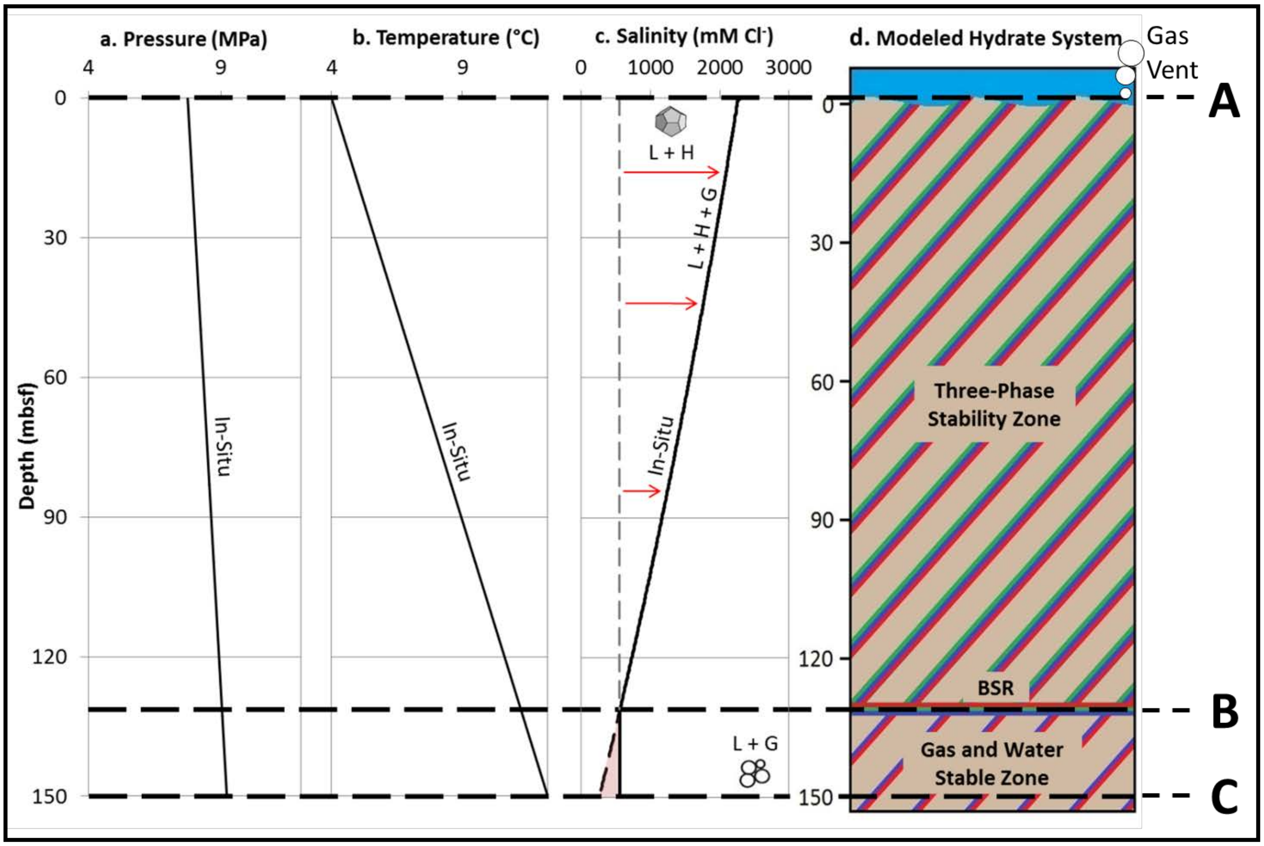

Figure 12: Alternative model of a submarine hydrate system that includes the effect of elevated salinities on in-situ thermodynamic state. Solid lines mark the assumed in-situ conditions. Dashed line marks the salinity required for three-phase equilibrium. Intercept between these lines indicates the depth to the base of the GHSZ, marked by the BSR. Depths marked A, B, and C refer to the in-situ PT profile in Figure 1. a) In-situ pore pressure is determined by assuming a constant hydrostatic pressure gradient and no overpressure development. b) In-situ temperature is determined by assuming a constant geothermal gradient, controlled by the conduction of heat from below where heat flow and the thermal conductivity of the sediment are constant. c) In-situ salinity of the pore-water is variable throughout the GHSZ and will elevate to the three-phase equilibrium as hydrate forms. d) Modeled structure of a hydrate system with these assumed conditions. Elevated salinities create three-phase equilibrium conditions throughout the GHSZ, such the system now consists of a three-phase region, below which hydrate is not stable.

The mechanism behind the observed hypersaline environments in these hydrate systems is likely salt exclusion during hydrate formation (Hesse and Harrison, 1981). This process alters the relative concentrations of water and salts in the pore space by incorporating water into the hydrate structure while forcing salt back into the remaining pore-water. Theoretically, with enough hydrate formation and subsequent increase in salinity, three-phase equilibrium could be maintained through a significant portion of the GHSZ. In this state, the BSR would no longer mark a thin, distinct boundary at three-phase equilibrium, as in the traditional model, but the base of a relatively thick three-phase zone within the GHSZ (Figure 12), explaining the presence of gas within the GHSZ.

We constrain the in situ temperature, pressure, and salinity at each study site to estimate the phases that can be present based on equilibrium thermodynamic calculations. We report the in situ salinity and hydrate saturation and evaluate the thermodynamic state within the GHSZ at four locations. Two of the sites have elevated in situ salinities near or at the three-phase boundary for a large portion of the GHSZ, indicating that portions of these systems are at three-phase equilibrium. One site has locally elevated salinities documenting three-phase equilibrium within the GHSZ. The final site has elevated salinities, but only for a small portion of the GHSZ and not near the three-phase boundary.

3.2 DETERMINATION OF IN SITU HYDRATE SATURATION AND PRESSURE, TEMPERATURE, AND SALINITY CONDITIONS

In order to assess the overall thermodynamic state of a hydrate system, the in-situ pressure, temperature, and salinity must be determined throughout the GHSZ. The in-situ pressure and temperature are used to define the salinity required for three-phase equilibrium, which marks the boundary between the hydrate stable and gas stable zones. The in-situ salinity can then be compared to the three-phase salinity to determine the thermodynamic state of the hydrate system with depth.

3.2.1 Determination of in-situ pressure and temperature

We follow the common assumption of previous research and assume a hydrostatic gradient and that no overpressure is developing within the sediments. Therefore, we calculate pore pressure (u) at a particular depth within the GHSZ using Equation 20:

$$u = (\rho_{sw} \cdot g \cdot Z_{wd}) + (\rho_{pw} \cdot g \cdot Z) = \rho_{sw} \cdot g \cdot (Z + Z_{wd}). \qquad \text{Eq. 20}$$

Z_{wd} is the water depth at the site, Z is the depth within the GHSZ, ρ_{sw} is the average density of seawater (1.023 g/cm^3), g is gravitational acceleration (9.81 m/s^2), and ρ_{pw} is the assumed density of the pore-water. The density of water can vary depending on its salinity and temperature. The potential effect of this density change on the pore pressure, however, is relatively small, so we assume that the pore-water density is equal to seawater density.

We calculate the in-situ temperature (T) at a particular depth within the GHSZ using Equation 21:

$$T = T_b + (Z \cdot G_g). \qquad \text{Eq. 21}$$

T_b is the temperature at the seafloor, and G_g is the geothermal gradient for the site. Geothermal gradient is controlled by the thermal conductivity and heat flow of the material below the seafloor (Henninges et al., 2005) and can be determined using downhole temperature probes.

3.2.2 Determination of in-situ salinity

The core-derived salinities are usually presumed to equal the in-situ values. The presence of hydrate, however, can result in elevated in-situ salinities. The dissociation of that hydrate releases fresh water back into the pore space, decreasing the salinity and invalidating this assumption. In this case, we determine the in-situ salinity using a method similar to that implemented by Malinverno, et al. (2008), which calculated the in-situ hydrate saturation from pore-water freshening. We assume a two-phase system where only free water, of saturation S_w, and hydrate, of saturation S_h, exist, such that:

$$S_h = 1 - S_w. \qquad \text{Eq. 22}$$

We also assume that the total pore volume does not change with hydrate formation and that the system is closed to diffusion and advection, meaning that the salt is immobile (Liu and Flemings, 2006). With these assumptions, we calculate the in-situ salinity ($C_{in\text{-}situ}$) with a volumetric correction (Eq. 23) between the core-derived salinity (C_0) and the water saturation:

$$C_{in-situ} = \frac{C_0}{1 - S_h} = \frac{C_0}{S_w}. \qquad \text{Eq. 23}$$

2.3 Determination of in-situ water saturation

We determine the water saturation using Archie's Law (Archie, 1941):

$$S_w = \sqrt[N]{\frac{a \cdot \rho_w}{n^m \cdot \rho_t}}. \qquad \text{Eq. 24}$$

N is the saturation exponent, a is the tortuosity coefficient, ρ_w is the pore-water resistivity, n is the porosity, m is the cementation exponent, and ρ_t is the formation resistivity. We use the RING resistivity log from the Logging-While-Drilling (LWD) data as a good estimate of the true formation resistivity (Cook et al., 2012). Porosity is calculated using a density equation:

$$n = {(\rho_m - \rho_b)}\Big/{(\rho_m - \rho_f)}. \qquad \text{Eq. 25}$$

Where ρ_m is the average grain density derived from the core moisture and density data, ρ_f is the assumed constant fluid density for each study site, and ρ_b is the bulk density derived from the LWD density log.

The pore-water resistivity is dependent upon the temperature and salinity of the water and is calculated using Arps' Equation (Arps, 1953):

$$\rho_w = 0.0123 + \left(\left(\frac{3647.5}{C^{0.955}}\right) \cdot \frac{45.4}{(T_f + 21.5)}\right). \qquad \text{Eq. 26}$$

Where T_f is the fluid temperature, determined using Equation 21, and C is the salinity of the water.

We determine the tortuosity coefficient (a) and cementation exponent (m) for each site based on resistivity and porosity measurements where water is the only phase present (S_w = 1). With this assumption, Equation 24 simplifies to:

$$F = \frac{\rho_t}{\rho_w} = a \cdot n^{-m}\,. \qquad \text{Eq. 27}$$

Where F, termed the formation factor, is the ratio of formation resistivity to pore-water resistivity. A power law regression is taken from a cross-plot between porosity and formation factor (Pickett plot) and is used to infer the values of a and m. We limited the values of a and m to be between 0.5 – 1.5 and to be greater than 1, respectively (Crain, 2013).

To ensure that the points chosen to determine a and m are from material that is fully water saturated, we only use data points that are from below the GHSZ and that are not associated with anomalously low log-derived density. We also remove data points that have a bulk density correction log greater than ±0.25 g/cm^3 or a caliper log that exceeds the bit diameter by greater than 1 cm (0.394 in). These conditions are applied not only to ensure that the points represent water-saturated sediments, but also to remove points where borehole conditions may have compromised the log data accuracy.

The value of the saturation exponent in hydrate-saturated sediments is a topic of considerable debate. Pearson, et al. (1983) shows that N was equal to approximately 2 for various water-saturated sandstones. Hydrate-bearing sediment, however, experiences physical changes as hydrate precipitates and therefore does not act like a clean, water-saturated sandstone. Spangenberg (2001) suggested that N can range from 0.5 to 4 and that the value was dependent on many factors, including: whether hydrates are isopachous or pore-filling, the degree of hydrate saturation, and the significance of capillary effects. Spangenberg suggests that, regardless of the other factors, N increases at greater hydrate saturations. We assume an N-value of 4 for all study sites, because our region of interest is associated with significant hydrate saturations.

We use an iterative application of Archie's Law (Eq. 24) and the salinity correction (Eq. 23) to determine the in-situ water saturation and salinity. The water saturation is calculated for the first iteration using the core-derived salinity. This salinity is then corrected and used in the following iteration to recalculate the water saturation. The saturation from the current iteration is then used to re-correct the core-derived salinity for the following iteration. This process is repeated for 10 iterations, though we found that the calculated water saturation and in-situ salinity leveled off (ΔS_w < 1%) after 4 to 5 iterations.

During this procedure, linear interpolation was required to account for the different sampling resolutions of the log and core-derived data. The logged data resolution ranged from 3.05 – 15.24 cm (1.2 – 6 in), depending on the site and logging tool, while the core was sampled every 208 – 493 cm (81.9 – 194.1 in). To account for this difference, this iterative application of Archie's law is run using two modes of linear interpolation at each site. The first mode interpolates between the core-derived salinities to determine a unique salinity value for each resistivity data point. This method produces a hydrate saturation and salinity curve at the same resolution as the resistivity data. The second mode interpolates between the resistivity measurements to determine a unique resistivity value for each salinity sample. This mode produces a hydrate saturation and salinity profile for each available salinity data point. The results from both of these interpolation modes are shown in the results for each site as gray or black lines for the resistivity resolution data and red dots for the salinity resolution data.

3.2.3 Determination of three-phase salinity

We calculate the salinity necessary to maintain three-phase equilibrium throughout the GHSZ for the interpreted temperature and pressure profiles at each study site. At any particular depth, we define this salinity as the point where the solubility of methane gas in water in a liquid-gas phase system (Duan et al., 1992) and liquid-hydrate phase system (Henry et al., 1999), at the unique in-situ pressure and temperature conditions, are equal. This model was described by Liu and Flemings (2006) and showed good agreement with stability conditions produced by the CSMHYD hydrate program (Sloan, 1998).

3.3 STUDY SITES

3.3.1 Analysis of well log and core-derived data

Each study site was chosen for the availability of necessary log and core data as well as the confirmed presence of hydrate within the logged portion of the well. The standard suite of log data included the gamma ray, caliper, resistivity, bulk density, photoelectric factor, and neutron porosity tools. Some logs were not essential to our calculations and are therefore are not displayed in the well log montages. We analyze the LWD and core data to infer the presence of hydrate and the dominant lithology and to determine if salt diffusion or advection is significantly affecting the in-situ salinity.

Hydrate presence is inferred using the resistivity and bulk density logs. Gas hydrate is a highly resistive material that complicates the conductive pathway, increasing tortuosity and the measured resistivity (Collett and Ladd, 2000; Cook et al., 2010; Pearson et al., 1983). Also, gas hydrate has a density equal to approximately 0.925 (Collett et al., 2012), which is less than seawater. The formation of gas hydrate could result in a decrease in measured bulk density as the greater density pore fluid is replaced by the significantly less dense hydrate. Therefore, we infer the presence of hydrate wherever the resistivity increases and bulk density decreases together.

The general lithological trends within a well are determined from the gamma ray log and core samples. The gamma ray tool responds to changes in grain size distribution, recording larger gamma ray values (GAPI) in finer-grained sediment (Serra, 1984). This information is used to identify interbedded fine-grained and coarse-grained material and directional-fining sequences. The core samples allow for a more complete characterization of the lithology, but sacrifice data resolution. These data are used to calibrate and confirm the analysis performed on the gamma ray log.

We determine the validity of the “closed system” assumption from the core-derived salinities. In an open system, the excess in-situ salt will be reduced back to baseline values through diffusion and advection, while in a closed system it will remain in the pore space. When the core is removed from the in-situ conditions and hydrate dissociates, fresh water will flow back into the pore space, freshening the pore-water. With open conditions the core-derived salinities would be significantly below seawater, while with closed conditions the pore-water would freshen back to the baseline salinity. Therefore, we interpret the system to be “closed” if the core-derived salinities are around seawater.

3.3.2 ODP Site 1249A

ODP Site 1249A (Figure 13) was drilled on the southern summit of Hydrate Ridge, offshore Oregon (44º 34.237’N, 125º 8.841’W) to determine the abundance and distribution of gas hydrate resources at in the region and to investigate the processes that allow free gas to exist within the GHSZ. Site 1249A is located approximately 220 km southwest of Portland, Oregon in 788.5 meters of water. The well was drilled to a total depth of 90 mbsf, stopping short of the base of the GHSZ (115 mbsf) for safety concerns (Shipboard Scientific Party, 2003). A standard suite of LWD tools was run for the entire well; the relevant LWD and core-derived data from this borehole are presented in Figure 14. The baseline density and resistivity values and Archie parameters for this site were determined using LWD data from ODP Site 1250A, 305 meters to the southwest, because this hole penetrated the base of the GHSZ (Shipboard Scientific Party, 2003). Archie’s parameters, *a* and *m*, were determined to equal 1.50 and 1.89, respectively (Table 1, Figure 15).

The resistivity log for ODP Site 1249A has a baseline value of 1.1 ohmm. From 0 – 21 mbsf, the resistivity increases log-linearly from the baseline to 110 ohmm. Between 21 – 47 mbsf, the resistivity is consistently elevated to an average of 88 ohmm with a maximum value of 214 ohmm at 34 mbsf. From 47 mbsf to the total depth, the resistivity decreases exponentially towards an average value of 2.3 ohmm. The density log has a baseline value of 1750 kg/m^3. From 0 – 47 mbsf the density is consistently lower than the baseline, ranging between 1060 – 1670 kg/m^3 and averaging 1590 kg/m^3. From 47- 64 mbsf, the density increases log-linearly from 1450 – 1750 kg/m3. From these analyses, we conclude that hydrate likely exists within the entire cored region of this well, with high saturations concentrated in the region between 21 – 47 mbsf. The presence of gas hydrate was confirmed through the occurrence of soupy or “mousse-like” textured sediments, caused by hydrate dissociation, infrared images, and from whole-round cores where hydrate samples were preserved (Shipboard Scientific Party, 2003).

The gamma ray log for Site 1249A increases from 40 to 60 GAPI log-linearly throughout the well, indicating a relatively consistent lithology. The low range in gamma ray measurements suggests that the lithology at this site consists of fine-grained sands and coarse-grained silty material. Core samples, however, defined two lithological units, both of which consisted of silty-clay material with thin, interbedded sandy layers. The lower section (Unit II) contained a higher frequency of thin sand layers (Shipboard Scientific Party, 2003).

At Site 1249A, the core-derived salinities range from 354 – 1008 mM Cl$^-$, averaging 556.6 mM Cl$^-$ with a standard deviation of ±44.6 mM Cl$^-$, excluding the values above 15 mbsf, where borehole washout could be affecting the pore fluid. The close proximity of the salinities to the baseline salinity indicates that the system was closed during hydrate formation.

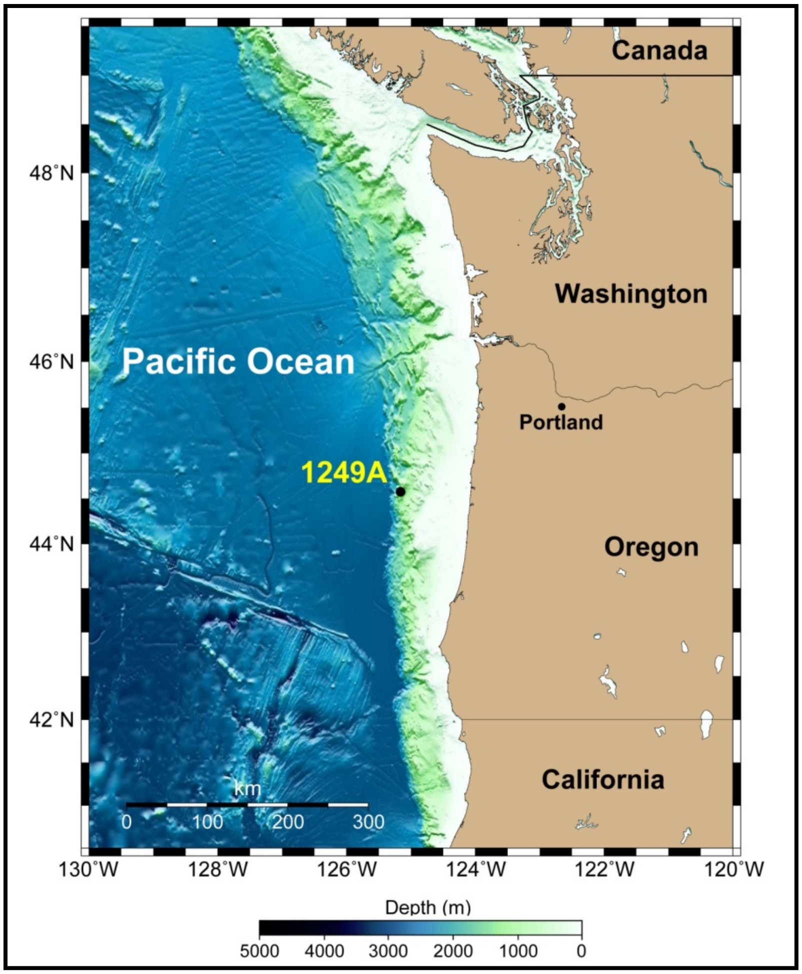

Figure 13: ODP Site 1249A is located approximately 220 km southwest of Portland, Oregon, in about 790m of water. Bathymetry data from IOC, et al. (2003).

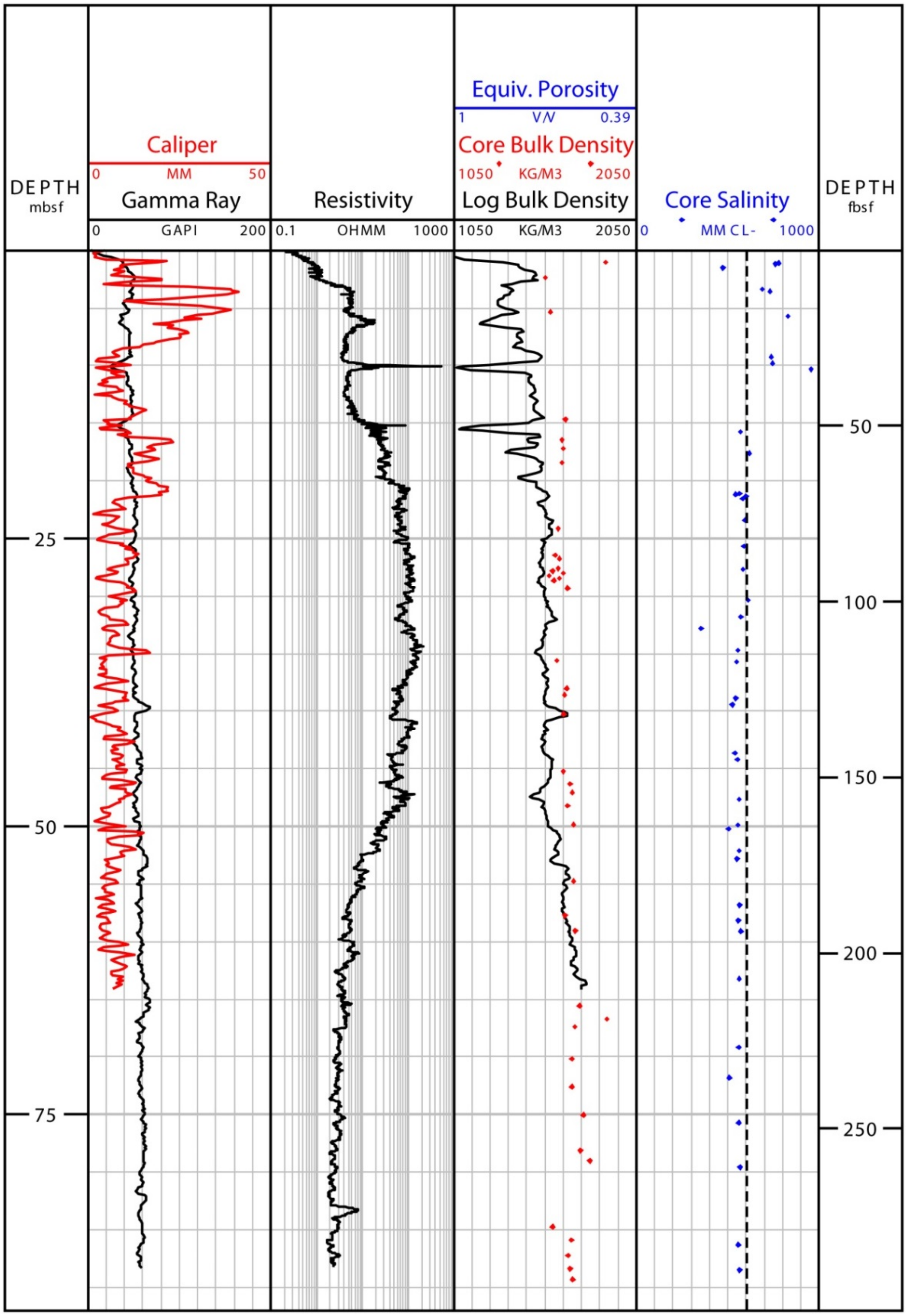

Figure 14: Montage of core and LWD data from ODP Site 1249A at Hydrate Ridge. Track 1: Gamma ray and differential caliper log; Track 2: RING resistivity log; Track 3: Core-derived and LWD bulk density. Equivalent porosity scale (assuming ρg = 2.70 g/cm3 and ρw = 1.05 g/cm3) is included for reference; Track 4: Core-derived chloride concentration. Dashed line represents average salinity of 607.7 mM Cl-.

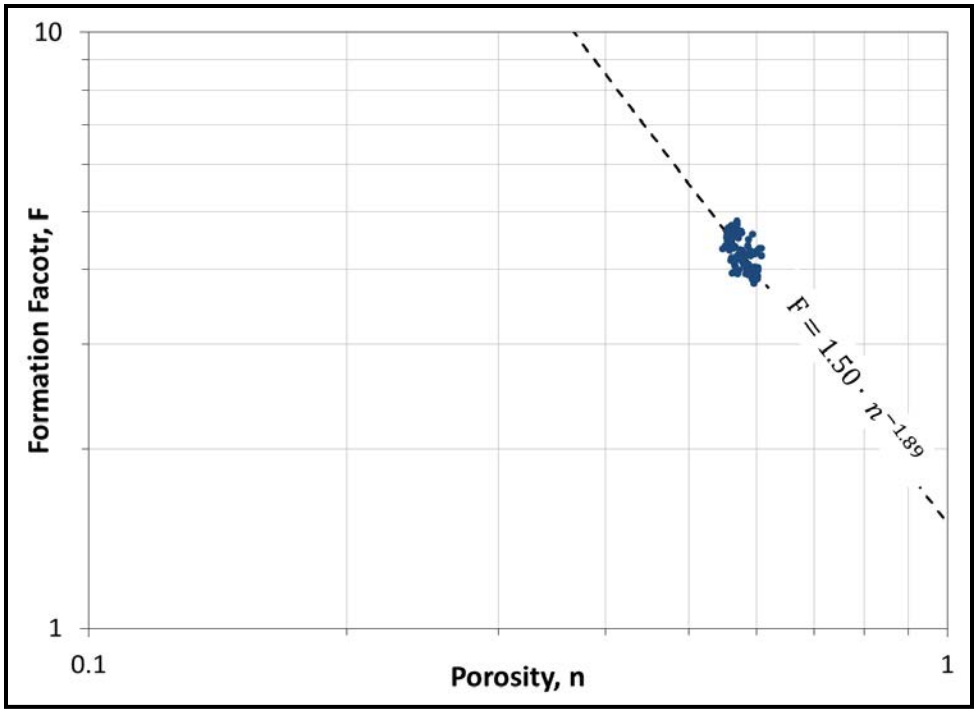

Figure 15: Pickett plot for ODP 1249A. The best fit linear regression line using water-saturated points yields the cementation exponent (m = 1.89) and tortuosity coefficient (a = 1.50).

3.3.3 IODP Site U1328A

IODP Site U1328A (Figure 16) was drilled on the mid-continental slope off of Vancouver Island (38º 40.057'N, 126 º 51.043'W) in a water depth of 1267.7 m to a total depth of 300 mbsf, penetrating the base of the GHSZ at 219 mbsf. The stratigraphy in this region is dominated by silty-clay with interbedded coarser-grained material. The presence of gas hydrate was confirmed through infrared temperature data as well as the incidence of soupy or "mousse-like" textured sediment caused by hydrate dissociation (Expedition 311 Scientists, 2006). The standard suite of LWD instruments were deployed throughout the cored section of the well (Figure 17). Archie's parameters, *a* and *m*, were determined to equal 1.48 and 1.4, respectively (Table 1, Figure 18).

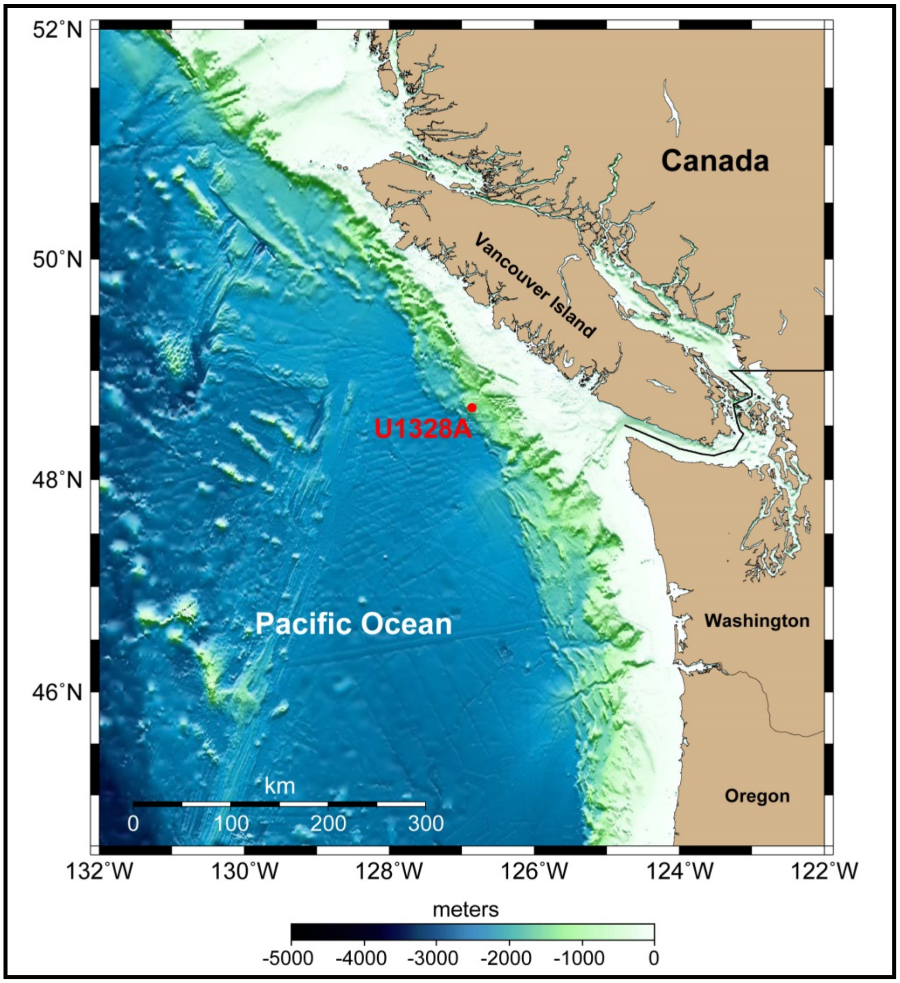

Figure 16: IODP Site U1328A is located approximately 100 km offshore Vancouver Island to the southwest, in about 1270m of water. Bathymetry data from IOC, et al. (2003).

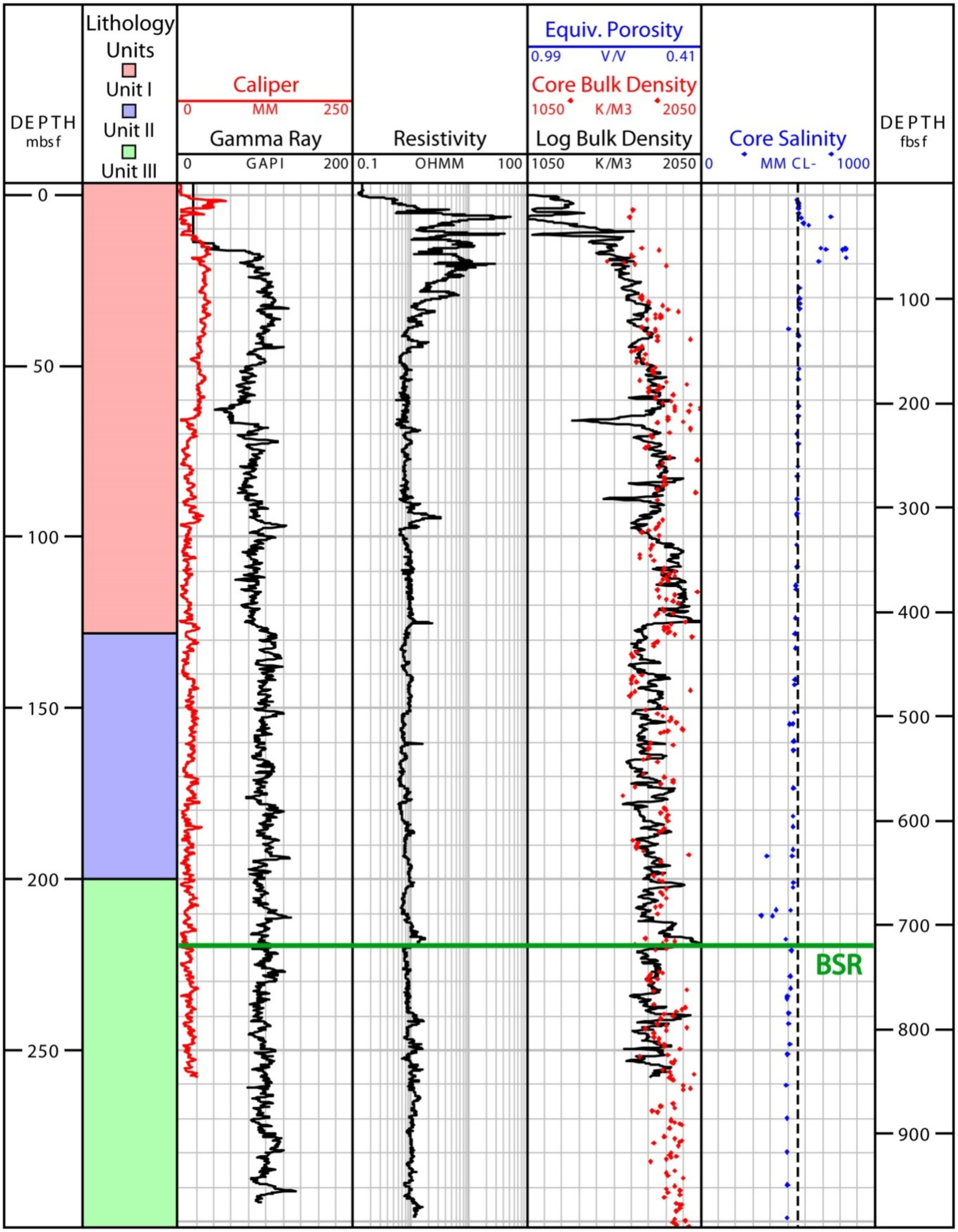

Figure 17: Montage of core and LWD derived data from IODP Site U1328A offshore Vancouver Island. Track 1 –Gamma ray and differential caliper log; Track 2 – RING resistivity; Track 3 – Core-derived and logged bulk density and equivalent porosity assuming ρ_g = 2.76 g/cm^3 and ρ_w = 1.03 g/cm^3; Track 4 – Core-derived chloride concentrations compared to the concentrations required for three-phase equilibrium.

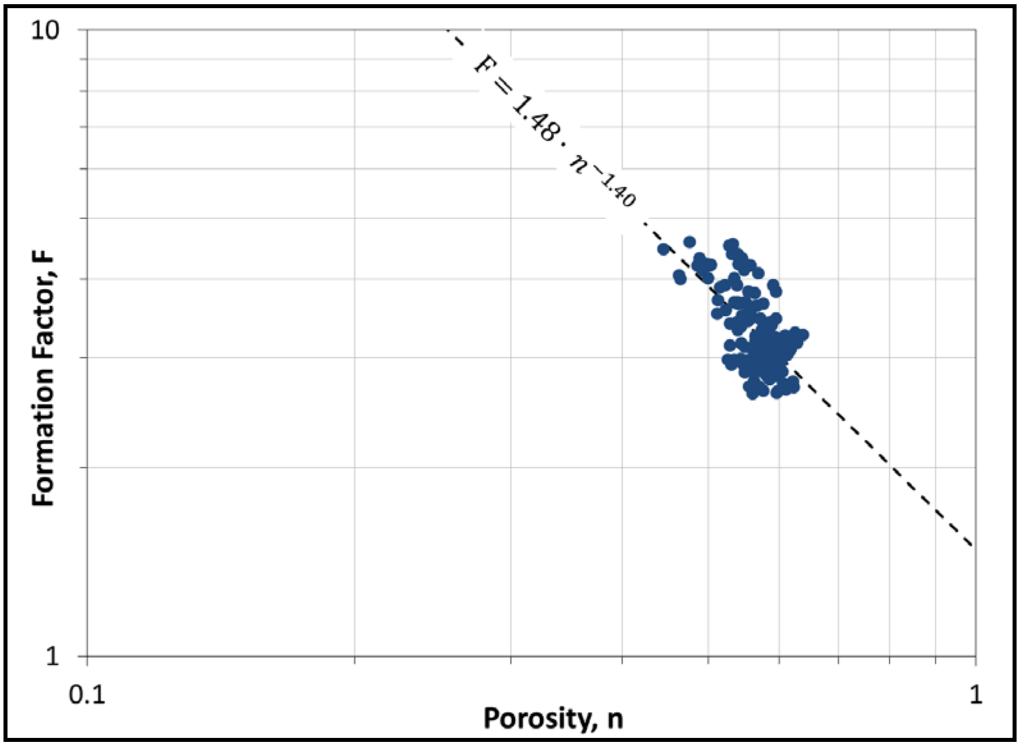

Figure 18: Pickett plot for IODP Site U1328A. The best fit linear regression line using water-saturated points yields the cementation exponent and tortuosity coefficient. At this site, *a* = 1.48 and *m* = 1.40.

3.3.4 NGHP Site 01-10A

NGHP Site 01-10A (Figure 19) was drilled in the Krishna-Godavari Basin, off of the eastern coast of India (15º 51.857’N, 81º 50.079’E) to investigate the distribution of methane hydrate resources available in that region. Site 10A is located approximately 150 kilometers southeast of Guntur, India in 1049.3 meters of water. The well was drilled to a total depth of 205.5 mbsf and penetrated the BSR at 160 mbsf (NGHP Expedition 01 Scientists, 2007). A standard suite of LWD tools was run for the entire well; the relevant LWD and core-derived data from this borehole are presented in Figure 20. Archie’s parameters, *a* and *m*, were determined to equal 1.50 and 1.62, respectively (Table 1, Figure 21). To avoid washout near the seafloor, the first 30 mbsf of the hole were drilled with low flow, rotation, and penetration rates. After 30 mbsf, the flow rate was increased until all LWD tools were activated (NGHP Expedition 01 Scientists, 2007). As a result, the data required for our calculation was only available below 22 mbsf.

The resistivity log for Site 10A increases from a baseline value of 0.94 ohmm starting at 28 mbsf, reaching a maximum value of 130 ohmm at 48 mbsf. Between 48 – 160 mbsf, the resistivity drops log-linearly from the peak value back to the baseline, excluding the region between 89 – 125 mbsf, where the resistivity drops an average of 8.3 ohmm below the this trend. Where data was available, the bulk density log ranges from 1240 – 1820 kg/m^3 with a baseline density of 1800 kg/m^3. Above the BSR, the bulk density decreased significantly from the baseline between 22 – 89 and 125 – 160 mbsf. Below the BSR, the density alternated between the baseline and a bulk density of approximately 1500 kg/m^3, which could either indicate the presence of free gas or be the result of poor borehole conditions. These data indicate that hydrate exists between 28 – 160 mbsf, but that greater saturations of hydrate occur between 45 – 90 and 125 – 160 mbsf. The occurrence of hydrate at Site 10A was confirmed in core sample cuts, infrared imaging data, and the occurrence of soupy or "mousse-like" textured sediment as a result of hydrate dissociation in core samples. Gas hydrate was observed as solid nodules, disseminated throughout the pore space, and within high-angle fractures (NGHP Expedition 01 Scientists, 2007).

The gamma ray log for Site 10A ranges between 60 -100 GAPI from 28 – 160 mbsf, with an average value of 82 GAPI, indicating that the lithology is primarily fine-grained material. The lithology from recovered cores supports this interpretation, defining a single lithological unit consisting of a clay matrix with varying occurrence of nannofossils. The core lithology also indicated the presence of authigenic carbonate cements in large portions on the well (NGHP Expedition 01 Scientists, 2007).

The core-derived salinities for NGHP Site 10A range from 397.6 – 634 mM Cl$^-$, averaging 526.6 mM Cl$^-$ with a standard deviation of ±65.3 mM Cl$^-$. The range of salinity values are relatively well distributed throughout the well, showing no particular trends correlated with lithology or hydrate presence. The close proximity of the salinities to the baseline salinity indicates that the system was closed during hydrate formation.

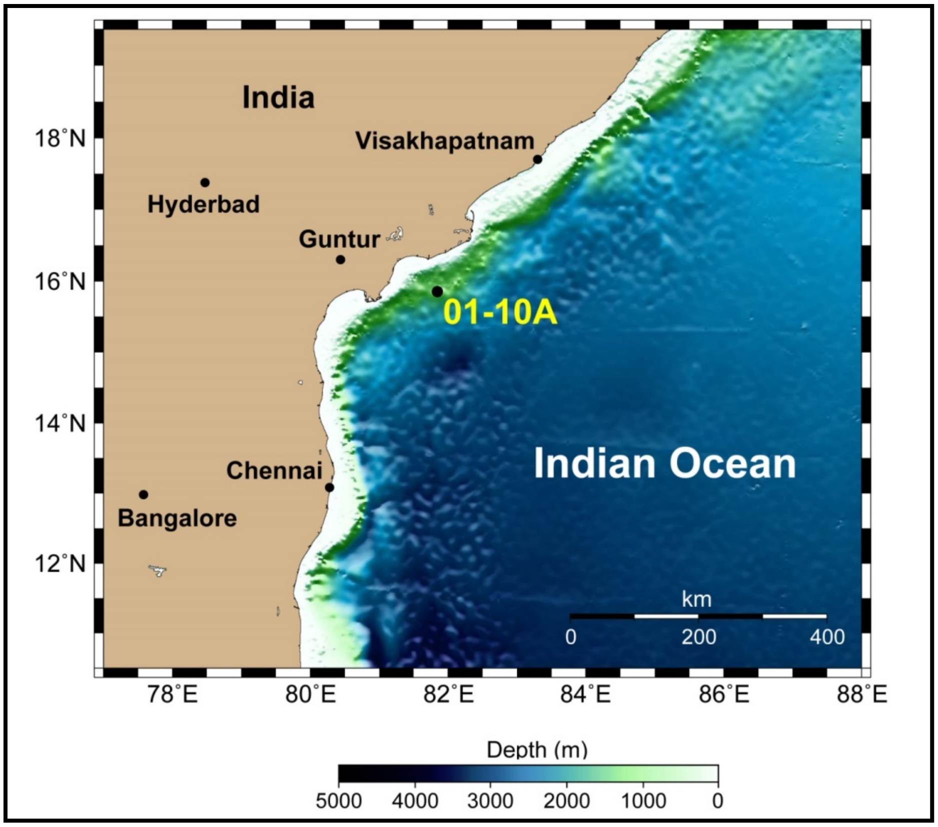

Figure 19: NGHP Site 01-10A is located approximately 150 km southeast of Guntur, India in about 1050m of water. Bathymetry data from IOC, et al. (2003).

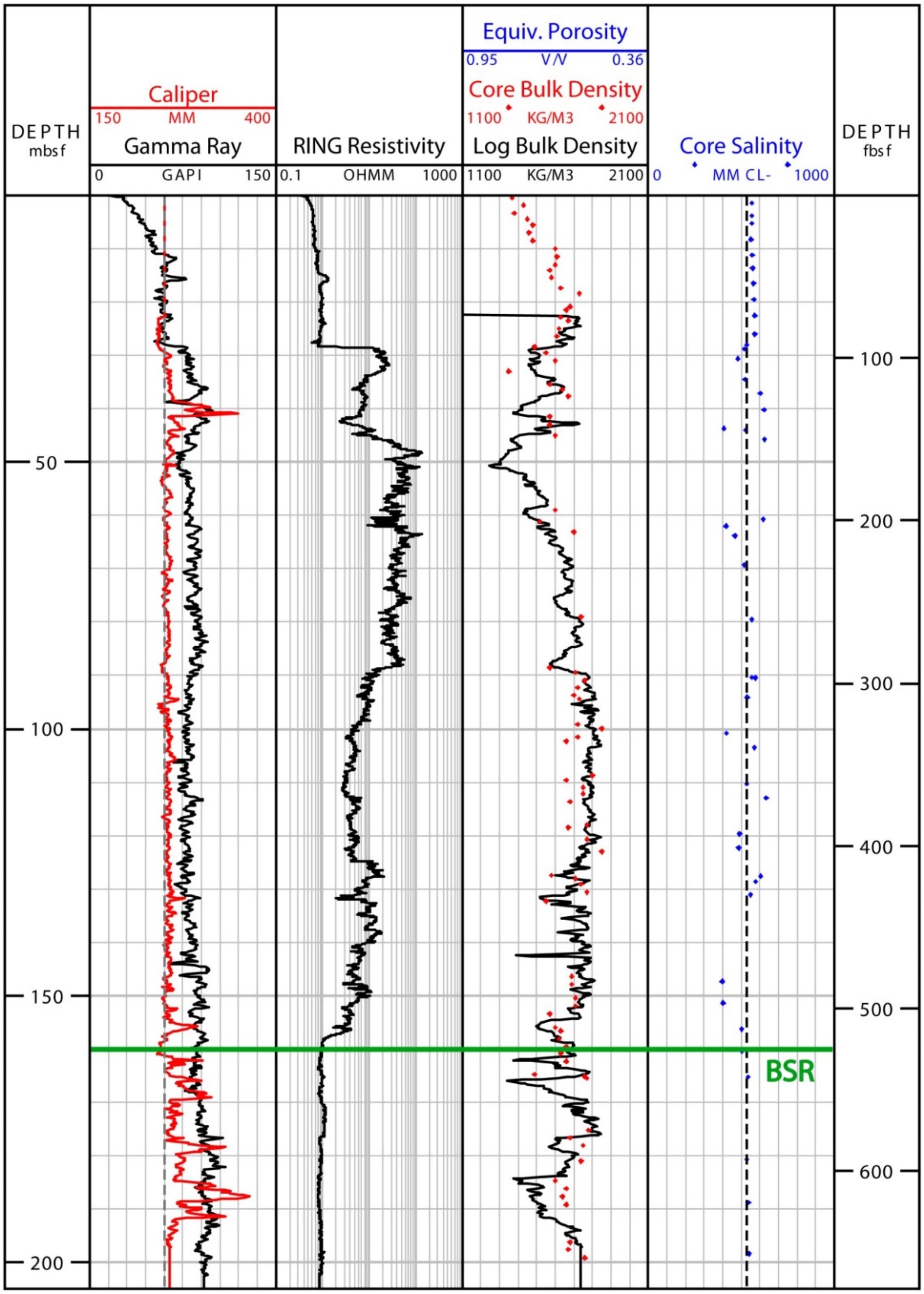

Figure 20: Montage of core and LWD data from NGHP Site 01-10A in the Krishna-Godavari Basin. Track 1: Gamma ray and caliper log (dashed line indicates bit size); Track 2: RING resistivity log; Track 3: Core-derived and LWD bulk density. Equivalent porosity scale (assuming ρg = 2.72 g/cm3 and ρw = 1.023 g/cm3) is included for reference; Track 4: Core-derived chloride concentration. Dashed line represents average salinity of 526.4 mM Cl-.

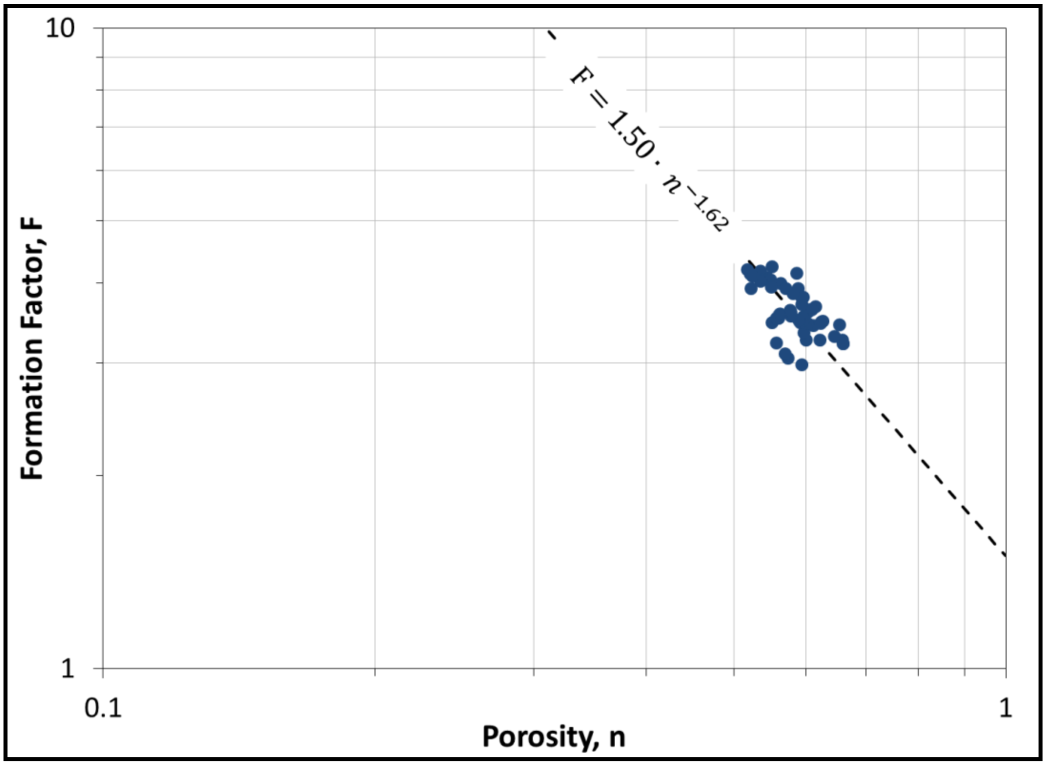

Figure 21: Pickett plot for NGHP 01-10A. The best fit linear regression line using water-saturated points yields the cementation exponent (m = 1.62) and tortuosity coefficient (a = 1.50).

3.3.5 Mallik Site 5L-38

Mallik Site 5L-38 (Figure 22) was drilled in the Mackenzie River Delta in the Northwestern Territories, Canada (69º 27.655'N, 134 º 39.648'W). The site was drilled in a water depth of 1 m to a total depth of 1166 mbsf. The upper 676.5 mbsf consists of permafrost-cemented sediment, underlain by water saturated sediment in which hydrate formed between 891 and 1107 mbsf (Collett et al., 2005; Takahashi et al., 2005). The stratigraphy within the GHSZ consists of 4 thick layers of sandy material (5 – 52 meters) seperated by thick, fine-grained silt layers (Medioli et al., 2005). The presence of gas hydrate in the area was previously confirmed in 1972 and 1998 (Bily and Dick, 1974; Collett and Dallimore, 1998; Dallimore et al., 1999) during the drilling of the Mallik L-38 and 2L-38, respectively, and was also confirmed at the 5L-38 well through the presence of hydrate in recovered cores and use of pressure core samples to specifically recover hydrate samples (Lu et al., 2005). This well was divided up into 4 distinct zones based upon the values for core-derived chloride concentrations in Matsumoto, et al. (2005) and supported by the lithology in that same study. There was an extensive wireline logging program implemented within the GHSZ at this site; the pertinent well log and core data is shown in Figure 23. Archie's parameters, *a* and *m*, were determined to equal 0.75 and 2.052, respectively (Table 1, Figure 24).

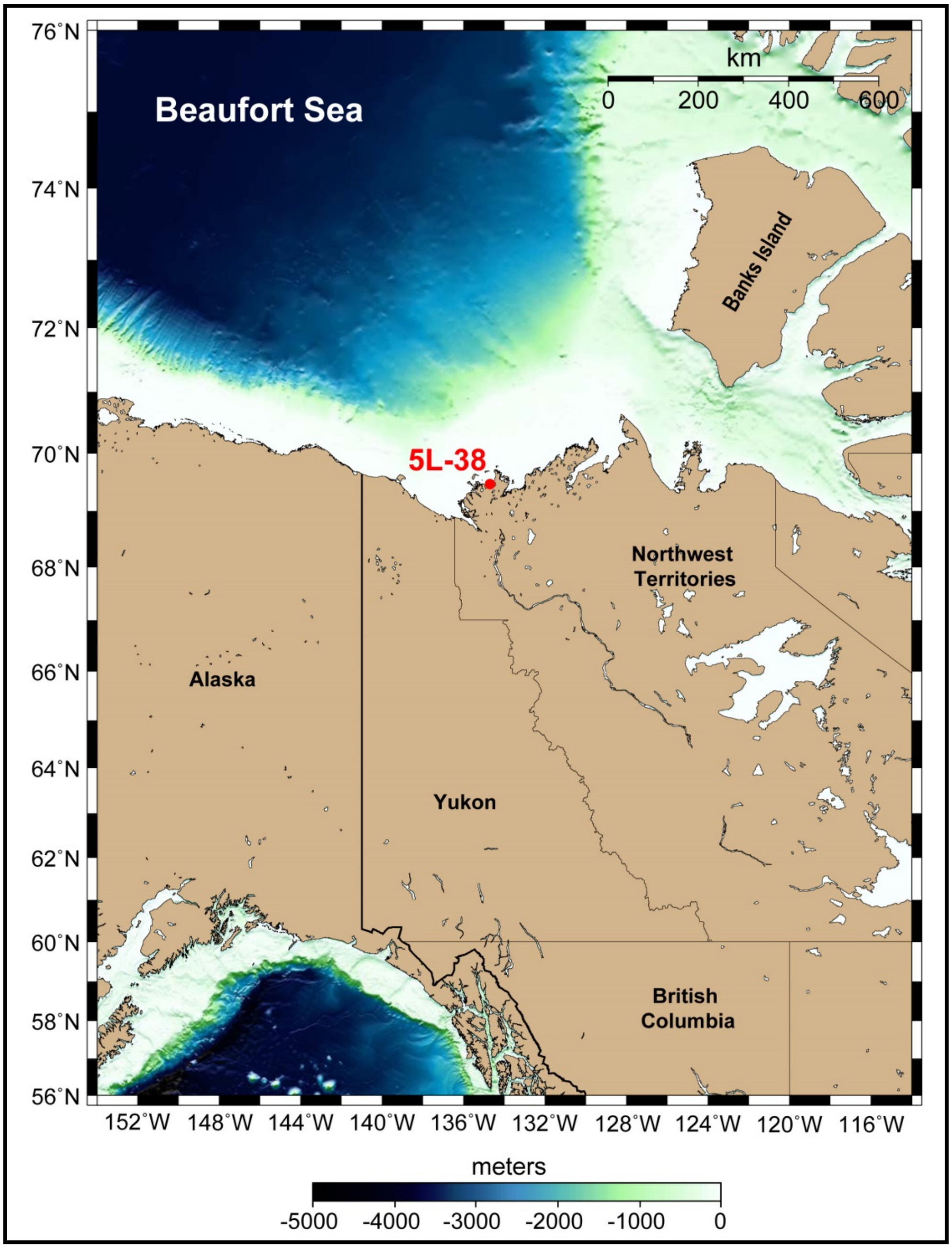

Figure 22: Mallik Site 5L-38 is located in the Mackenzie River Delta, Northwestern Territories, Canada in about 1m of water. Bathymetry data from IOC, et al. (2003).

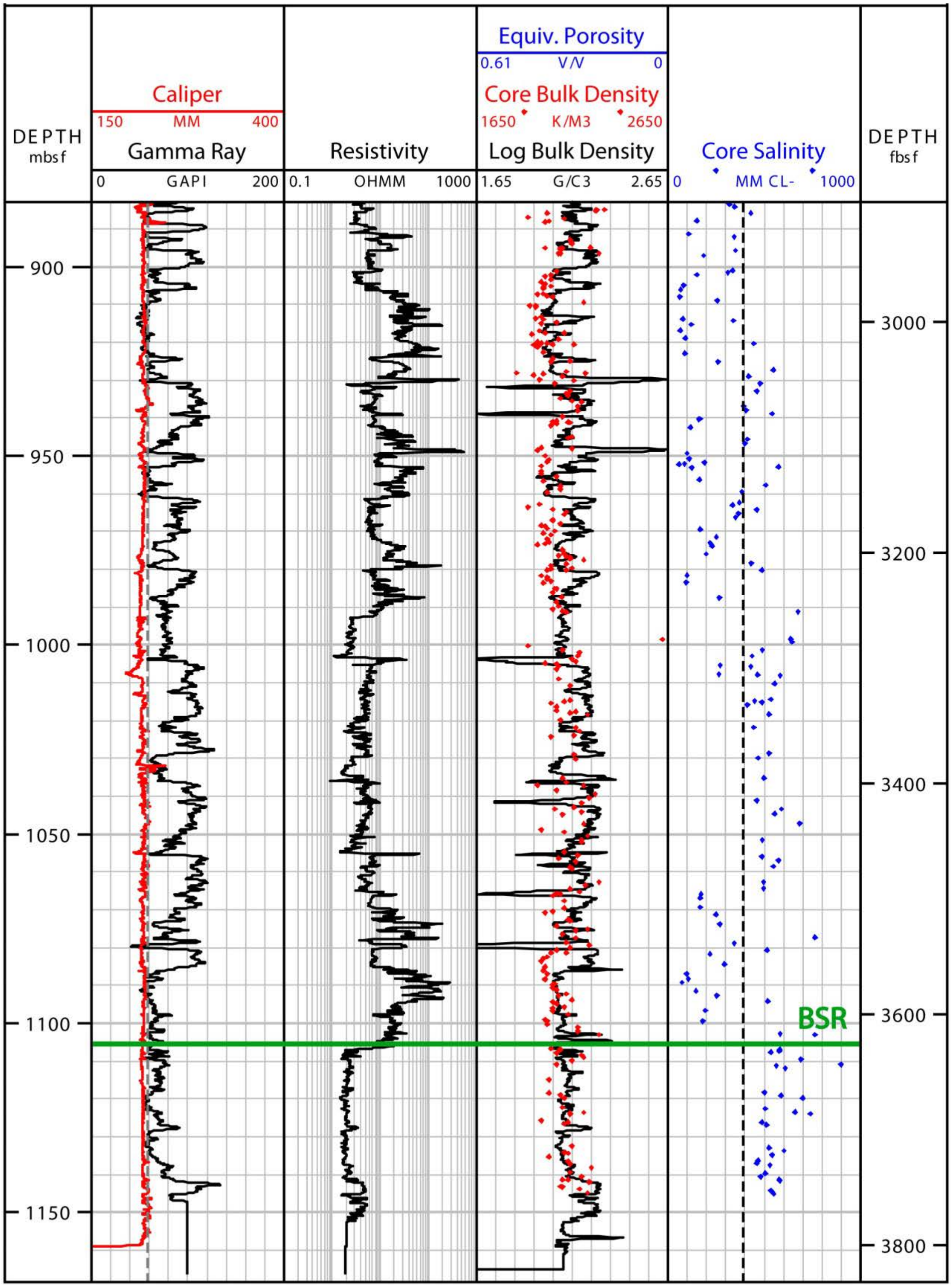

Figure 23: Montage of core and wireline derived data from Mallik Site 5L-38 in the Mackenzie Delta. Track 1 –Gamma ray and caliper log (dashed line represent the bit size for this section); Track 2 – Focus mode 5 (deep) resistivity; Track 3 – Core-derived and logged bulk density and equivalent porosity assuming ρg = 2.65 g/cm3 and ρw = 1.01 g/cm3; Track 4 – Core-derived chloride concentrations compared to the concentrations required for three-phase equilibrium.

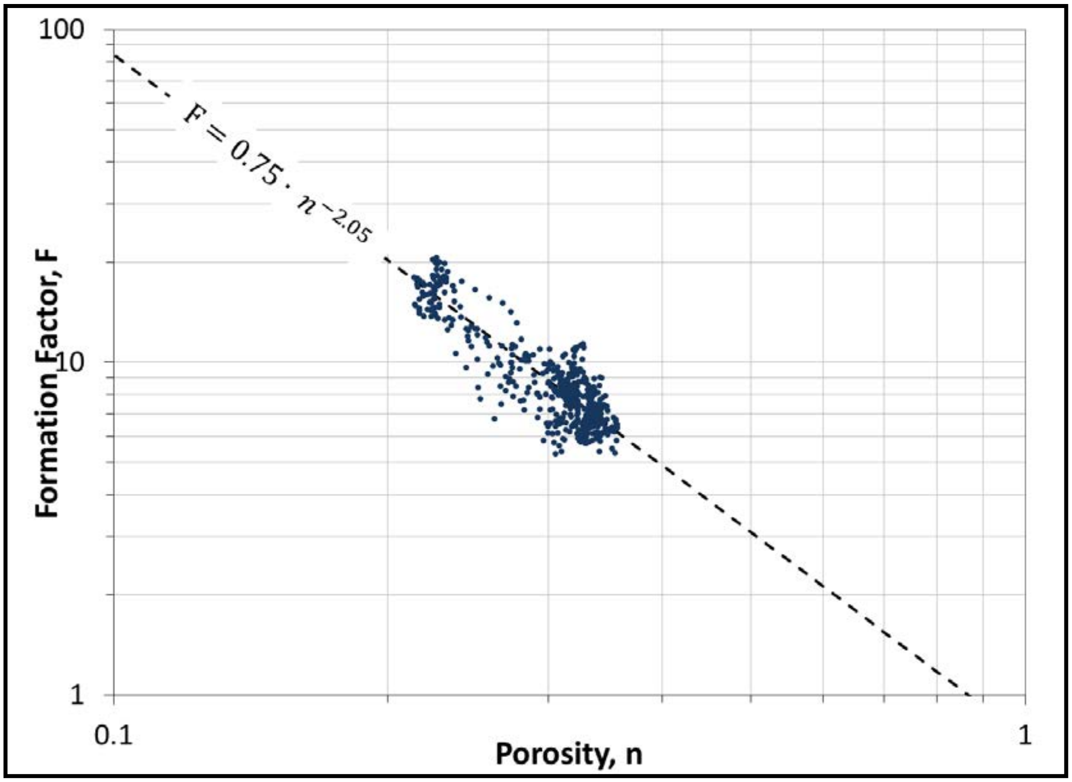

Figure 24: Pickett plot for Mallik Site 5L-38. The best fit linear regression line using water-saturated points yields the cementation exponent and tortuosity coefficient. At this site, *a* = 0.75 and *m* = 2.05.

3.4 RESULTS

3.4.1 ODP Site 1249A

At Site 1249A, the hydrate saturation averages 0.484 between 2 – 15 mbsf, excluding two peaks at 6.3 and 10 mbsf with saturations of 0.695 and 0.89, respectively. The highest hydrate saturation exists between 15 – 47 mbsf, with saturations ranging from 0.514 – 0.814 with an average of 0.733. Below 47 mbsf, the hydrate saturation reduces exponentially to an average of 0.192 in the bottom 11 meters of the well (Figure 25; Track 2).

The calculated in-situ salinities are well correlated with the hydrate saturations. An average salinity of 1580 mM Cl^- exists between 2 – 15 mbsf, approximately 2.6 times greater than the baseline salinity, excluding the two anomalous peaks at 6.3 and 10 mbsf with salinities of 2985 and 7742 mM Cl^-, respectively. Between 15 – 47 mbsf, the in-situ salinity ranges from 1316 to 2996 mM Cl^- and averages 2154 mM Cl^-, 3.54 times greater than the baseline salinity. Below 47 mbsf, the salinity decreases exponentially from 2700 mM Cl^- back to 1.25 times greater than the baseline (Figure 25; Track 3). The pressure core sample taken at 14 mbsf was determined to have an in-situ salinity of 1630 mM Cl^- (Milkov et al., 2004), which correlates well with the salinity we calculated for that depth and supports the other in-situ salinities we determined.

We qualitatively identify one thick region, between 15 – 47 mbsf, and two thin layers, from 9.8 – 10.5 mbsf and 5.7 – 7 mbsf, where the in-situ salinities are near to or exceed the three-phase boundary (Figure 25; Track 3), and interpret these regions to be at three-phase equilibrium. We believe that the two thin layers are associated with the presence of free gas, because they are both associated with a drastic decrease in bulk density and increase in resistivity that is uncharacteristic of the surrounding sediment. We still interpret these regions to be at three-phase equilibrium, however, because the salinity indicates this thermodynamic state.

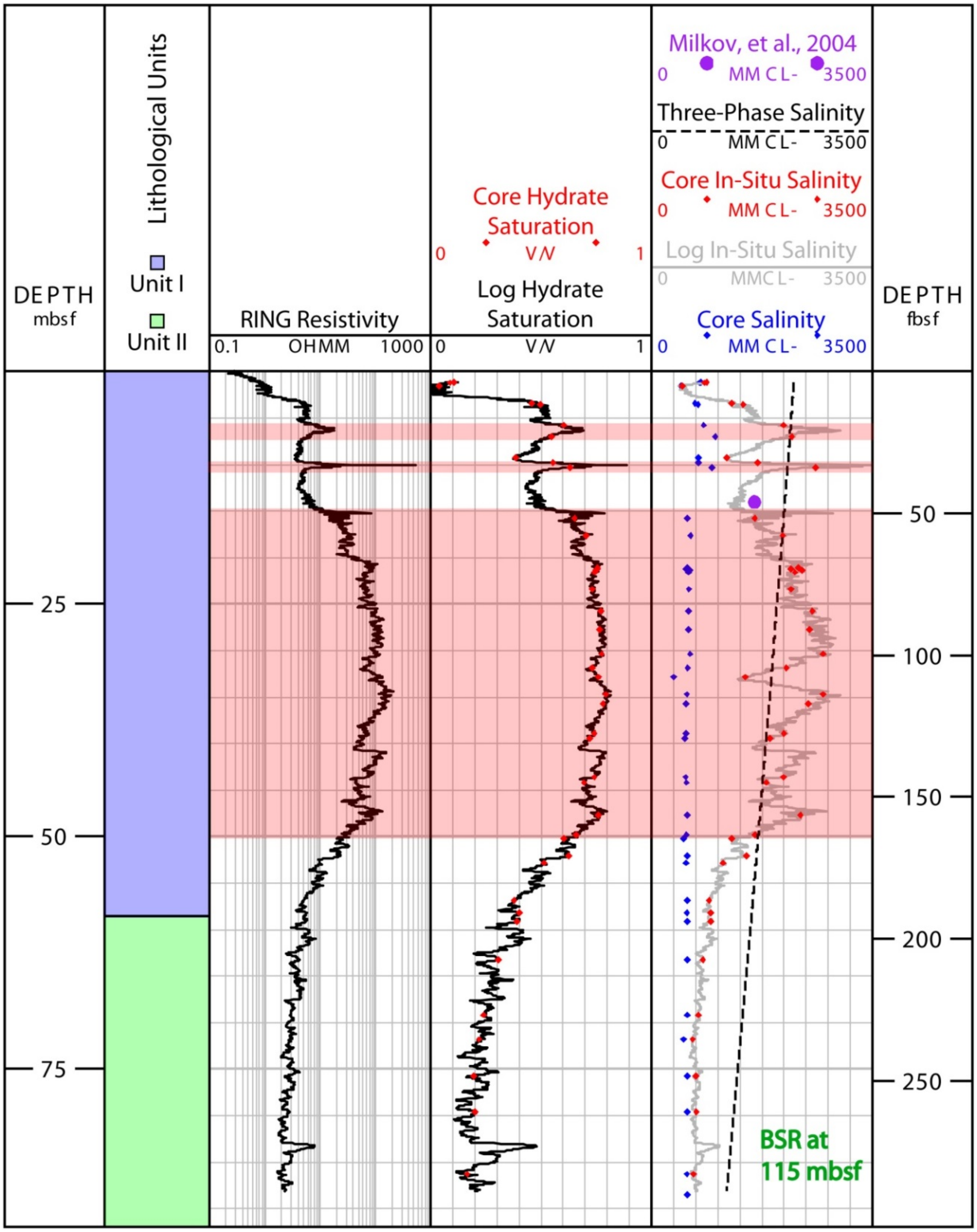

Figure 25: Results from ODP Site 1249A. Track 1: Core-derived lithological units, descriptions can be found in the scientific reports (Shipboard Scientific Party, 2003). Track 2: RING resistivity log; Track 3: Resistivity- (black line) and salinity-interpolated (red dots), Archie-derived hydrate saturation; Track 4: Core-derived salinity (Shipboard Scientific Party, 2003), resistivity- (gray line) and salinity-interpolated (red dots) in-situ salinities, and the salinity required for three-phase equilibrium (dashed line). Red shading shows qualitatively interpreted three-phase equilibrium zones.

3.4.2 IODP Site U1328A

We identify a relatively thin region of the GHSZ (0 – 30 mbsf) with high hydrate saturation, which decreases rapidly to essentially no hydrate for the rest of the GHSZ (Figure 26; Track 1). This zone of high hydrate saturation is correlated with elevated salinities near the top of the GHSZ, but do not reach the three-phase boundary (Figure 26; Track 2). These results suggest that no portion of this system is at three-phase equilibrium.

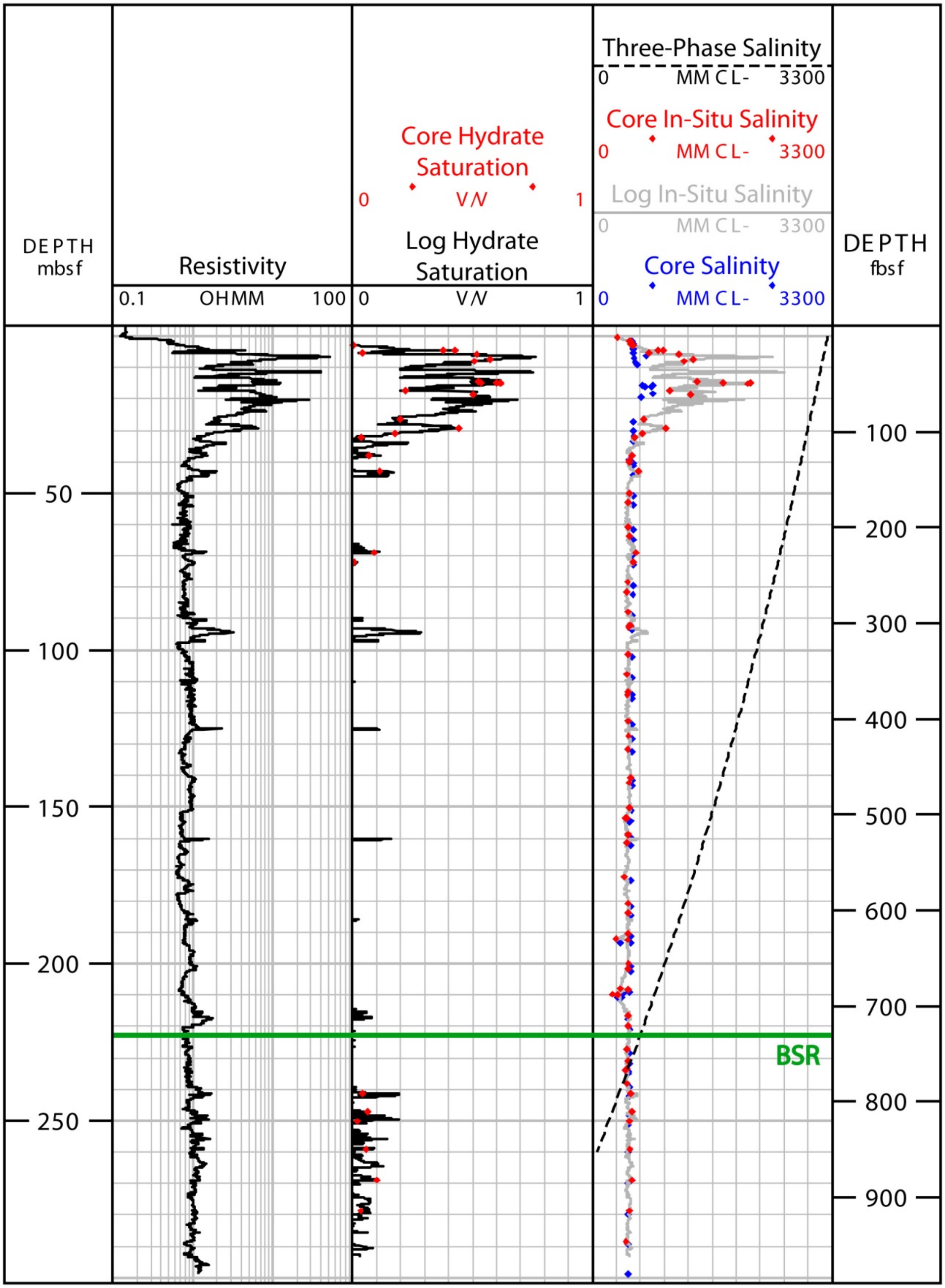

Figure 26: Results from IODP Site U1328A. Track 1 – RING resistivity log; Track 2 – Resistivity (black line) and salinity (red dots) interpolated, Archie-derived hydrate saturations; Track 3 – Core-derived salinity (Expedition 311 Scientists, 2006), resistivity (black line) and salinity (red dots) interpolated in situ salinities, and the salinity required for three-phase equilibrium (dashed line).

3.4.3 NGHP Site 01-10A

At Site 10A, there are four distinct zones of varying hydrate saturation: Zone 1, from 28 – 45 mbsf; Zone 2, from 45 – 90 mbsf; Zone 3, from 90 – 123 mbsf; and Zone 4, from 123 – 160 mbsf. These zones are identified by significant changes in the average value of the hydrate saturations between zones. Zone 1 – 4 have average hydrate saturations of 0.526, 0.7, 0.382, and 0.413, respectively, with a peak saturation of 0.817 at 48.4 mbsf (Figure 27; Track 3). The hydrate saturations in Zones 2 and 4 are consistently high and follow a relatively linear decline in value with depth. The hydrate saturation drops rapidly from 0.40 – 0 in the last 3 meters above the BSR. Zones 1 and 3 exhibit lower hydrate saturations relative to the proximal zones as well as a similar decrease in saturation with depth. Elevated salinities are identified throughout zones 1 – 4, averaging 1181, 1922, 876.6, and 872 mM Cl^-, respectively, ranging between 1.66 – 3.65 times greater than the baseline salinity (Figure 27; Track 4).

We qualitatively interpret Zones 2 and 4, where in-situ salinities are at or exceed the three-phase salinity, to be near to or at three-phase equilibrium. Between 46 – 57 mbsf, the in-situ salinities calculated at the log data resolution (gray line) were far greater than the three-phase salinity. At the pressure and temperature conditions at this depth, hydrate would not be stable under these conditions. We attribute these anomalously high values to the lack of core-derived salinities within this section. The interpolation of salinity values between the available salinity data above and below this region results in an average salinity 94.6 mM Cl^- greater than the baseline. If the baseline salinity were used in this region, the in-situ salinities would decrease by between 270 – 530 mM Cl^-.

Seven pressure cores were recovered while drilling sites 10B and 10D and were used to determine the in-situ hydrate saturation. The resulting saturation values from these analyses are plotted with the calculated hydrate saturations in Figure 11. Two of the cores, 10B-28P (175.1 mbsf) and 10B-25P (164.1 mbsf), were taken below the base of the GHSZ. The volume of gas released from these cores was either below the saturation point of methane in water or would result in a small volume of free gas in the core. The other five pressure cores, 10B-08Y (50.1 mbsf), 10B-15P (98.2 mbsf), 10B-18Y (117.4 mbsf), 10D-12E (77.8 mbsf), and 10D-22E (145.1 mbsf), were taken above the base of the GHSZ. Core 10D-12E, however, had substantial mechanical complications during recovery and storage that resulted in significant hydrate dissociation and gross underestimation of in-situ hydrate saturation (NGHP Expedition 01 Scientists, 2007).

Core 10B-08Y had significant air voiding caused by hydrate dissociation or gas devolution during handling, which significantly reduced the amount of core available to determine hydrate saturation. Also, the micro CT scanner used to quantify hydrate saturation had a resolution two orders of magnitude greater than the pore size, reducing its ability to detect disseminated hydrate (Rees et al., 2011). These handling complications and methodological limitations could have caused significant underestimation of the hydrate saturation.

The other three pressure cores were all associated with varying amounts of hydrate dissociation during recovery that resulted in lower calculated in-situ hydrate saturation (NGHP Expedition 01 Scientists, 2007). Despite these complications, however, the saturations derived from these three pressure cores are correlated relatively well with the Archie-derived hydrate saturations we present here. The average saturation of these pressure cores was 16.3 percent lower than calculated, which can be attributed to the dissociation of hydrate during recovery and handling.

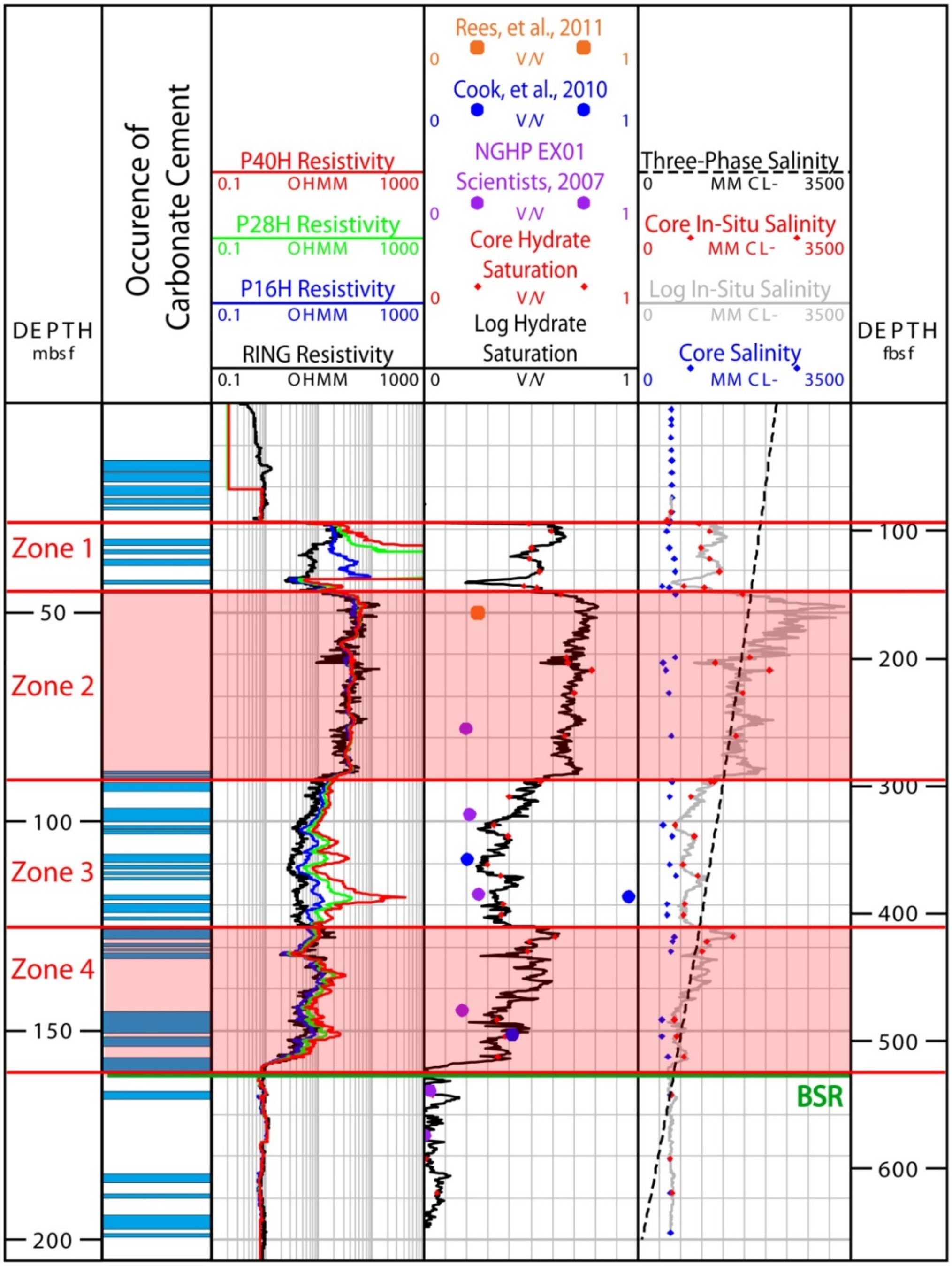

Figure 27: Results from NGHP Site 01-10A. Track 1: Occurrence of carbonate cement derived from recovered cores (NGHP Expedition 01 Scientists, 2007); Track 2: RING (black line) and propagation resistivity curves (colored lines) at 2MHz and depths of investigation ranging from 16 – 40 inches; Track 3: Resistivity- (black line) and salinity-interpolated (red dots), Archie-derived hydrate saturation, pressure core-derived hydrate saturations (NGHP Expedition 01 Scientists, 2007; Rees et al., 2011), and modeled hydrate saturations incorporating resistivity anisotropy (Cook et al., 2010); Track 4: Core-derived salinity (NGHP Expedition 01 Scientists, 2007), resistivity- (gray line) and salinity-interpolated (red dots) in-situ salinities, and the salinity required for three-phase equilibrium (dashed line). Red shading show quantitatively interpreted three-phase equilibrium zones.

3.4.4 Mallik Site 5L-38

Hydrate formation at Mallik 5L-38 is limited to Zones 1 and 3, with decreasing hydrate saturation towards the seafloor (Figure 28; Track 1). Our calculated hydrate saturations correlate well with the saturations determined from the pressure core sampling program (Lu et al., 2005). These zones of high saturation are associated with elevated in situ salinities, however, the salinities only approach or cross the three-phase boundary in Zone 3 (Figure 28; Track 2). From these results, we interpret three-phase equilibrium to exist betnween 1060 – 1107 mbsf.

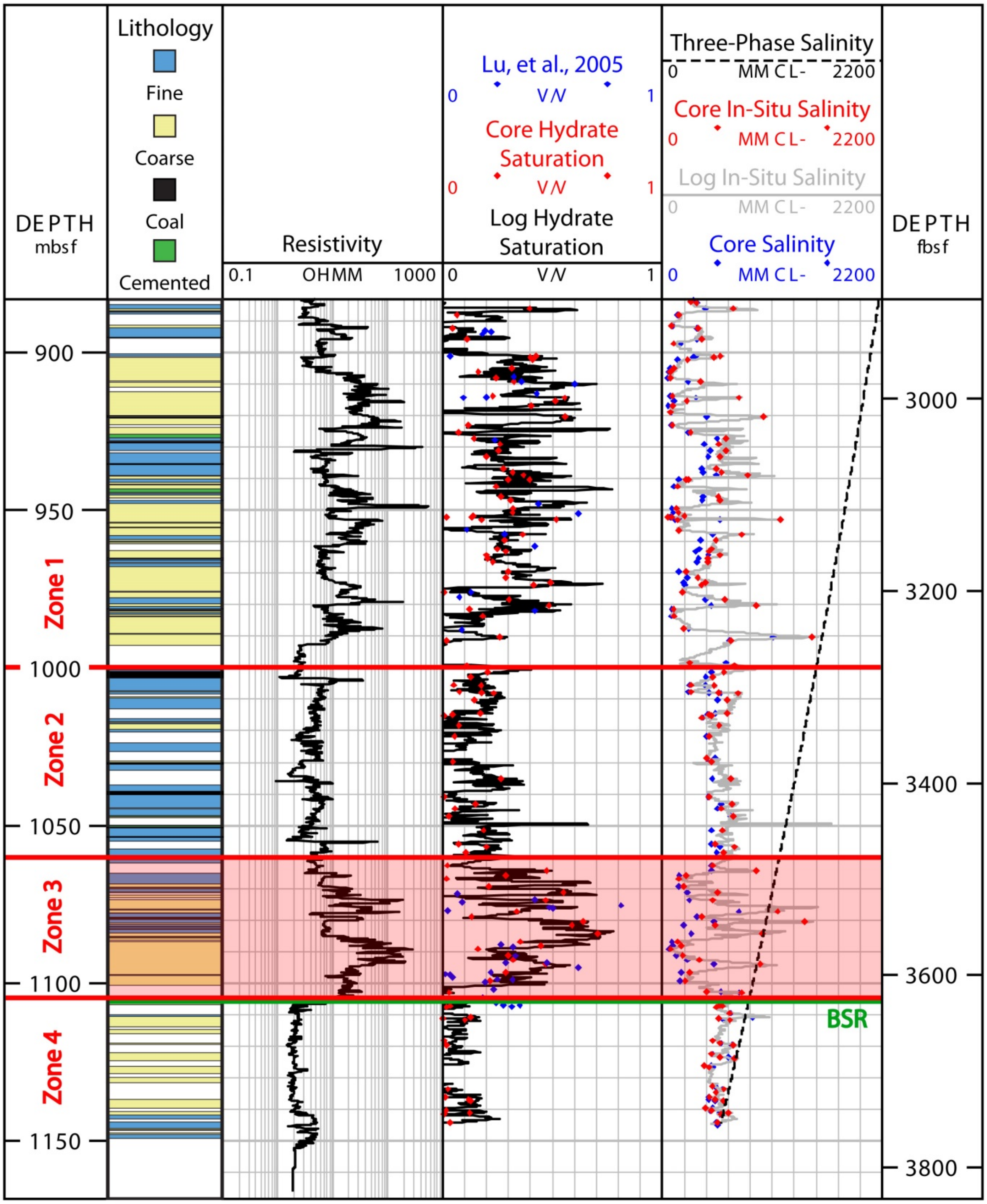

Figure 28: Results from Mallik 5L-38. Track 1 – Core-derived, generalized core lithology; Track 2 – RING resistivity log; Track 3 – Resistivity (black line) and salinity (red dots) interpolated, Archie-derived hydrate saturation and hydrate saturations determined from pressure core samples (Lu et al., 2005). Track 4 – Core-derived salinity (Matsumoto et al., 2005), resistivity (black line) and salinity (red dots) interpolated in situ salinities, and the salinity required for three-phase equilibrium (dashed line). Red boxes indicate zone interpreted as being at three-phase equilibrium.

Study Site	Water Depth (mbsf)	Depth to BSR (mbsf)	Bottom Temperature (ºC)	Geothermal Gradient (°C/km)	Grain Density (g/cm^3)	Fluid Density (g/cm3)	Archie Parameters		
							a	m	N
ODP 1249A	788.5	115	4.0	55	2.70	1.050	1.50	1.89	4
IODP U1328A	1267.7	219	3.5	52	2.76	1.030	1.48	1.40	4
NGHP 01-10A	1049.4	160	6.5	45	2.72	1.023	1.50	1.62	4
Mallik 5L-38	1.0	1107	5.7	30	2.65	1.010	0.75	2.05	4

Table 1: Parameters used to determine in situ hydrate saturation and salinity at each study site. Archie's parameters, a and m, were determined for each site from the LWD data. N was assumed to be constant for all sites. All parameters were taken from the initial and scientific reports for each site (Collett et al., 2005; Expedition 311 Scientists, 2006; Henninges et al., 2005; NGHP Expedition 01 Scientists, 2007; Shipboard Scientific Party, 2003).

3.5 DISCUSSION

3.5.1 Limitations on hydrate formation and distribution

Within the regions interpreted to be at three-phase equilibrium, hydrate formation is buffered by the in-situ salinity. Salinity increases as hydrate forms until it reaches the value required for three-phase stability, which is controlled by the in-situ pressure and temperature conditions. In the zones interpreted to be at two-phase equilibrium, however, hydrate formation could be limited by an absence of gas or by the presence of carbonate cements.

The structure and stability of hydrate is dependent upon the gas composition and flux (Sloan, 1998). Studies have suggested that free gas migrates laterally from ODP Site 1250 to Site 1249, intersecting Site 1249A at approximately 50 mbsf (Liu and Flemings, 2006), resulting in an absence of free gas below this depth. This limits the gas available to form hydrate either to that dissolved in the pore-water or to biogenically produced gas, which explains the lower hydrate saturations observed in this region.

At both study sites, the core was used to identify major lithological units throughout the well according to grain size distribution and the presence of biogenic material. At NGHP Site 01-10A, the core was also used to identify the presence of carbonate cements (Figure 11; Track 1), which frequently complicates the pore structure and decreases permeability (Lucia, 1983). From 0 – 90 mbsf, Zones 1 and 2, core recovery was 64.6 percent and carbonate occurrence was reported in 26.4 percent of the core. Between 90 – 160 mbsf, Zones 3 and 4, core recovery was 67.4 percent with reported carbonate occurrence in 66.1 percent of the core (NGHP Expedition 01 Scientists, 2007). The lower hydrate saturations in Zones 3 could be related to the increased presence of carbonate cements. Either the decreased permeability is reducing the gas saturation and limiting hydrate formation, or it is increasing capillary effects, which decrease hydrate stability (Clennell et al., 1999; Liu and Flemings, 2011) and the three-phase salinity.

3.5.2 Resistivity anisotropy from hydrate-filled fractures

Both of the study sites have been associated with the presence of high-angle, hydrate-filled fractures (Cook et al., 2010; Lee and Collett, 2009; Weinberger and Brown, 2006). It has been suggested that these fractures create an anisotropic medium that could result in overestimates of hydrate saturation, when using isotropic petrophysical methods (Kennedy and Herrick, 2004; Lee and Collett, 2009). In isotropic media, the measured resistivity is the same regardless of the direction in which the measurement is taken. In the presence of alternating layers of materials with distinctly different resistivities, however, the measured resistivity perpendicular ($R_{\perp}$) to the layers tends to be far greater than the resistivity parallel ($R_{\parallel}$) to the layers (Cook et al., 2012; Kennedy and Herrick, 2004). With an isotropic model, this increase in resistivity is attributed to greater hydrate saturation, despite the fact that hydrate-filled fractures contribute little additional hydrate saturation to the sediment. We critically evaluate the distribution and character of the fracture network at each study site to determine if fractures are affecting our results.

Hydrate-filled fractures are identified from recovered core samples and from the Resistivity-At-Bit (RAB) images and the propagation resistivity data collected during LWD acquisition. In the core samples, curators observe concentrated hydrate in fractures and identify the massive presence of hydrate using thermal infrared imaging to detect negative thermal anomalies (NGHP Expedition 01 Scientists, 2007; Shipboard Scientific Party, 2003). The RAB imaging system records the resistivity of the borehole wall in all directions, creating a three-dimensional look at how resistivity changes across the borehole. Hydrate-filled fractures appear as sinusoidal layers with high resistivity, because the fracture intersects the borehole wall at two different depths along the strike orientation. The dip of the fracture (θ) can be calculated from the borehole diameter (D) and amplitude of the fracture (A) on the RAB image (Weinberger and Brown, 2006):

$$\theta = tan^{-1}\left(\frac{A}{D}\right). \qquad \text{Eq. 28}$$

The propagation resistivity tool records the phase-shift and attenuation resistivity at two frequencies and three source-receiver spacings and has been used to infer information about $R_{\parallel}$ and $R_{\perp}$ in the borehole (Ellis and Singer, 2007). Fractures are identified in the phase-shift propagation resistivity data from separation between the resistivity curves, caused by increasing resistivity at greater depths of investigation. Greater separation between the propagation resistivity curves indicates more anisotropic conditions, potentially due to the presence of fractures (Cook et al., 2010). This tool is not only used to identify the presence of fractures, but also provides a qualitative assessment of the degree to which anisotropy is affecting the bulk resistivity measurement.

At ODP Site 1249A, fractures were only identified through the core samples and RAB imaging data; interpretation of these data is limited to the scientific reports. Using the infrared scanner, hydrate was identified in 49 core samples taken from Site 1249F. Only eight of those samples, starting at 47 mbsf, were associated with hydrate in veins or fractures. In the RAB image, the highest concentration of hydrate is between 24 – 50 mbsf, where 20 fractures identified within this region (Shipboard Scientific Party, 2003). This information indicates that the fractures are likely creating anisotropy in the sediment that is causing an increase in resistivity. The resistivity of the sediment, however, is similar to that of the fractures, which diminishes the effects of anisotropy. Therefore, between 24 – 50 mbsf, the bulk resistivity is less affected by the presence of hydrate-filled fractures and using an isotropic model could still be acceptable.

At NGHP Site 01-10A, the infrared scanner identified large amounts of hydrate distributed throughout the well, though none of these occurrences were associated with fractures. The RAB image revealed the presence of hydrate-filled fractures concentrated between 90 – 124 mbsf, with sporadic fractures in other regions of the well (Cook et al., 2010; NGHP Expedition 01 Scientists, 2007). The phase-shift propagation resistivity curves (Figure 11; Track 2) show separation in Zones 1, 3, and 4, with concentrated separation in Zone 3. This indicates the presence of resistive fractures in these regions, supports the results from the RAB image, and suggests that Zone 2 can be considered isotropic.

Cook, et al. (2010) used a one-dimensional forward fracture model to predict the bulk hydrate saturation at three depths, incorporating the effects of resistivity anisotropy. Two of the saturations predicted from this model correlated well with our Archie-calculated saturations (Figure 11; Track 3), suggesting that Archie's law could be valid in anisotropic conditions (Lee and Collett, 2009). These results suggest that the hydrate saturation and salinity we calculated in Zones 2 and 4 accurately represent the in-situ conditions and that, although the conditions at Zones 1 and 3 are affected by anisotropy, the in-situ conditions are well represented using Archie's Law.

3.6 CONCLUSIONS

We present the in-situ hydrate saturation and salinity at four hydrate-bearing sites, calculated using an iterative application of Archie's Law and a salinity correction. We calculate the salinity required for three-phase equilibrium at the in-situ pressure and temperature using a thermodynamic model. We compare the in-situ salinity to the three-phase salinity at each site to determine the thermodynamic state throughout the GHSZ. We conclude that:

- ODP Site 1249A and NGHP Site 01-10A both contain thick regions within the GHSZ where the in-situ pressure, temperature, and salinity conditions suggests that the system is at three-phase equilibrium.
- Mallik Site 5L-38 has a small region near the base of the GHSZ where the in-situ conditions may result in three-phase equilibrium.
- IODP Site U1328A has elevated in-situ salinities near the top of the GHSZ, but the values are not greater enough to reach the three-phase boundary, indicating that this site is not at three-phase equilibrium. This concentration of hydrate near the seafloor is likely a result of the sedimentation and dissolved methane advection rates (Malinverno et al., 2008).
- At ODP Site 1249A, the interpreted three-phase region from 15 – 50 mbsf is associated with hydrate-filled fractures. Between 24-50 mbsf, however, there is little difference between the resistivity of the fractures and matrix, which reduces the effect of anisotropy on the resistivity measurement.

- At NGHP Site 01-10A, the propagation resistivity curve indicates that Zone 2, interpreted to be at three-phase equilibrium, is not associated with resistivity anisotropy, suggesting that the use of Archie's Law here accurately calculates water saturation. We believe that this is due to both a lower occurrence of hydrate-filled fractures, as well as a lower discrepancy between the fracture and matrix resistivities within this region.
- Within Zones 3 and 4, at NGHP Site 01-10A, the presence of carbonate cement could be limiting the formation of hydrate and, therefore, the development of elevated in-situ salinities.
- At NGHP Site 01-10A, although there are fractures present, our saturations correlate well with those from pressure cores and forward fracture models, indicating that the Archie parameters used are attributing for some anisotropic effects.

TASK 4: LABORATORY EVALUATION OF HYDRATE DISSOCIATION

Projected Finish: 3/31/14
Actual Finish: 6/1/14

SUMMARY

We have successfully simulated the formation and dissociation of methane hydrate including the effect of salinity. We successfully demonstrated our ability to experimentally simulate 3-phase equilibrium and we showed how cooling impacted the amount of hydrate that could be formed. Our laboratory results are well-matched by our simulation results. We are now extending this study to form methane hydrates in a meter-long cell and then have this cell undergo warming both from above and from below. These experiments will allow us to complete Task 4.

SUBTASK 4.1 - FREEZING TO 3 PHASE STABILITY CONDITIONS, FOLLOWED BY MELTING FROM ABOVE

Milestone 1.E Demonstrate ability to create and dissociate methane hydrate within sediment columns under conditions analogous to natural systems.

4.1.1 Experimental setup

The experimental chamber consisted of three primary components: sample holder, temperature control, and plumbing and sensing. The sample holder (Figure 29) consists of an aluminum X-ray transparent pressure vessel, two stainless steel end plugs with multiple high-pressure feed-throughs, and an EPDM sleeve attached to two PVC endcaps.

Methane gas (99+%, Praxair) was fed to the sample and pressure was maintained using a Teledyne-Isco (Lincoln, NE) 500D syringe pump running in the constant pressure mode (Figure 29). The volume of gas in the pump was recorded manually. A second Teledyne Isco 500D syringe pump was connected by way of a valve to the downstream end of the sample (Figure 29). This valve was maintained in closed position throughout the test except for one time when a gas connectivity test was performed. Plumbed into the upstream pore fluid line was a 1 L steel sampling bottle containing additional methane gas (Figure 29). This additional methane gas was present for pump refilling if necessary. Pressure was monitored using outputs on the pumps, as well as a Wika S-10 pressure transducer calibrated to an Omega Engineering PCL342 pressure calibrator.

Temperature was measured at a number of locations using thermocouples (Omega Engineering, Stamford, CT). A type J thermocouple was inserted into the sample (T_{in}), and a type T thermocouple was attached to the outside of the sleeve containing the sample (T_{out}), both of which were at the same distance from the downstream end of the sample (Figure 29). A type T thermocouple was used to monitor the tubing temperature, and another was attached to a steel sampling bottle near the syringe pumps to provide an accurate estimate of the gas temperature inside the syringe pumps. Temperature and pressure were recorded every 20 seconds throughout the test using a Keithley 2701 digital multimeter and recorded to a computer. All thermocouples were compared to melting ice, and the temperature indications are corrected using the difference between the indicated temperature and 0 °C.

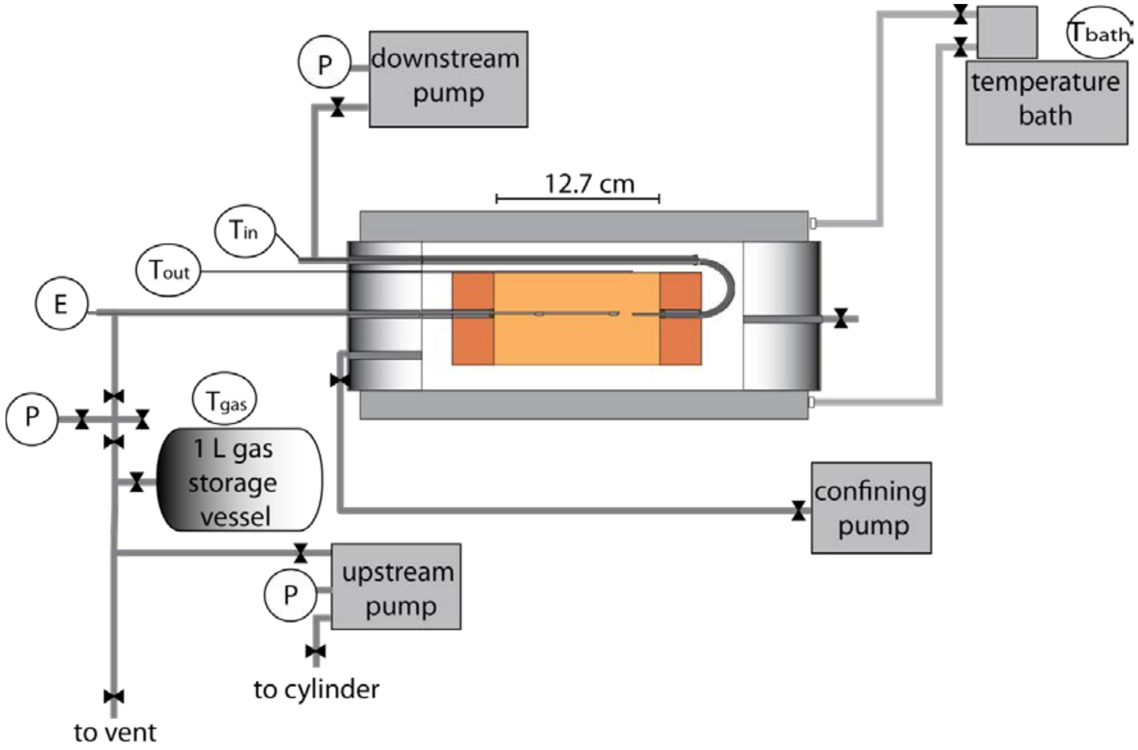

Figure 29: Sketch of experimental setup. P refers to pressure transducer. T_{in}, T_{out} and T_{gas} are thermocouples. T_{out} is placed on the EPDM sleeve, which measures the temperature on the outer radius of the nearly cylindrical sample. T_{in} is placed in the center of the sample. T_{in} and T_{out} are at the same distance from the downstream side of the sample. T_{gas} measures the temperature of the gas in the pumps. E refers to two electrodes measuring the bulk resistivity of the sample.

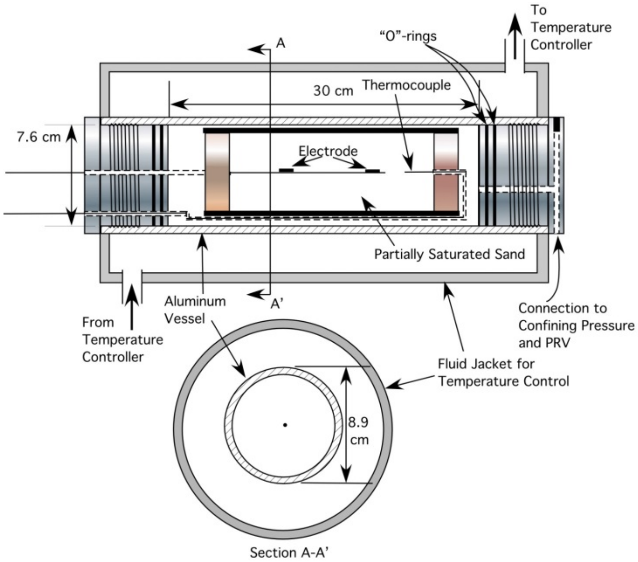
To Temperature Controller
"O"-rings
A
30 cm
Thermocouple
7.6 cm
Electrode
Partially Saturated Sand
Aluminum Vessel
A'
From Temperature Controller
Connection to Confining Pressure and PRV
Fluid Jacket for Temperature Control
8.9 cm
Section A-A'

(a)

(b)

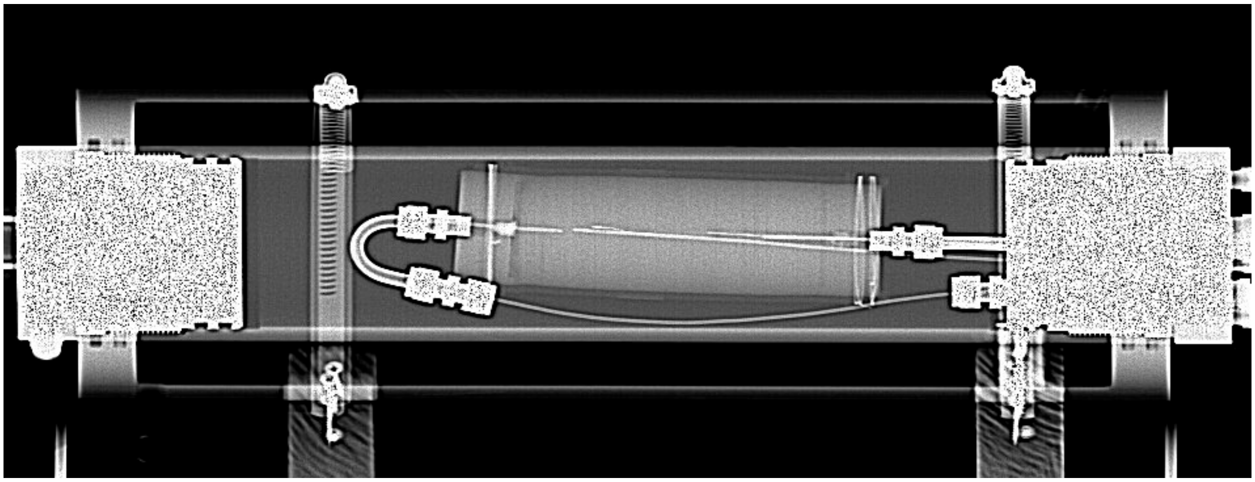

(c)

Figure 30: The detailed sketch (a), photograph (b) and X-ray image (c) of the core. The nearly cylindrical sample has a length of 12.7 cm and diameter of 5.1 cm. The two electrodes are about 3.8 cm from the upstream and downstream ends of the core, respectively. In the X-ray image lighter shade means higher density while darker shade means lower density.

The electrical resistivity probes consisted of two 0.8 mm in diameter (o.d.), 0.8 cm long silver-silver chloride electrodes (In Vivo Metrics, Healdsburg, CA) separated by 5 cm (Figure 30). The silver-silver chloride electrodes were attached to an electrically resistive garolite rod using adhesive-lined heat-shrink tubing (Figure 30). Each electrode was connected to a 0.2 mm enamel-coated copper wire, which was potted in epoxy inside a 1.6 mm diameter stainless steel tube. Prior to packing the sample, we calibrated the electrodes (resistivity array) in a series of potassium chloride solutions (Hodgman, 1960). Impedance between the electrodes was measured using a QuadTech 7400B Precision LCR meter. Both impedance and phase angle were recorded when desired over the frequency range from10 Hz to 100 kHz.

CT scanning was performed using a modified General Electric Lightspeed 16 medical CT scanner. Scans were performed at critical junctures during the experiment, and intermittently for monitoring. Scanning was performed at 120kV and 160 mA, with 0.195 x 0.195 x 0.625 voxel size. Data was analyzed using modified relations from Seol and Kneafsey (2011).

4.1.2 Sample preparation

The sediment used in this experiment was composed of F-110 sand, 99.99% silica sand from U.S. Silica. This silica sand consisted of rounded to subangular grains with a D_{50} of about 110 microns. Prior to the experiment the sand was rinsed with deionized water and allowed to dry under blowing air for 48 hours. We then weighed the sand and placed it in a sealed bag. With the sand grain density of 2.65 g mL^{-1} and target porosity of 36%, we calculated the mass of water needed to achieve a saturation of 55%. Prior to adding the water, we added reagent grade NaCl to the water to achieve a 3.5 wt. % brine solution. We added the brine solution to the sand stepwise, sealed the bag, and kneaded the sand to thoroughly mix the constituents. We allowed the sand to rest overnight to ensure equal distribution of the brine solution.

To pack the sample, a sleeve was attached to the bottom PVC endcap using a double-wrap of wire. A hollow 6 mm o.d. tube was placed over the resistivity probe to protect it. This tube was sequentially raised as the sand was packed. Sand packing was performed by measuring the mass of sand-brine mixture, adding the mixture two teaspoons at a time, and tamping each layer (~ 0.5 cm) approximately 100 times using a 1.2 cm o.d. aluminum rod, rotating the sample frequently to avoid overpacking one side. When the sample was packed to the desired level, the mass of sand and brine in the bag was again weighed, the opposing PVC endcap (the downstream side) containing a Type J thermocouple (T22) was inserted into the sample, and attached using a double wrap of wire. A CT cross section of the sample is shown in Figure 30.

4.1.3 Experimental procedures

At room temperature, we pressurized the confining fluid (a mixture of propylene glycol and water) to 8.27 MPa and the pore pressure to 6.94 MPa and then held the sample under these conditions for

60 hours. This allowed ample time for methane to dissolve into the brine to equilibrium solubility. During this time, we also collected baseline measurements of resistivity and CT images.

During the experiment we cooled the vessel slowly and step-wise to form hydrate and then warmed the vessel similarly to disassociate any hydrate present (red line, Figure 2). Immediately prior to the onset of cooling we closed the valve to the downstream pump. We supplied methane to the sample through the upstream valve so that gas was free to flow into/out the sample at constant pressure in response to the volume changes associated with methane hydrate formation and dissociation in the sample. We successively decreased the temperature in the sample from room temperature (17 ^{o}C) to 12, 10, 8.0, 6.0, 4.0, 2.0 and 0.5 ^{o}C over a period of 15 days (Figure 2). After each temperature change, we waited from one to seven days for the system to reach equilibrium such that neither temperature, pressure, or gas consumption (after leak rate correction) changed.

We equilibrated the sample for four days at the lowest temperature and on Day 19 of the experiment we began to increase the temperature. We successively increased the sample temperature from 0.5 ^{o}C back to 2, 4.0, 6.0, 8.0, 9, 10, 12 ^{o}C and to room temperature (Figure 2). After each temperature change, we found that it only took about 1 day for the system to reach equilibrium (no further change in pressure, temperature, or gas consumption).

In addition to hydrate formation and dissociation, volume change in the upstream pump can be caused by temperature fluctuation, pressure change, and leakage. Analysis of the volume change in the upstream pump allowed us to identify and remediate a leak early in the experiment, however another small leak persisted. The unexpected volume consumptions shown over the first 3 days of the test when the sample was outside the hydrate stability region result largely from laboratory temperature swings which were controlled over the remaining duration of the experiment. There were 16.27 mL less gas in the upstream pump at the end of the experiment (Day 28) than there was at Day 3 although the temperatures and pressure were the same. The average leakage rate was estimated by dividing 16.27 mL by the time elapsed (24.67 days) resulting in a value of 0.66 mL day^{-1}.

We collected several baseline CT images. At the end of the experiment, the sample was saturated with brine by flushing 20 pore volumes of brine with salinity of 3.5 wt.% and CT-scanned. It was then saturated with fresh water by flushing 20 pore volumes of tap water and CT-scanned. It was flushed with three pore volumes of methanol and several days of dry nitrogen gas to dry the sample and CT-scanned at the dry condition.

4.1.4 Experimental results

As the temperature decreased from room temperature to 10, 8, 6 and 4^{o}C (0-7 days, red circles, Figure 2), the measured methane gas consumption slightly increased (0-7 days, black boxes, Figure 2); the gas consumption was 0.2 g, which exactly equaled the gas mass decrease caused by the temperature decline in the sample and room temperature fluctuation (0.2 g) (green line). When the temperature was decreased from 4 to 2 ^{o}C, the accumulated methane gas consumption increased dramatically: 1.7 g of gas was consumed over 7 hours and then 2.1 g of gas was consumed over the next 16 hours. Then over a period of 6 days, more methane was gradually consumed by the system (0.8 g). The final temperature decrease, from 2 to 0.5 ^{o}C resulted in an immediate increase in methane gas consumption to 5.0 g. No further change is observed over 4.5 days.

On Day 19, we began to increase the temperature from 0.5 to 2, 4, 6, 8, 9, 10 and 12^{o}C over a period of 8 days. Methane gas was produced by the dissociating hydrate resulting in gas release (Figure 2). Gas was produced rapidly with each temperature increase. It took about 4 hours for the temperature to increase from one value to the new temperature and the same amount of time for methane gas consumption to decrease. No further gas consumption decrease was detected over one day. Almost 50% of the methane hydrate dissociated when the temperature was increased from 6 to 8 °C on Day 22. The methane consumption (corrected) returned to the original value at the last temperature increase from 8 to 9°C.

The average bulk densities between 10 mm and 105 mm along the sample axis were 1.898, 2.028, 2.020 and1.750 g cm^{-3}from our collected baseline CT images at initial, brine-saturated, fresh water-saturated and dry conditions, respectively. We averaged the data only between 10 and 105mm for the following reasons. First, the packing was different at downstream end (left end) because inserting the end cap inevitably disturbed the sample there (0-10 mm, packing was conducted from upstream end to downstream end); second, sand flowed out of the sample during the brine and water floods at the end of the test, thus some parameters cannot be directly computed over this length at the upstream end (105-127 mm, right end). The grain density, density of brine with 3.5 wt.% salinity and water density are 2.65, 1.030 and 1.002 g cm^{-3} at pressure of 6.94 MPa and temperature of 17 °C, respectively. Gas density is assumed to be 0.0 g cm^{-3} compared with other density values (about 0.053 g cm^{-3} for methane at 6.94 Mpa and 17 °C). Using these data and an initial water saturation of 51%, we compute the estimated porosity to be 35%, 34%, 38% and 38% at initial, dry, brine-saturated and water-saturated conditions, respectively. These estimated porosities were all close to the actual porosity of 35%.

Figure 31(a) shows differential CT images (image at the initial condition subtracted from the image at later times) during methane hydrate formation and dissociation. Information about these images is listed in Table 2. The downstream end of the sample (left side) was closed during the experiment, and the coolant entered the cooling jacket from the downstream side (left side, Figure 31). As the sample was cooled to about 2 °C, the CT images recorded a density increase (red) in the left half of the sample and a density decrease (blue) in the right half (Figure 31). In addition, there was a gradual shift of the area of the density increase, which became more focused on the left side and along the central axis of the sample (images 3-7, Figure 31 (a)). As temperature was increased, the zone of increased density (left) decreased in density, and there was a small increase in density in the low density zone on the right (images 8-10, Figure 31 (a)).

The average density change from the initial condition of each of the 204 slices (0.625 mm in thickness) for a single scan is plotted in Figure 31 (b). As methane hydrate started to form after Day 7.4, the bulk density on the left side increased while that on the right side decreased. The zone with increased density gradually condensed toward the middle of the left half sample with greater density increase from Day 8.7 to Day 15.4, and also towards the sample axis (Figure 31 (b)). From Day 19.4 to Day 25.4, the temperature was stepwise increased and the bulk density change gradually returned to about zero across the sample.

Using the method described in Seol and Kneafsey (2011), we calculated an initial water saturation of 53%. This is close to saturation that was experimentally prepared (51%).We used this approach to calculate the saturations from the CT data (Figure 32). On Day 5.5 and 7.4, the hydrate saturation was zero, and the water and gas saturations were relatively uniform across the sample. As hydrate formed, its saturation increased to more than 50% on the left side whereas it increased to only about 40% on the right side (Day 8.7 to 19.4 in Figure 32 (a)). The water saturation decreased across the sample; however, the decrease was greater in the right half than the left half (Figure 32 (b)). The gas saturation decreased to almost half of the initial value in the left half sample, while it slightly increased in the right side (Figure 32 (c)).

The saturation diagrams illustrate that the bulk density increased in the left half of the sample (Figure 31) because hydrate formed in some fraction of the pore space that was originally gas filled (Figure 32). In contrast, the density on the right side decreased (Figure 31) because as hydrate formed, brine migrated to the left side.As the sample temperature was increased, the phase saturations gradually returned to the initial distributions (Figure 31).

Electrical resistivity data are presented in Figure 33. Bulk resistivity measured with different AC frequencies had the similar trends. When frequencies were greater than 120 Hz, bulk resistivity increased with frequency. Bulk resistivity measured with frequencies no larger than 120 Hz were similar to each other (Figure 33). We divided the experiment to four periods - Period 1 (Day 0 to Day 7.4), 2 (Day 7.4 to Day 14.4), 3 (Day 14.4 to Day 19.4) and 4 (Day 19.4 to Day 27.4), respectively (Figure 33). Bulk resistivity measured with 10 Hz started with a value of 2.8 Ωm and slightly increased with time in Period 1 (red line). As methane gas consumption dramatically increased from Day 7.4 (Period 2), resistivity immediately increased to the first peak value of 35 Ωm on Day 9.4 (red line). Resistivity then gradually declined to about 13.4 Ωm on Day 14.4 (red line), although the gas consumption kept increasing during this time. In Period 3, as temperature was further decreased to 0.5 ^{o}C and more gas was consumed in the sample, resistivity immediately increased to the second peak value of 16.4 Ωm within 3 hours on Day 14 (red line). Resistivity then slowly decreased again at 0.5 ^{o}C. Resistivity gradually decreased as temperature was increased and methane gas consumption decreased stepwise in Period 4. Resistivity quickly increased to a short-lived peak value on Day 22.4 when hydrate was melting. Resistivity did not return to the initial values, but remained slightly higher at the end of the experiment.

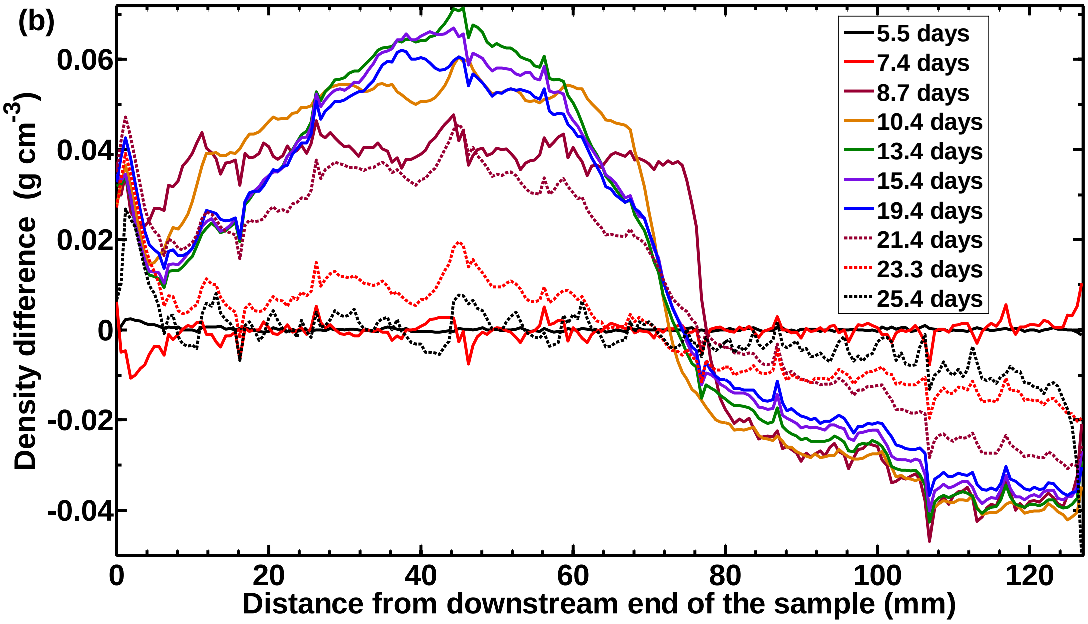

Figure 31: (a) Calibrated difference (image at time = 0 subtracted from image at later times) CT images of the sample at different times. The red color means density increases from the initial condition, while the blue color means density decreases from the initial condition. The unit for the scale is g cm-3. The left hand side of each image is the downstream side of the sample, which is closed during the experiment. The right hand side of each image is the upstream side. Table 2 shows the measurement time, sample temperatures and the accumulated methane gas consumptions for each image. (b) Bulk density change from the initial condition across the sample during methane hydrate formation and dissociation. Bulk density and density change are the average values of all the pixels in one 0.625 mm thick slice from each cross section perpendicular to the longitudinal axis of the sample.

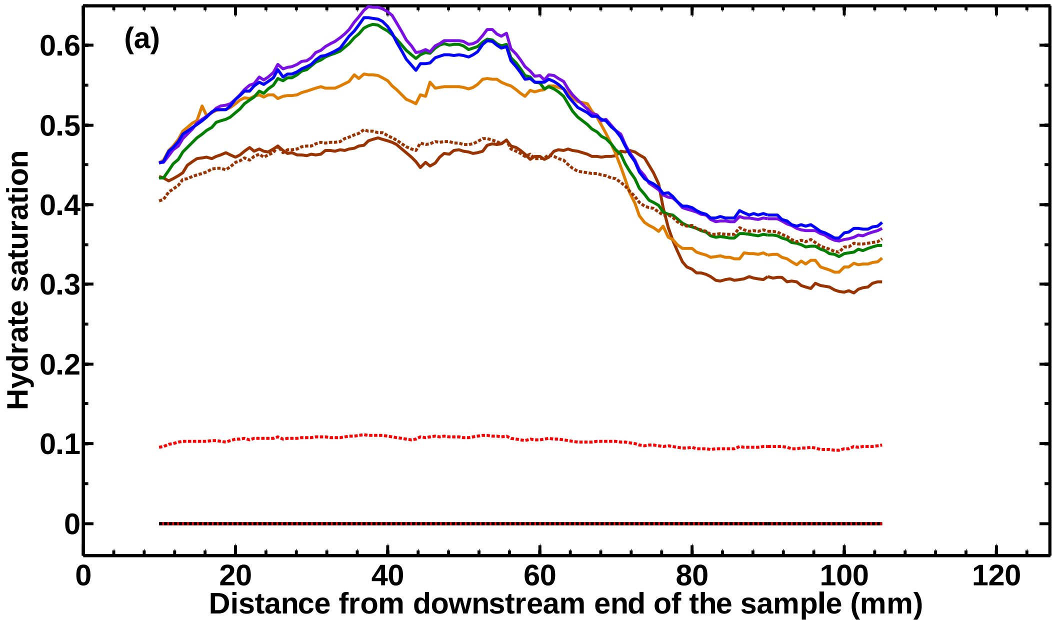

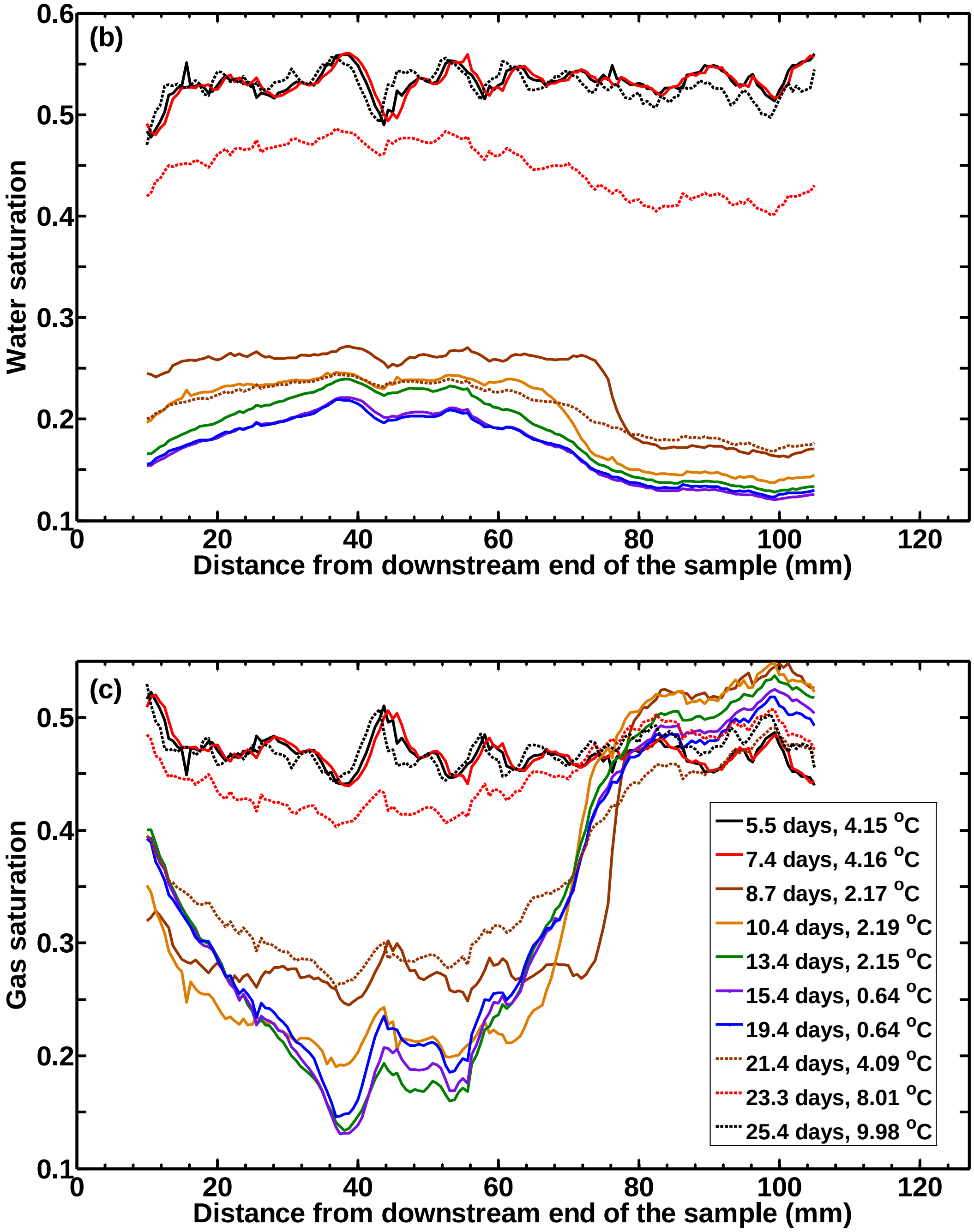

Figure 32: Calculated (a) hydrate, (b) water and (c) gas saturation distributions in the sample at different time using the CT data in Figs. 6 and 7(b). The saturations between 0 and 10 mm, and between 105 and 127 mm are not included here. In Figure 32(a), the solid black, solid red and dashed black lines overlay each other with value of zero.

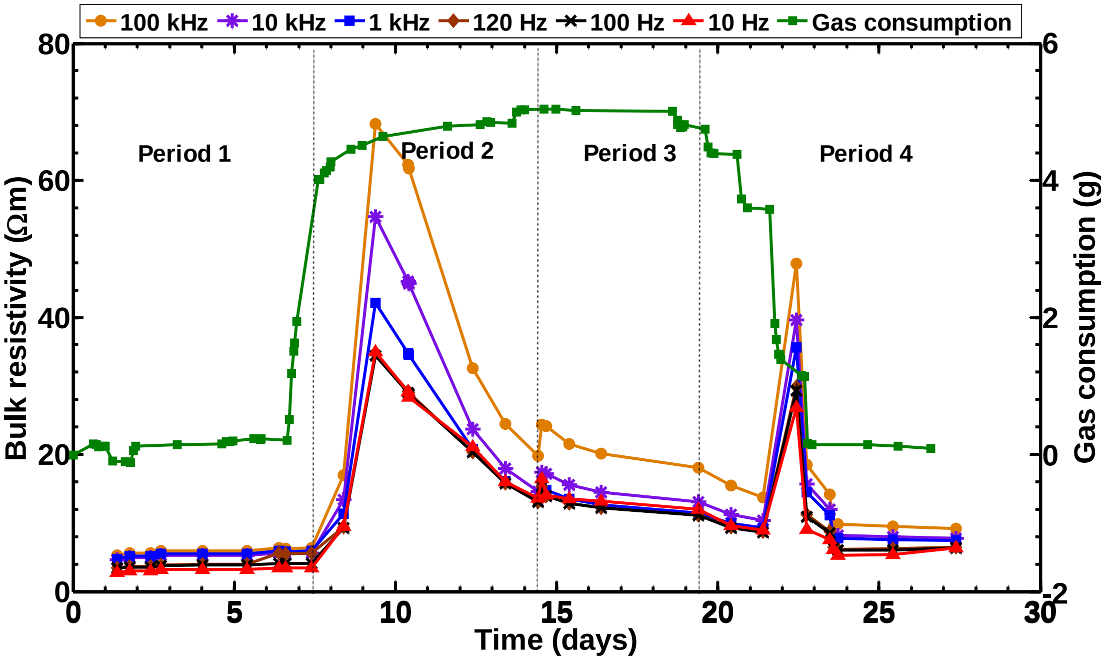

Figure 33: Bulk resistivity (red line) changes during methane hydrate formation and dissociation. The bulk resistivity are measured by two electrodes which are separated by 5.1 cm and are 3.8 cm from the upstream and downstream ends of the sample, respectively.

Number on Montage	Time (days)	Sample temperature T2 (°C)	Accumulated methane gas consumption (g)
1	6.4	4.13	0.2
2	7.4	4.16	0.2
3	8.7	2.17	4.3
4	10.4	2.19	4.6
5	13.4	2.15	4.8
6	15.4	0.64	5.0
7	19.4	0.64	5.0
8	21.4	4.09	4.4
9	23.3	8.01	1.2
10	25.4	9.98	0.1

Table 2: Measurement time, sample temperatures and accumulated methane gas consumptions for CT images in Figure 31(a).

4.1.5 Discussions of experimental results

4.1.5.1 Three-phase equilibrium behavior of hydrate system

The average pressure during this experiment was 6.94 MPa. As discussed before, methane hydrate is predicted to form at 8.4 °C at 6.94 MPa and salinity of 3.5 wt.%. However, as the temperature is decreased to 8, 6 and 4 °C in our experiment, the accumulated methane gas consumption only slightly increased due to room temperature fluctuations and temperature decrease in the sample. Methane hydrate started to form when the temperature was decreased to about 2 °C when the subcooling was 6.4 °C (Figure 2). The same subcooling effect has been observed in many previous experiments, e.g. Rees et al. (2011), Seol and Kneafsey (2009), and Spangenberg et al. (2005). As discussed by (Lederhos et al. (1996)), when the temperature and pressure is within the hydrate forming region, water molecules will organize themselves around each methane molecule to form labile clusters upon the dissolution of methane in water. These labile clusters may either dissipate or combine to form unit cells. The unit cells may either grow or shrink stochastically. Catastrophic methane hydrate growth begins only after a critical radius is reached by the stochastic growth of unit cells. In an isobaric system, subcooling is the driving force for hydrate nucleation (Sloan, 1998). Hydrate nucleation is stochastic at low driving force. However, the system is less stochastic or more predictable at higher driving force (Sloan, 1998). The time from the moment when temperature is decreased to the hydrate stability zone to the initiation of hydrate nucleation is called induction time. The data of Yousif (1994) showed that induction time increased dramatically with the decrease of subcooling (e.g. induction time increased from about 20 minutes at the subcooling of 10 °C to more than 1000 minutes at the subcooling of 5 °C). From the entropy point of view, when methane hydrate forms, the disorderly associated gas and liquid phases transform to orderly hydrate crystals, while when methane hydrate dissociates, the orderly hydrate crystals change to disorderly gas and liquid. Entropy favors disorder over order. Therefore, during hydrate formation, there is a long, metastable period for re-arranging the disorderly gas and liquid into orderly hydrate crystals (Sloan, 1998) (Figure 2). However, methane hydrate melting usually happens rapidly once the system temperature and pressure is out of the hydrates stability zone (Sloan, 1998) (Figure 2). The kinetics of hydrate dissociation have been investigated by Moridis et al. (2005).

As methane hydrate started to form at 2 °C, the gas consumption or hydrate formation was very fast initially (3.8 g methane gas was consumed in 23 hours) and then became slow (0.8 g methane gas was consumed in 6 days, Figure 2). That is because as hydrate forms and salinity increases, the driving force (the difference between the current salinity and the equilibrium salinity at the current pressure and temperature) for further hydrate growth decreases (Sloan, 1998). Additionally, hydrate tends to form at the gas-water interface, thus pockets of water may be partially occluded from the gas. Hydrate ripening will likely change the occlusion over time, allowing more hydrate formation.

The predicted methane gas consumption at three-phase equilibrium is 4% higher than the measurements on Day 13.4 and 15.4 (Figure 2). The calculated hydrate saturations from the measured methane gas consumption (one volume of methane hydrate formation corresponds to about 2.13 volumes of methane gas consumption in this experiment, 47% on Day 13.4, and 49% on Day 15.4) are 2% less than the predicted ones at three-phase equilibrium on Day 13.4 and 15.4 (Figure 34). The most likely reason for the difference between the measured and predicted methane consumptions and hydrate saturations is that as methane hydrate forms, the pores of the sediment is blocked by methane hydrate, and brine with lower-than-equilibrium salinity is isolated from methane gas slowing or preventing further hydrate growth. The differences can also result from the uncertainty of the thermodynamic model used in this study (e.g. the three-phase equilibrium temperatures predicted by Moridis (2008) are slightly lower than that predicted by the model used in this study) and differences between the assumed and unknown actual hydration number (e.g. hydration number is assumed to be 5.75 as used in Liu and Flemings (2007) and Seol and Kneafsey (2011). However, the measurement of Circone et al. (2005) gave an average hydrate stoichiometry of 5.99±0.07 along the three-phase equilibrium boundary). During hydrate dissociation, the difference between the measured and predicted methane gas consumptions decreases with increasing temperature (Figure 2).

The average hydrate saturation calculated from CT data on Day 13.4 and 15.4 are 48% and 50%, respectively (Figure 32(a)), which are very close to 47% and 49% calculated from measured methane gas consumption. The predicted gas saturations are slightly higher than the calculated values at those times, while the predicted water saturations are slightly lower than the calculated values at those times (Figure 4). The predicted bulk average salinity increases as hydrate forms and decreases as hydrate dissociates (Figure 4).

Our experiment was close to three-phase equilibrium at 2 and 0.5 °C during hydrate formation and entire hydrate dissociation. This conclusion is drawn from the following facts: first, the methane hydrate dissociated synchronously with temperature increase in our experiment (Figure 2); second, the predicted methane gas consumption and bulk hydrate saturation based on three-phase equilibrium were close the measurements or direct calculations from the measurements (Figures 2 and 4). Additionally, the presence of hydrate and gas, and forming additional hydrate from cooling beneath 2°C confirms that all three phases were available at 2°C. Previous studies have experimentally observed the effect of salinity in limiting hydrate formation (Husebø et al., 2009; Wright et al., 2005). However, the thermodynamic status of their hydrate systems was unexplored and not clear. To the best of our knowledge, this work is the first to clearly check the status of the hydrate system and demonstrate that the hydrate system is close to three-phase equilibrium constrained by pressure, temperature and salinity.

4.1.5.2 Mass transport during hydrate formation

As methane hydrate formed, the left half sample had higher hydrate saturation than the right half (Figure 32(a)). We attribute this to hydrate first nucleating there. This could have happened because coolant flowed from left to right resulting in a slight thermal gradient and slightly higher subcooling on the left side when temperature was decreased from 4 to 2 °C. This would induce two processes. First, salinity would increase in the left half relative to the right during hydrate growth due to earlier hydrate formation. Salt would tend to diffuse away from the left to the right promoting more hydrate formation in the left half sample at the early stage of hydrate formation. The effective salt diffusivity could be small due to hydrate formation; however, the salinity gradient could be great during earlier stage of hydrate growth. In addition, the system was kept at 2 and 0.5 °C for 7 and 5 days, respectively, to wait for equilibrium (and salt diffusion). Second, the pore size would be smaller in the left half sample than in the right due to the earlier hydrate growth in the left. Therefore, capillary pressure in the left side would be higher than the right side (gas pressure had the constant value of 6.94 MPa across the sample), which would draw in water with lower than equilibrium salinity from right side and provide more water for further hydrate formation in the left half. This core-scale migration of water induced by capillary pressure has also been observed by Kneafsey et al. (2007) and Rees et al. (2011) in fresh water systems. Clennell et al. (1999) theoretically discussed the effect of salt diffusion and brine migration on hydrate formation.

Based on mass conservation of H_2O and NaCl and the calculated hydrate and water saturations (Figure 32), about 6.01 g H_2O and 0.50 g NaCl were estimated to migrate into the region 10-70 mm, and about 1.95 g H_2O was estimated to migrate out and 0.04 g NaCl migrate into the region 70-105 mm on Day 13.4 compared with the initial condition (Figure 32). In this calculation, we used a uniform salinity of 12.7 wt.% across the core (Three-phase equilibrium salinity on Day 13.4 should be 13.4 wt.%, and the calculated methane gas consumption is equal to the measured one if salinity is 12.7 wt.%. Since our experiment was close to three-phase equilibrium and pressure and temperature were the same across the core, the salinity should be relatively uniform across the core). The H_2O and NaCl mass change in the two regions 10-70 mm and 70-105 mm did not balance. That is because we did not calculate the H_2O and NaCl mass changes in regions of 0-10 mm and

105-127 mm (saturations were not calculated there as discussed in Section 3.4). Mass transport should happen and mass balance should be observed among these four regions (0-10 mm, 10-70 mm, 70-105 mm and 105-127 mm) instead of the two regions (10-70 mm and 70-105 mm). H_2O mass decrease and NaCl mass increase in the region of 70-105 mm indicated that during hydrate formation, two mechanisms of salt transport could happen: 1) salt advection with brine from 70-105 mm to 10-70 mm; 2) salt diffusion from 10-70 mm to 70-105 mm.

4.1.5.3 Bulk resistivity changes during hydrate formation and dissociation

The bulk resistivity in hydrate-bearing sediments is a complex function of water saturation, salinity, brine phase connectivity, hydrate morphology and temperature. In hydrate-bearing sediments, electric current transport is mainly conducted by free charge migration in brine (Na^+ and Cl^- here). As methane hydrate formed, the throats of pores are blocked, leading to poor brine connectivity and a fast increase in bulk resistivity (Figure 33). The resistivity gradually declined after the peak values in Period 2 and 3 (Figure 33). This behavior is different from previous studies, where the bulk resistivities of hydrate-bearing sediments reached nearly constant values after hydrate formation (Birkedal et al., 2011; Li et al., 2012; Li et al., 2010; Ren et al., 2010). This declining in bulk resistivity could be caused by the core-scale hydrate and salt redistribution. The methane hydrate saturation increased at the center of the left electrode side but slightly decreased in the surrounding area from image 4 to 5 in Figure 31(a), which were collected during resistivity declining period after the first peak value. This could also be caused by the pore-scale hydrate morphology change. The study by (Katsuki et al., 2007) showed that when methane hydrate formed at the subcooling of greater than 3.4 ^oC (subcooling was 6.4 ^oC in our experiment), the initial hydrate crystals had faceted ends and wavy surfaces. After some time, the wavy surfaces changed to smooth surfaces, and liquid water layers remained between the hydrate crystal and the silica surfaces of the channels. This morphology change led to better brine connectivity and would lead to declining bulk resistivity.

The bulk resistivity decreased with hydrate dissociation in Period 4 (Figure 33) because the brine connectivity became better. However, there was another peak in resistivity on Day 22 (Figure 33). This might be caused by the blockage of pores or poor contact between the electrodes and sediment because of the large amount of gas released from hydrate dissociation, which can be detected a significant decrease in accumulated methane gas consumption during the following day (Figure 33). The hydrate formation and dissociation could redistribute the salinity in the sample resulting in fresher water in the region of the electrodes and thus led to a slightly higher measured bulk resistivity on Day 28 when all the hydrate formed was dissociated (Figure 33).

SUBTASK 4.2 - FREEZING TO L+H CONDITION, WARMING FROM ABOVE

We are currently embarking on a 2nd set of experiments that will be in a 1 meter long core. This experiment will allow us to perform warming from both above and below. Our plans are described under expected outcomes.

SUBTASK 4.3 - FREEZING TO L+H CONDITION, WARMING FROM BELOW

We are currently embarking on a 2nd set of experiments that will be in a 1 meter long core. This experiment will allow us to perform warming from both above and below. Our plans are described under expected outcomes.

NOMENCLATURE TABLE

G	Free gas phase
H	Hydrate phase
L	Liquid phase
u	Pore pressure (MPa)
ρ_{sw}	Seawater Density (g/cm^3)
ρ_{pw}	Pore water density (g/cm^3)
ρ_f	Fluid density (g/cm^3)
ρ_b	Bulk density (g/cm^3)
ρ_m	Grain density (g/cm^3)
Z_{wd}	Water depth (m)
ΔZ	Depth within the GHSZ (m)
Z	GHSZ thickness (m)
g	Gravitational acceleration (m/s^2)
T_f	Formation temperature (ºC)
T_b	Seafloor temperature (ºC)
G_g	Geothermal gradient (ºC/km)
S_h	Hydrate saturation (dimensionless)
S_w	Water saturation (dimensionless)
$C_{in\text{-}situ}$	In-situ salinity (dimensionless)
C_0	Core-derived salinity (dimensionless)
C	Salinity (dimensionless)
N	Saturation exponent (dimensionless)
a	Tortuosity coefficient (dimensionless)
m	Cementation exponent (dimensionless)
n	Porosity (dimensionless)
ρ_w	Fluid resistivity (Ωm)
ρ_t	Formation resistivity (Ωm)
F	Formation factor (dimensionless)

Analytical model

M_m	molar weight of methane (kg mol^{-1})
M_w	molar weight of water (kg mol^{-1})
M_h	molar weight of hydrate (kg mol^{-1})
$m_{g,f}^{m}$	methane mass in the final gas phase (kg)
$m_{h,f}^{m}$	methane mass in the final hydrate phase (kg)

$m^{m}_{w,f}$	methane mass in the final water phase (kg)
$m^{m}_{g,i}$	methane mass in the initial gas phase (kg)
$m^{m}_{w,i}$	methane mass in the initial water phase (kg)
N	stoichiometric hydration number (dimensionless)
P_f	final pressure (Pa)
P_i	initial pressure (Pa)
T_f	final temperature (K)
T_i	initial temperature (K)
$S_{g,i}$	initial gas saturation (dimensionless)
$S_{g,f}$	final gas saturation (dimensionless)
$S_{h,f}$	maximum hydrate saturation (dimensionless)
$S_{w,i}$	initial water saturation (dimensionless)
$S_{w,f}$	final water saturation (dimensionless)
V_{tot}	total volume of the sediment (m^3)
$X^{m}{}_{w,f}$	final solubility of methane in water (wt.%)
$X^{m}{}_{w,i}$	initial solubility of methane in water (wt.%)
$X^{s}{}_{w,i}$	initial mass fraction of salt in brine (wt.%)
$X^{s}{}_{w,f}$	final mass fraction of salt in brine (wt.%)
$\rho_{w,f}$	initial brine density (kg m^{-3})
$\rho_{w,i}$	final brine density (kg m^{-3})
$\rho_{g,i}$	initial gas density (kg m^{-3})
$\rho_{g,f}$	final gas density (kg m^{-3})
ρ_h	methane hydrate density (kg m^{-3})
ϕ	porosity of the sediment (dimensionless)
Δm	mass of methane gas consumed during hydrate formation (kg)

Numerical model

β	phase
e	energy component
g	gas phase
h	hydrate phase
κ	component
l	liquid phase
m	methane component
s	salt component
v	vapor phase
w	water component
C_R	heat capacity of the solid grain (J kg^{-1} oC^{-1})
D^{κ}_{l0}	molecular diffusion coefficient of component k in free water (m^2 s^{-1})
ϕ	porosity of the sediment (dimensionless)

ϕ_0	porosity in the absence of hydrate (dimensionless)
g	acceleration due to gravity (m s^{-2})
h_{β}	specific enthalpy of phase β (J kg^{-1})
k	intrinsic permeability (m^2)
k_0	permeability in the absence of hydrate (m^2)
$k_{r\beta}$	relative permeability of phase β (dimensionless)
λ	overall thermal conductivity of porous media (W m^{-1} $^{o}C^{-1}$)
λ_{β}	thermal conductivity of phase β (W m^{-1} $^{o}C^{-1}$)
λ_R	thermal conductivity of grain (W m^{-1} $^{o}C^{-1}$)
μ_{β}	viscosity of phase β (Pa s)
P_c	capillary pressure (Pa)
P_{c0}	capillary pressure in the absence of hydrate (Pa)
P_{β}	β phase pressure (Pa)
q^e	generation rate of energy (J m^{-3} s^{-1})
q^{κ}	generation rate of component κ (kg m^{-3} s^{-1})
ρ_{β}	density of phase β (kg m^{-3})
S_{β}	saturation of phase β (dimensionless)
T	temperature (^{o}C)
t	time (s)
u_{β}	specific internal energy of phase β (J kg^{-1})
X_{β}^{k}	mass fraction of component κ in phase β (dimensionless)

REFERENCES

Archer, D., Martin, P., Buffett, B., Brovkin, V., Rahmstorf, S., and Ganopolski, A., 2004, The importance of ocean temperature to global biogeochemistry: Earth and Planetary Science Letters, v. 222, p. 333-348.

Archie, G.E., 1941, The electrical resistivity log as an aid in determining some reservoir characteristics: Transactions of AIME, v. 146, p. 9.

Arps, J.J., 1953, The Effect of Temperature on the Density and Electrical Resistivity of Sodium Chloride Solutions: Society of Petroleum Engineers, v. 5, p. 4.

Bear, J., 1972, Dynamics of Fluids in Porous Media: Mineola, N. Y., Dover.

Bily, C., and Dick, J.W.L., 1974, Naturally occurring gas hydrates in the Mackenzie Delta, N.W.T: Bulletin of Canadian Petroleum Geology, v. 22, p. 340-352.

Birkedal, K.A., Ersland, G., Hauge, L.P.O., and Graue, A., 2011, Electrical resistivity measurement of CH4 hydrate-bearing sandstone during formation, the 7th International Conference on Gas Hydrates: Edinburgh, Scotland, United Kingdom.

Circone, S., Kirby, S.H., and Stern, L.A., 2005, Direct Measurement of Methane Hydrate Composition along the Hydrate Equilibrium Boundary: The Journal of Physical Chemistry B, v. 109, p. 9468-9475.

Clennell, M.B., Hovland, M., Booth, J.S., Henry, P., and Winters, W.J., 1999, Formation of natural gas hydrates in marine sediments 1. Conceptual model of gas hydrate growth conditioned by host sediment properties: Journal of Geophysical Research, v. 104, p. 22985-23003.

Collett, T.S., and Dallimore, S.R., 1998, Quantitative assessment of gas hydrates in the Mallik L-38 well, Mackenzie Delta, NWT, Canada, *in* Lewkowicz, A.G.a.A., M., ed., Proceedings of the Eighth International Conference on Permafrost, June 23-27, 1998, Volume Bulletin 585: Quebec, Quebec, Centre d'etudes nordiques, p. 6.

Collett, T.S., and Ladd, J., 2000, Detection of gas hydrate with downhole logs and assessment of gas hydrate concentrations (saturations) and gas volumes on the Blake Ridge with electrical resistivity log data, Proceedings of the Ocean Drilling Program, Scientific Results, Volume 164: College Station, TX, Texas A & M University, Ocean Drilling Program, p. 179 -191.

Collett, T.S., Lee, M.W., Zyrianova, M.V., Mrozewski, S.A., Guerin, G., Cook, A.E., and Goldberg, D.S., 2012, Gulf of Mexico Gas Hydrate Joint Industry Project Leg II logging-while-drilling data acquisition and analysis: Marine and Petroleum Geology, v. 34, p. 41-61.

Collett, T.S., Lewis, R.E., and Dallimore, S.R., 2005, JAPEX/JNOC/GSC et al. Mallik 5L-38 gas hydrate production research well downhole well-log and core montages, *in* Dallimore, S.R., and Collett, T. S., ed., Scientific Results from the Mallik 2002 Gas Hydrate Production Research Well Program, Mackenzie Delta, Northwest Territories, Canada, Volume Bulletin 585, Geological Survey of Canada, p. 23.

Cook, A.E., Anderson, B.I., Malinverno, A., Mrozewski, S., and Goldberg, D.S., 2010, Electrical anisotropy due to gas hydrate-filled fractures: Geophysics, v. 75, p. F173-F185.

Cook, A.E., Anderson, B.I., Rasmus, J., Sun, K., Li, Q., Collett, T.S., and Goldberg, D.S., 2012, Electrical anisotropy of gas hydrate-bearing sand reservoirs in the Gulf of Mexico: Marine and Petroleum Geology, v. 34, p. 72-84.

Crain, E.R., 2013, Crain's Petrophysical Handbook - Resistivity Basic.

Dallimore, S.R., Uchida, T., and Collett, T., 1999, Summary, *in* Dallimore, S.R., Uchida, T., and Collett, T.S., eds., Scientific results from JAPEX/JNOC/GSC Mallik 2L-38 Gas Hydrate Production Research Well, Mackenzie Delta, Northwest Territories, Canada, Volume Bulletin 544, Geological Survey of Canada, p. 10.

Dickens, G.R., 2003, Rethinking the global carbon cycle with a large, dynamic and microbially mediated gas hydrate capacitor: Earth and Planetary Science Letters, v. 213, p. 169-183.

Duan, Z., Møller, N., Greenberg, J., and Weare, J.H., 1992, The prediction of methane solubility in natural waters to high ionic strength from 0 to 250°C and from 0 to 1600 bar: Geochimica et Cosmochimica Acta, v. 56, p. 1451-1460.

Ellis, D.V., and Singer, J.M., 2007, Well Logging for Earth Scientists, 2nd ed., Springer, 692 p.

Expedition 311 Scientists, 2006, Site U1328, *in* Riedel, M., Collett, T.S., Malone, M.J., and Expedition 311 Scientists, eds., Proceedings of the Integrated Ocean Drilling Program, Volume 311: Washington, DC (Integrated Ocean Drilling Program Management International, Inc.).

Haeckel, M., Suess, E., Wallmann, K., and Rickert, D., 2004, Rising methane gas bubbles form massive hydrate layers at the seafloor: Geochimica et Cosmochimica Acta, v. 68, p. 4335-4345.

Heeschen, K.U., Trehu, A.M., Collier, R.W., Suess, E., and Rehder, G., 2003, Distribution and height of methane bubble plumes on the Cascadia Margin characterized by acoustic imaging: Geophysical Research Letters, v. 30.

Henninges, J., Schrotter, J., Erbas, K., and Huenges, E., 2005, Temperature field of the Mallik gas hydrate occurrence - implication on phase changes and thermal properties, *in* Dallimore, S.R., and Collett, T.S., eds., Scientific Results from the Mallik 2002 Gas Hydrate Production Research Well Program, Mackenzie Delta, Northwest Territories, Canada, Volume Bulletin 585, Geological Survey of Canada, p. 11.

Henry, P., Thomas, M., and Ben Clennell, M., 1999, Formation of natural gas hydrates in marine sediments 2. Thermodynamic calculations of stability conditions in porous sediments: Journal of Geophysical Research, v. 104, p. 23005-23022.

Hesse, R., and Harrison, W.E., 1981, Gas hydrates (clathrates) causing pore-water freshening and oxygen isotope fractionation in deep-water sedimentary sections of terrigenous continental margins: Earth and Planetary Science Letters, v. 55, p. 10.

Hodgman, C.D., 1960, Handbook of Chemistry and Physics: Cleveland, Ohio, Chemical Rubber Publishing Co.

Husebø, J., Ersland, G., Graue, A., and Kvamme, B., 2009, Effects of salinity on hydrate stability and implications for storage of CO2 in natural gas hydrate reservoirs: Energy Procedia, v. 1, p. 3731-3738.

IOC, IHO, and BODC, 2003, Centenary Edition of the GEBCO Digital Atlas, published on CD-ROM on behalf of the Intergovernmental Oceanographic Commission and the International Hydrographic Organization as part of the General Bathymetric Chart of the Oceans: Liverpool, U.K., British Oceanographic Data Centre.

Katsuki, D., Ohmura, R., Ebinuma, T., and Narita, H., 2007, Methane hydrate crystal growth in a porous medium filled with methane-saturated liquid water: Philosophical Magazine, v. 87, p. 1057-1069.

Kayen, R.E., and Lee, H.J., 1991, Pleistocene slope instability of gas hydrate-laden sediment on the Beaufort margin: Marine Geotechnology, v. 10.

Kennedy, W.D., and Herrick, D.C., 2004, Conductivity Anisotropy In Shale-Free Sandstone, Society of Petrophysicists and Well-Log Analysts.

Kleinberg, R.L., Flaum, C., Griffin, D.D., Brewer, P.G., Malby, G.E., Peltzer, E.T., and Yesinowski, J.P., 2003, Deep sea NMR: Methane hydrate growth habit in porous media and its relationship to hydraulic permeability, deposit accumulation, and submarine slope stability: Journal of Geophysical Research: Solid Earth, v. 108, p. 2508.

Kneafsey, T.J., Tomutsa, L., Moridis, G.J., Seol, Y., Freifeld, B.M., Taylor, C.E., and Gupta, A., 2007, Methane hydrate formation and dissociation in a partially saturated core-scale sand sample: Journal of Petroleum Science and Engineering, v. 56, p. 108-126.

Kvenvolden, K.A., 1988, Methane Hydrate: A Major Reservoir of Carbon in the Shallow Geosphere?: Chemical Geology, v. 71, p. 11.

Kvenvolden, K.A., 1993, Gas hydrates-geological perspective and global change: Reviews of Geophysics, v. 31, p. 173-187.

Lederhos, J.P., Long, J.P., Sum, A., Christiansen, R.L., and Sloan Jr, E.D., 1996, Effective kinetic inhibitors for natural gas hydrates: Chemical Engineering Science, v. 51, p. 1221-1229.

Lee, M.W., and Collett, T.S., 2009, Gas hydrate saturations estimated from fractured reservoir at Site NGHP-01-10, Krishna-Godavari Basin, India: Journal of Geophysical Research: Solid Earth, v. 114, p. B07102.

Li, F., Sun, C., Li, S., Chen, G., Guo, X., Yang, L., Pan, H., Li, S., and Zhang, K., 2012, Experimental studies on the evolvement of electrical resistivity during methane hydrate formation in sediments: Energy & Fuels, v. 26, p. 6210-6217.

Li , S., Xia, X., Xuan, J., Liu, Y., and Li, Q., 2010, Resistivity in formation and decomposition of natural gas hydrate in porous medium: Chinese Journal of Chemical Engineering, v. 18, p. 39-42.

Liu, X., and Flemings, P.B., 2006, Passing gas through the hydrate stability zone at southern Hydrate Ridge, offshore Oregon: Earth and Planetary Science Letters, v. 241, p. 211-226.

—, 2007, Dynamic multiphase flow model of hydrate formation in marine sediments: Journal of Geophysical Research, v. 112.

—, 2011, Capillary effects on hydrate stability in marine sediments: Journal of Geophysical Research-Solid Earth, v. 116, p. 24.

Lu, H., Dutrisac, R., Ripmeester, J., Wright, F., and Uchida, T., 2005, Measurements of gas hydrate saturation in sediment cores recovered from the JAPEX/JNOC/GSC et al. Mallik 5L-38 gas hydrate production research well, *in* Dallimore, S.R., and Collett, T. S., ed., Scientific Results from the Mallik 2002 Gas Hydrate Production Research Well Program, Mackenzie Delta, Northwest Territories, Canada, Volume Bulletin 585, Geological Survey of Canada, p. 11.

Lucia, F.J., 1983, Petrophysical Parameters Estimated From Visual Descriptions of Carbonate Rocks: A Field Classification of Carbonate Pore Space.

Malinverno, A., Kastner, M., Torres, M.E., and Wortmann, U.G., 2008, Gas hydrate occurrence from pore water chlorinity and downhole logs in a transect across the northern Cascadia margin (Integrated Ocean Drilling Program Expedition 311): Journal of Geophysical Research: Solid Earth, v. 113, p. B08103.

Matsumoto, R., Tomaru, H., Chen, Y.F., Lu, H., and Clark, I.D., 2005, Geochemistry of the interstital waters of the JPAX/JNOC/GSC et al. Mallik 5L-38 gas hydrate production research well, *in* Dallimore, S.R., and Collett, T. S., ed., Scientific Results from the Mallik 2002 Gas Hydrate Production Research Well Program, Mackenzie Delta, Northwest Territories, Canada, Volume Bulletin 585, Geological Survey of Canada, p. 11.

Medioli, B.E., Wilson, N., Dallimore, S.R., Pare, D., Brennan-Alpert, P., and Oda, H., 2005, Sedimentology of the cored interval, JAPEX/JNOC/GSC et al. gas hydrate production research well, *in* Dallimore, S.R., and Collett, T. S., ed., Scientific Results from the Mallik 2002 Gas Hydrate Production Research Well Program, Mackenzie Delta, Northwest Territories, Canada, Volume Bulletin 585, Geological Survey of Canada, p. 14.

Mienert, J., Vanneste, M., Bünz, S., Andreassen, K., Haflidason, H., and Sejrup, H.P., 2005, Ocean warming and gas hydrate stability on the mid-Norwegian margin at the Storegga Slide: Marine and Petroleum Geology, v. 22, p. 233-244.

Milkov, A.V., 2004, Global estimates of hydrate-bound gas in marine sediments: how much is really out there?: Earth-Science Reviews, v. 66, p. 183-197.

Milkov, A.V., Dickens, G.R., Claypool, G.E., Lee, Y.-J., Borowski, W.S., Torres, M.E., Xu, W., Tomaru, H., Tréhu, A.M., and Schultheiss, P., 2004, Co-existence of gas hydrate, free gas, and brine within the regional gas hydrate stability zone at Hydrate Ridge (Oregon margin): evidence from prolonged degassing of a pressurized core: Earth and Planetary Science Letters, v. 222, p. 829-843.

Moridis, G., 2008, TOUGH+Hydrate v1.0 User's Manual: A Code for the Simulation of System Behavior in Hydrate-Bearing Geologic Media.

Moridis, G.J., Seol, Y., and Kneafsey, T.J., 2005, Studies of Reaction Kinetics of Methane Hydrate Dissocation in Porous Media.

NGHP Expedition 01 Scientists, 2007, Sites NGHP-01-10, 12, and 13, *in* Collett, T.S., Reidel, M., Cochran, J., Boswell, R., Presley, J., Kumar, P., Sathe, A., Sethi, A., Lall, M., and the NGHP Expedition 01 Scientists, eds., National Gas Hydrate Program Expedition 01 Initial Reports, Directorate General of Hydrocarbon, Ministry of Petroleum and Natural Gas (India), p. 150.

Nixon, M.F., and Grozic, J.L.H., 2007, Submarine slope failure due to gas hydrate dissociation: a preliminary quantification: Canadian Geotechnical Journal, v. 44, p. 10.

Paull, C.K., Buelow, W.J., Ussler, W.I., and Borowski, W.S., 1996, Increased continental-margin slumping frequency during sea-level lowstands above gas hydrate bearing sediments: Geology, v. 24, p. 4.

Pearson, C.F., Halleck, P.M., McGuire, P.L., Hermes, R., and Mathews, M., 1983, Natural gas hydrate deposits: a review of in situ properties: The Journal of Physical Chemistry, v. 87, p. 4180-4185.

Reagan, M.T., and Moridis, G.J., 2008, Dynamic response of oceanic hydrate deposits to ocean temperature change: Journal of Geophysical Research: Oceans, v. 113, p. C12023.

Rees, E.V.L., Kneafsey, T.J., and Seol, Y., 2011, Methane hydrate distribution from prolonged and repeated formation in natural and compacted sand samples: X-Ray CT observations: Journal of Geological Research, v. 2011.

Ren, S., Liu, Y., Liu, Y., and Zhang, W., 2010, Acoustic velocity and electrical resistance of hydrate bearing sediments: Journal of Petroleum Science and Engineering, v. 70, p. 52-56.

Schmuck, E.A., and Paull, C.K., 1993, Evidence for gas accumulation associated with diaprisim and gas hydrates at the head of the Cape Fear Slide: Geo-Marine Letters, v. 13, p. 8.

Seol, Y., and Kneafsey, T.J., 2009, X-ray computed-tomography observations of water flow through anisotropic methane hydrate-bearing sand: Journal of Petroleum Science and Engineering, v. 66, p. 121-132.

—, 2011, Methane hydrate induced permeability modification for multiphase flow in unsaturated porous media: Journal of Geophysical Research: Solid Earth, v. 116, p. B08102.

Serra, O., 1984, Fundamentals of Well-log Interpretation: The interpretation of logging data, Elsevier.

Shipboard Scientific Party, 2003, Site 1249, *in* Trehu, A.M., Bohrmann, G., Rack, F.R., Torres, M.E., and et al., eds., Proceedings of the Ocean Drilling Program, Initial Reports, Volume 204: College Station, Ocean Drilling Program.

Shipley, T.H., Houston, M.H., Buffler, R.T., Shaub, F.J., McMillen, K.J., Ladd, J.W., and Worzel, J.L., 1979, Seismic evidence for widespread possible gas hydrate horizons on continental slopes and rises: AAPG Bulletin, v. 63, p. 2204-2213.

Sloan, E.D., 1998, Clathrate Hydrates of Natural Gases: Marcel Dekker, New York, 705 p.

Spangenberg, E., 2001, Modeling of the influence of gas hydrate content on the electrical properties of porous sediments: Journal of Geophysical Research: Solid Earth, v. 106, p. 6535-6548.

Spangenberg, E., Kulenkampff, J., Naumann, R., and Erzinger, J., 2005, Pore space hydrate formation in a glass bead sample from methane dissolved in water: Geophysical Research Letters, v. 32, p. L24301.

Takahashi, H., Fercho, E., and Dallimore, S.R., 2005, Drilling and operations overview of the Mallik 2002 Production Research Well Program, *in* Dallimore, S.R., and Collett, T. S., ed., Scientific Results from the Mallik 2002 Gas Hydrate Production Research Well Program, Mackenzie Delta, Northwest Territories, Canada, Volume Bulletin 585, Geological Survey of Canada, p. 14.

Torres, M.E., Kim, J.H., Choi, J.Y., Ryu, B.J., Bahk, J.J., Riedel, M., Collett, T.S., Hong, W.L., and Kastner, M., 2011, Occurrence of high salinity fluids associated with massive near-seafloor gas hydrate deposits, Proceedings of the 7th International Conference on Gas Hydrates: Edinburgh, Scotland, United Kingdom, p. 19.

Trehu, A.M., Flemings, P.B., Bangs, N.L., Chevallier, J., Johnson, J.E., Liu, C.S., Liu, X., Reidel, M., and Torres, M.E., 2004, Feeding methane vents and gas hydrate deposits at south Hydrate Ridge: Geophysical Research Letters, v. 31, p. 4.

Weinberger, J.L., and Brown, K.M., 2006, Fracture networks and hydrate distribution at Hydrate Ridge, Oregon: Earth and Planetary Science Letters, v. 245, p. 123-136.

Wright, J.F., Dallimore, S.R., Nixon, F.M., and Duchesne, C., 2005, In situ stability of gas hydrate in reservoir sediments of the JAPEX/JNOC/GSC et al. Mallik 5L-38 gas hydrate production well, *in* Dallimore, S.R., and Collett, T. S., ed., Scientific Results from the Mallik 2002 Gas Hydrate Production Research Well Program, Mackenzie Delta, Northwest Territories, Canada, Volume Bulletin 585, Geological Survey of Canada, p. 11.

Yousif, M.H., 1994, The kinetics of hydrate formation, 69th Annual Technical Conference Soc. of Petrol. Eng.: New Orleans, LA.